2019 年度

青山学院大学審査学位論文

指導教員　　山崎 了　教授

Magnetic Field Amplification in Relativistic Collisionless Shocks Formed in Gamma-Ray Bursts

ガンマ線バーストにおける相対論的無衝突衝撃波での磁場増幅機構

理工学研究科

理工学専攻

冨田　沙羅

Magnetic Field Amplification in Relativistic Collisionless Shocks Formed in Gamma-Ray Bursts

Sara Tomita

Department of Physics and Mathematics
Aoyama Gakuin University
December, 2019

Acknowledgement

I would like to extend my gratitude to:

Professor Ryo Yamazaki for being my supervisor and a great source of inspiration and useful discussions.

Assistant Professor Yutaka Ohira for collaboration, helpful comments about plasma physics and particle acceleration, and a great source of inspiration.

Professor Youichi Sakawa for collaboration and teaching me about laser astrophysics and its experimental technique during my stay in Osaka University.

Professor Masahiro Hoshino, and Associate Professor Takanobu Amano for helpful comments about plasma physics and helping me in every way during my stay in the University of Tokyo.

Assistant Professor Yosuke Matsumoto for teaching me about particle-in-cell simulation.

The students and staff at Yamazaki laboratory in Aoyama Gakuin University and the University of Tokyo and Osaka univerisity for coffee and fruitful discussions.

Grant-in-Aid for JSPS Research Fellowships for Young Scientists, Aoyama Gakuin University for financial support of my PhD studies.

My family for supporting me throughout my entire life.

Abstract

Gamma-ray bursts (GRBs), which are the most luminous electromagnetic explosions in the universe, release relativistic jets, and they are followed by a long-lived afterglows. The afterglows are due to the synchrotron emission from nonthermal electrons accelerated in relativistic shocks. Observations of GRB afterglows suggest that the magnetic field strength in the emission region is two orders of magnitude larger than the shock-compressed value. At present, the mechanism of such a field amplification process is not fully understood.

The magnetic field amplification at collisionless shocks is also an important issue for a collisionless plasma physics. The magnetic field strength determines the maximum energy of nonthermal particles accelerated at the shock. So far, the Weibel instability has been expected to be responsible for the downstream strong magnetic field. The Weibel instability is excited in a plasma with temperature anisotropy, generating magnetic fields. According to the previous particle-in-cell (PIC) simulations of relativistic shocks propagating into *homogeneous* media, the strong magnetic field generated by the Weibel instability in the shock transition region rapidly decays behind the shock, and cannot occupy the large downstream region. The coherent length of the Weibel-generated field is much smaller than the gyro-radii of high-energy particles, hence the particle acceleration becomes inefficient.

In this thesis, we performed a PIC simulation of a relativistic shock propagating into *inhomogeneous* plasma for the first time. Indeed, realistic interstellar and circumstellar media are in general turbulent and perturbed. It is found that the post-shock magnetic field decays slowly compared with the homogeneous case. The density fluctuation, whose wavelength is two or three orders of magnitude larger than plasma skin-depth, generates the downstream large-scale magnetic field. The sound waves as well as entropy waves are also formed by the interaction between the shock wave and the upstream density fluctuation. The sound waves and the diffusion of high-energy particles produce large-scale temperature anisotropy in the downstream region. The free energy of the temperature anisotropy is large enough to make the field strength suggested by GRB observations. Our results show that the upstream inhomogeneity plays an important role in the emission process of GRB afterglows.

Contents

Chapter 1

Introduction

The first gamma-ray burst (GRB) was discovered by the military satellite, Vela, in 1967 (Klebesadel et al., 1973). The GRBs are astrophysical transients which release short (from ~ 10 msec to ~ 100 sec), intense gamma-ray pulses with a non-thermal spectrum peaking at energies $\sim 10-10^4$ keV (Bošnjak & Daigne, 2014). There are two classes of GRBs: long and short GRBs (Kouveliotou et al., 1993). The former has the typical duration $\sim 10-100$ s, and its progenitor is thought to be a massive star (e.g. Stanek et al., 2003). The duration of the latter is typically ~ 0.1 s, which is caused by the merger of binary neutron stars (e.g. Gehrels et al., 2005; Abbott et al., 2017).

The isotropic distribution of GRBs' arrival direction puzzled many astronomers about whether the GRBs are Galactic or extragalactic (Nemiroff, 1995; Paczynski, 1995; Lamb, 1995). Since the discovery of GRB afterglows by BeppoSAX satellite in 1997 (Costa et al., 1997), follow up multi-wavelength observations of GRBs have been carried out. The red-shifted absorption lines in the observed optical counterparts to the GRBs gave a smoking-gun evidence for the cosmological distance to the GRB (Metzger et al., 1997). Nowadays, afterglows in various wavelengths from radio to very-high-energy gamma-rays have been observed to last for a day, month, or even years (Costa et al., 1997; Sahu et al., 1997; Frail et al., 1997; Ajello et al., 2019a). For GRBs with known redshift, we can estimate the isotropic-equivalent gamma-ray energy $E_{\gamma,\rm iso} \sim 10^{49}$–$10^{55}$ erg (Amati et al., 2002). Hence, GRBs are extremely explosive phenomena in the Universe. In order for such a huge amount of energy to be released in a few seconds, GRBs must be accompanied with relativistic plasma jets ejected from central engines (Piran, 2000). Some nearby GRBs have shown the superluminal motion of the radio afterglow as an evidence for the relativistic jet (Taylor et al., 2004; Mooley et al., 2018).

Although the jet dynamics and the radiation mechanism have not been still understood, the standard model describing a general picture of GRB, so called internal-external shock model, is established through theoretical modelings and the multi-wavelength observations (Paczynski & Rhoads, 1993; Mészáros & Rees, 1997; Waxman, 1997; Wijers et al., 1997; Harrison et al., 1999; Rhoads, 1999). The multiple internal shocks are formed in the jet due to non-uniform velocity distribution in relativistic plasma outflows where the kinetic energy of the bulk flow is partially dissipated (Meszaros & Rees, 1992; Paczynski & Rhoads, 1993; Katz, 1994; Sari & Piran, 1997), resulting in the prompt GRB emissions. Although this model assumes the synchrotron radiation for the emission mechanism, the predicted spectra cannot be fully explained. Understanding of the prompt emission mechanism remains puzzled. The external shocks are produced by the interaction between the jet and circumburst media (CBM). The afterglows are believed to be the synchrotron emission from non-thermal electrons accelerated in the external relativistic shock. In this model, the afterglow emission is calculated with free five parameters: the energy contained in the expanding outflow E, CBM density n, the fractions of energy of the magnetic field and relativistic electrons to the dissipated jet kinetic energy $\epsilon_{\rm B}$ and $\epsilon_{\rm e}$, and the power-law index of the electron energy distribution in the shocked plasma, $p_{\rm e}$ (Sari et al., 1998). These five parameters are determined from the fitting of rich multi-wavelength afterglow data. Although the standard model can generally explain the afterglow data, the early afterglows showing variable behaviors remains elusive. In order to explain the early afterglow light curves, various radiation mechanism and component has been proposed beyond the standard model (Katz et al., 1998; Berger et al., 2003; Lipkin et al., 2004; Yamazaki et al., 2004; Ioka et al., 2006; Uhm et al., 2012, and reference therein). In any cases, there are some uncertainties of the microphysical parameter $\epsilon_{\rm B}$ and external density n. This is partly because the problems regarding the magnetic field amplification at relativistic shocks remains unresolved.

The magnetic field amplification is also an interesting topic for collisionless plasma physics. The relativistic counter-streaming plasmas have a large temperature anisotropy which excites the Weibel instability (Weibel, 1959), generating the magnetic field. The Weibel-generated field changes the particle's momentum and forms a relativistic collisionless shock. Such physical processes occur in GRBs since interactions between the CBM and relativistic jet is collisionless. Thus, the relativistic shock in GRBs is a unique laboratory to study fundamental questions in plasma physics. So far, the magnetic field amplification in the Weibel-mediated shocks has been investigated by many particle-in-cell simulations which solve simultaneously both particle trajectories and electromagnetic field from the first principle (Silva et al., 2003; Kato, 2005; Chang et al., 2008; Keshet et al., 2009; Medvedev et al., 2011; Ruyer & Fiuza, 2018; Takamoto et al., 2018). According to their results, strong magnetic field is seen near the shock front, but the post-shock magnetic field rapidly decays (Sironi et al., 2013; Chang et al., 2008; Keshet et al., 2009). The coherent length of the generated magnetic field is ~ 10 times the plasma skin-depth. Hence, although the non-thermal particles are generated, the efficiency of the particle acceleration is low. This means that the high-energy photons are not fully generated via synchrotron emission to account for the observed afterglows in this process.

In this thesis, we study in detail the mechanism of the magnetic field amplification in the Weibel-mediated shock. The previous studies of the magnetic field amplification by the Weibel instability assumed that the external medium is homogeneous. Actually, there are some density fluctuations produced by the stellar wind or some inhomogeneity of interstellar medium (ISM). Magnetohydrodynamics (MHD) simulations have shown the field amplification by turbulent dynamo when the shock propagates into the inhomogeneous media (Sironi & Goodman, 2007; Inoue et al., 2011; Mizuno et al., 2011). For a collisionless system, the diffusive motion of high-energy particles may potentially impact on the shock structure. The energy dissipation by the particle diffusion is expected to lead to the plasma heating and particle acceleration. We believe this effect should be non-negligible since the observations suggest that a large fraction of electrons are injected into the nonthermal population. Furthermore, the kinetic plasma instability may convert the turbulent kinetic energy to the magnetic energy. Therefore, using a first principles approach, we investigate magnetic field amplification in a relativistic shock propagating into inhomogeneous media. In chapter 2, we review the observations of GRBs. In chapter 3, we describe the theoretical model of GRB afterglows. In chapter 4, we review the studies about the magnetic field amplification in GRB afterglows. In chapter 5, we will construct the model of magnetic field amplification in the downstream region of shocks propagating into inhomogeneous media, and present the result of two-dimensional PIC simulation of a relativistic shock propagating into inhomogeneous electron-positron plasma. In chapter 6, we discuss the impact of our simulation result on the magnetic field amplification in GRB afterglows and give a outlook. Finally we conclude in chapter 7.

Chapter 2

Observation of Gamma-Ray Bursts

Observational studies of GRBs have made progress due to gamma-ray and X-ray satellites (BepposSAX, KONUS/WIND, HETE-2, Swift, Integral, AGILE, Fermi) and the follow-up observations in ground-based Cherenkov, optical, infrared, milimeter and radio telescopes. In this chapter, observational properties of GRBs are summarized.

2.1 Prompt Emissions

2.1.1 Temporal Properties

The duration of the prompt gamma-ray emission is thought to reflect the active time of the central engine. The duration of a burst, T_{90}, is defined as the time interval between the epochs when 5% and 95% of the total counts of the GRB arrive. As seen in Figure 2.1, T_{90} is distributed broadly from ~ 0.01 to $\sim 10^3$ sec. The T_{90} distribution is separated into two groups: the short- and long-duration components have T_{90} of typically ~ 0.1 sec and a few tens of seconds, respectively (Kouveliotou et al., 1993). The bottom panel in Figure 2.1 shows the hardness ratio defined as the ratio of the fluence in the detector channels 3 (100–300 keV) and 4 ($>$ 300 keV). Comparing their spectral hardness ratio, the short GRBs is harder than the long GRBs, that is, short GRBs have more high-energy photons than the long GRBs. Hence, it is suggested that the origins of the short and long GRBs are different.

The light curves of the prompt emission are highly variable (Fishman & Meegan, 1995). The variability time scale, which is approximately equivalent to the pulse width, ranges between milliseconds to several tens of seconds (Norris et al., 1996). Some examples of the GRB light curves are displayed in Figure 2.2.

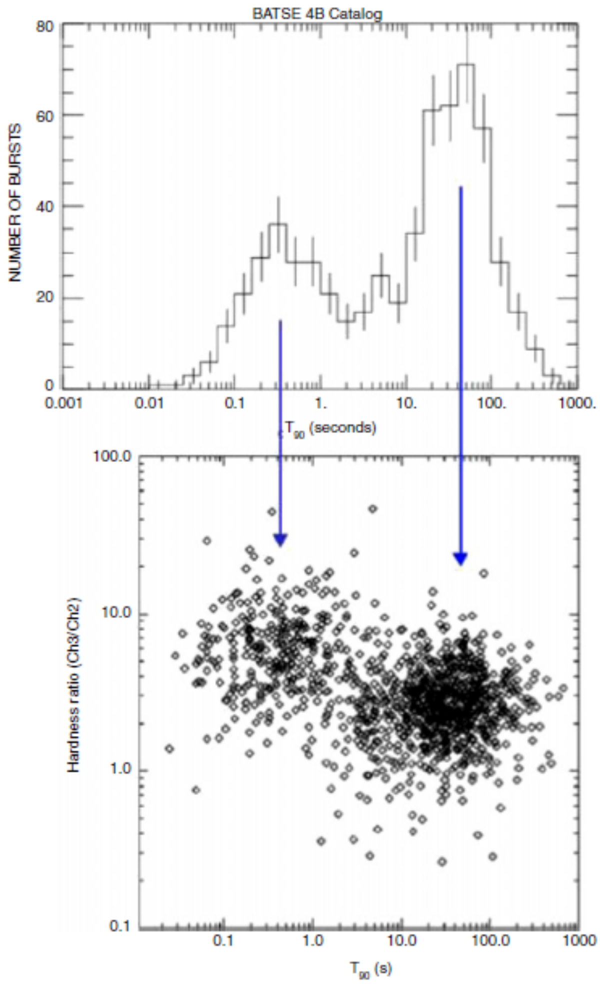

Figure 2.1: Duration distribution (top panel) and duration–hardness ratio distribution (bottom panel) of GRBs detected by BATSE on board Compton Gamma-Ray Observatory. Adapted from the BATSE 4B Catalog (http://gammaray.msfc.nasa.gov/batse/grb/catalog/).

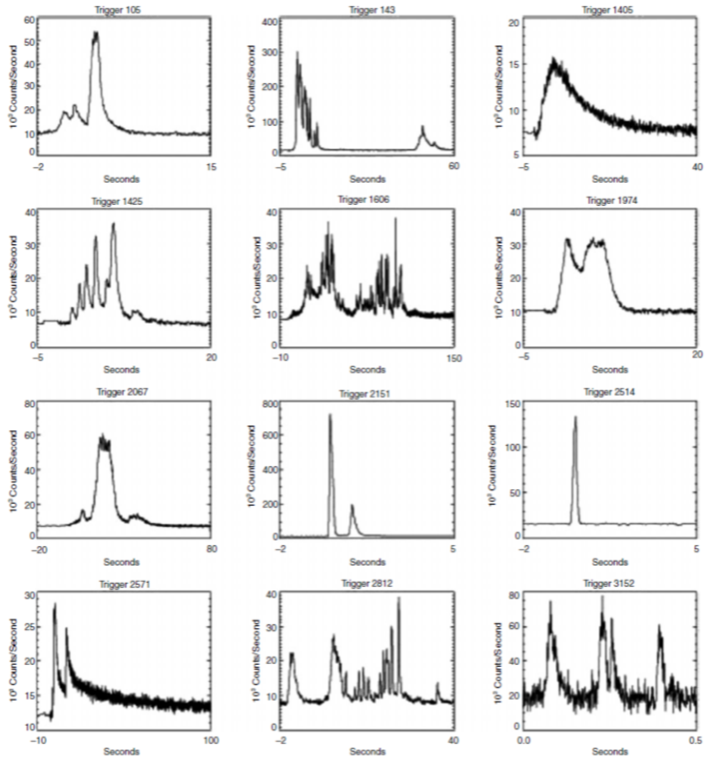

Figure 2.2: Example of the prompt gamma-ray bursts light curves. From Fishman & Meegan (1995).

2.1.2 Spectral Properties

The prompt GRB emission is non-thermal. The observed νF_ν-spectrum peaks at a few hundred keV and sometimes has a tail extending up to GeV energy range. Although the observed spectra are different depending on events, they are fitted with two power laws joined smoothly at a break energy around E_0, which is known as the Band function (Band et al., 1993):

$$N(E) \propto \begin{cases} E^\beta \exp\left(-\frac{E}{E_0}\right) & E < (\alpha-\beta)E_0 \\ [(\alpha-\beta)E_0]^{\alpha-\beta} E^\beta \exp(\beta-\alpha) & E \geq (\alpha-\beta)E_0 \end{cases}, \tag{2-1-1}$$

where α and β are the photon indices below and above the break energy E_0, respectively. The peak energy E_p of the spectral energy distribution $E^2N(E)$ is given by $E_p = (2+\alpha)E_0$ for $\alpha > -1$. For example, as shown in Figure 2.3, the prompt emission spectrum of GRB 990123 is well fitted by the Band function. Figure 2.4 shows the distributions of E_0, α, and β for the bright GRBs observed with the Burst and Transient Source Experiment (BATSE) covering an energy range from 30 keV to 2 MeV (Preece et al., 2000). It is found that the average values are $E_\mathrm{p} \sim 250$ keV, $\alpha \sim -1 \pm 1$, and $\beta \sim -2^{+1}_{-1}$. The number of events with smaller E_p increases if the GRBs are observed by HETE-2/WXM and Swift/BAT that are sensitive to lower-energy photons than BATSE (Sakamoto et al., 2005, 2008)

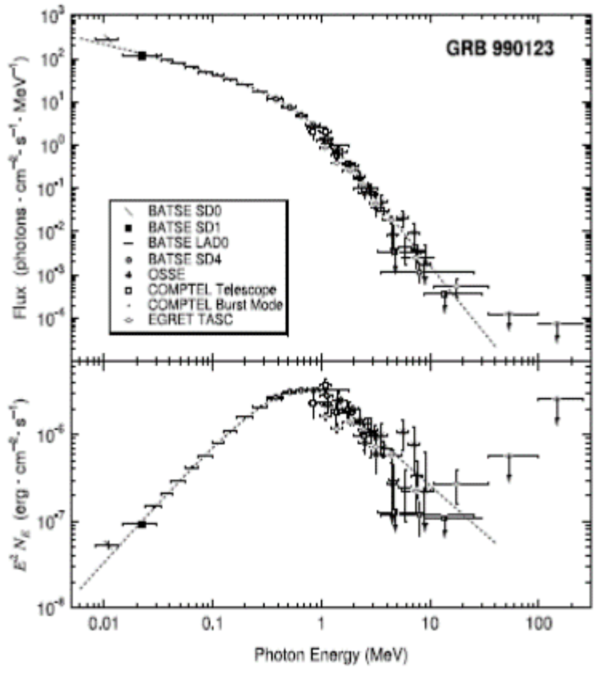

Figure 2.3: Prompt emission spectrum of GRB 990123. From Briggs et al. (1999).

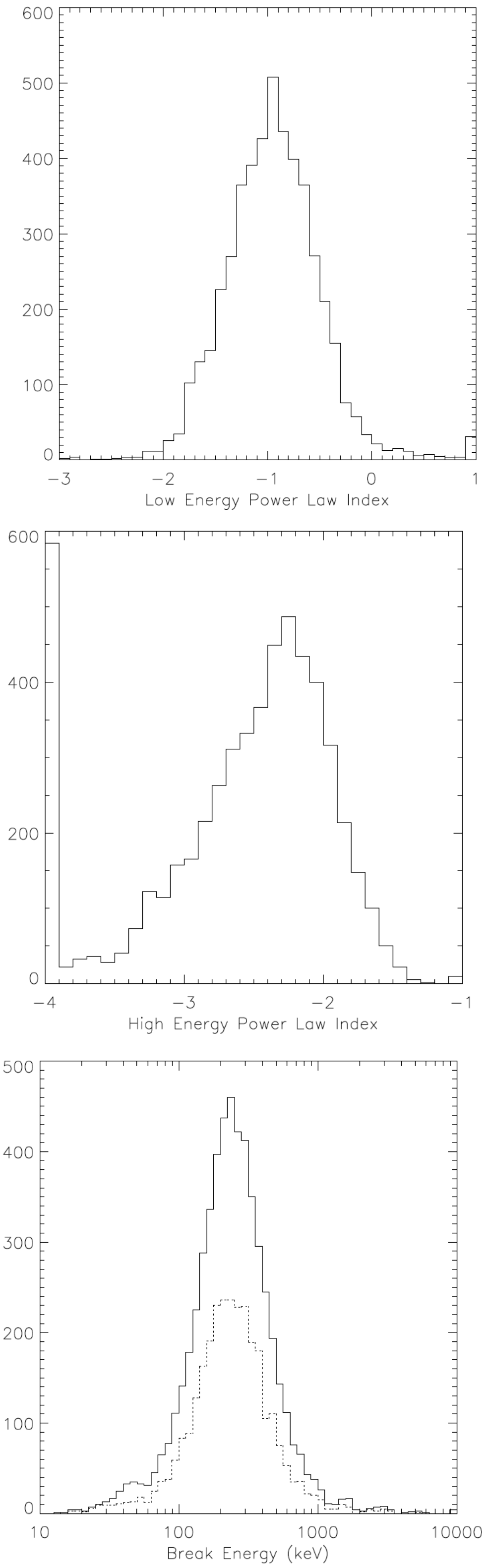

Figure 2.4: Distributions of low- (upper) and high-energy (middle) power-law index, and the break energy E_0 (botom). From Preece et al. (2000).

2.2 GRB Afterglows

Paczynski & Rhoads (1993) and Mészáros & Rees (1997) predicted that broadband afterglows were detectable after the prompt emissions. According to their external-shock model, the relativistic outflow from a GRB progenitor interacts with the circumburst media (CBM), forming the external forward and reverse shock waves. Afterglows are assumed to be synchrotron emission from non-thermal electrons accelerated by the relativistic shocks. As the flow decelerates, multi-wavelength afterglows decay with a power-law-like nature.

A GRB afterglow flux at any given time depends on the five parameters: energy in expanding outflow except for the energy in prompt emission E, the external medium density $n_{\rm ex}$, the energy fraction in magnetic field (electron) that is given by the dissipated jet kinetic energy $\epsilon_{\rm B(e)}$, and the power-law index of electron energy distribution with non-thermal tail in shocked plasma $p_{\rm e}$. In the simplest version of the afterglow model, these parameters are considered to be constant (Sari et al., 1998). A broadband afterglow spectrum has a power-law shape which breaks at three characteristic frequencies, $\nu_{\rm a}$, $\nu_{\rm c}$, and $\nu_{\rm m}$ (see section3). In the early afterglow phase ($< 10^{2-3}$ sec), the relation $\nu_{\rm c} < \nu_{\rm m}$ is expected, in which non-thermal electrons lose a significant fraction of their energy due to radiation. This is called the "fast cooling" regime. In the late phase, we see $\nu_{\rm c} > \nu_{\rm m}$ ("slow cooling" regime). Then, only a part of high-energy electrons cools down. When the characteristic frequencies cross over the observed band, the behavior of light curves changes. Given the five parameters, afterglow light curves are represented as $F_\nu \propto \nu^{-\beta} t^{-\alpha}$.

The above theoretical model can fit overall afterglow lightcurves, namely in the later epoch. However, there are also a large number of observed afterglows unexpected from the standard model. In this section, the observational properties of GRB afterglows and the plausible interpretation are summarized.

2.2.1 Late-Time (≥ 10 hr) Afterglow Phase

The X-ray afterglow of GRB 970228 was first discovered by Narrow Field Instrument (NFI: covering energy band 0.1–300 keV) onboard the BeppoSAX satellite (Costa et al., 1997), and the burst location was determined within 4 arc-minutes. Owing to better accurate position determination, the optical afterglow was discovered on 8 hours after the detection of the burst by the follow-up observation by Hubble Space Telescope (Sahu et al., 1997). Furthermore, the host galaxy of the burst was identified, where atomic/molecular absorption lines were observed and gave a redshift of $z = 0.695$ (Bloom et al., 2001). The X-ray and optical afterglows decayed as $F_\nu \propto t^{-1.33^{+0.13}_{-0.11}}$ (Costa et al., 1997) and $F_\nu \propto t^{1.10\pm0.04}$ (Galama et al., 1997), respectively.

Radio afterglow was discovered in GRB 970508 by Very Large Array (VLA) at 0.15 days after the burst in 1.4 GHz band (Frail et al., 1997). Both absorption and emission lines were observed from the optical spectrum of GRB 970508 and provided the redshift of $z = 0.835$. Figure 2.5 shows the radio light curve of GRB970508 observed in 4.8 GHz band. The radio flux has a peak at 10 days and decays as $t^{-1.14}$ at $t > 100$ days. The light curve has a large fluctuation, which is suggested to be due to scintillations (Goodman, 1997). From the constrained size of the emission region and Lorentz factor, it was found that a GRB outflow is relativistic. In addition, a superluminal expansion of the radio afterglow was observed for GRB 030329 by Very Long Baseline Interferometry (VLBI) campaign using six radio observatories, and indicated that the blast waves were still mildly relativistic several weeks after the GRB detection (Taylor et al., 2004).

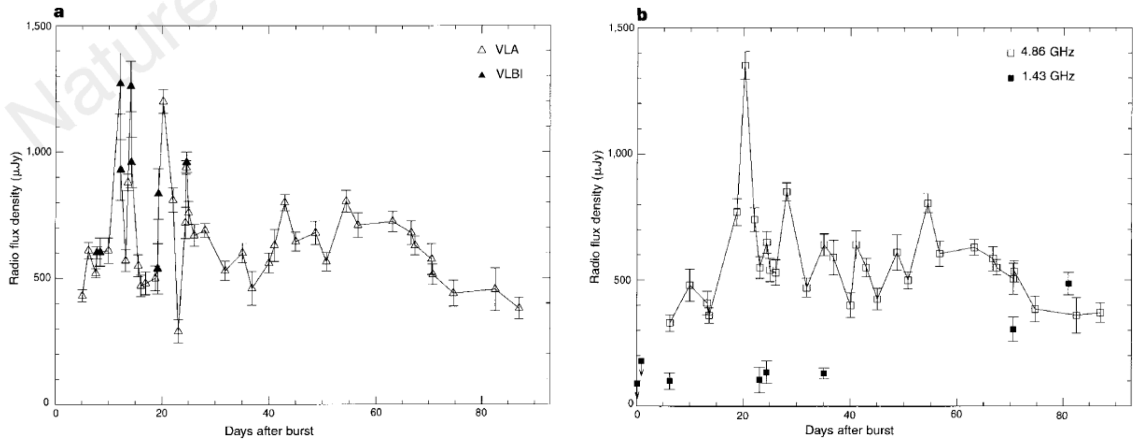

Figure 2.5: Radio light curve of GRB 970508. Panel **a** shows light curves at 8.46 GHz band given by Very Large Array (open triangle) and Very Long Baseline Interferometry (filled triangle) data. Panel **b** shows 1.43 and 8.46 GHz light curves in VLA and VLBI. From Frail et al. (1997).

Since the discovery of the GRB afterglows, a large amount of late time ($t > 10$ hr) afterglow data were obtained by multi-wavelength follow-up observations. The late time X-ray and optical afterglows generally decay as $F_\nu \propto t^{-\alpha}$, with $\alpha \sim 1$, and have a power-law spectrum as $F_\nu \propto \nu^{-0.9\pm0.5}$ (e.g. Wijers et al., 1999). At ~ 1 day after the burst trigger, each temporal index of the X-ray and optical afterglow light curves become steeper, as $F_\nu \propto t^{-2}$ (Harrison et al., 1999). Such a temporal steepening, which is inconsistent with a radiation from spherical blast-wave, is expected to be seen for the case of a collimated outflow as a jet (Rhoads, 1999). When the relativistic jet slows down, the opening angle of the jet increases, so that the outflow suddenly decelerates, reducing the relativistic beaming effect. As a result, X-ray and optical afterglow flux decrease, making a sudden break in the observed light curves. This break is called the "jet break" (Sari et al., 1999). The light curve of radio afterglows rises as $t^{0.5}$ from a few days after the burst trigger and peaks at ~ 10 days, after which it decays as t^{-1}. These behaviors are consistent with the prediction of the external-forward shock model (Figure 2.6).

2.2.2 Early-Time Afterglow Phase

While late-time afterglows can be explained by the standard model, early afterglow data observed by X-ray telescope (XRT: 0.2–10 keV) and UV-optical telescope (UVOT) onboard *Swift* satellite have much more complex behaviors than expected in the pre-Swift era. The features of early ($< 10^5$ sec) afterglows are summarized as follows.

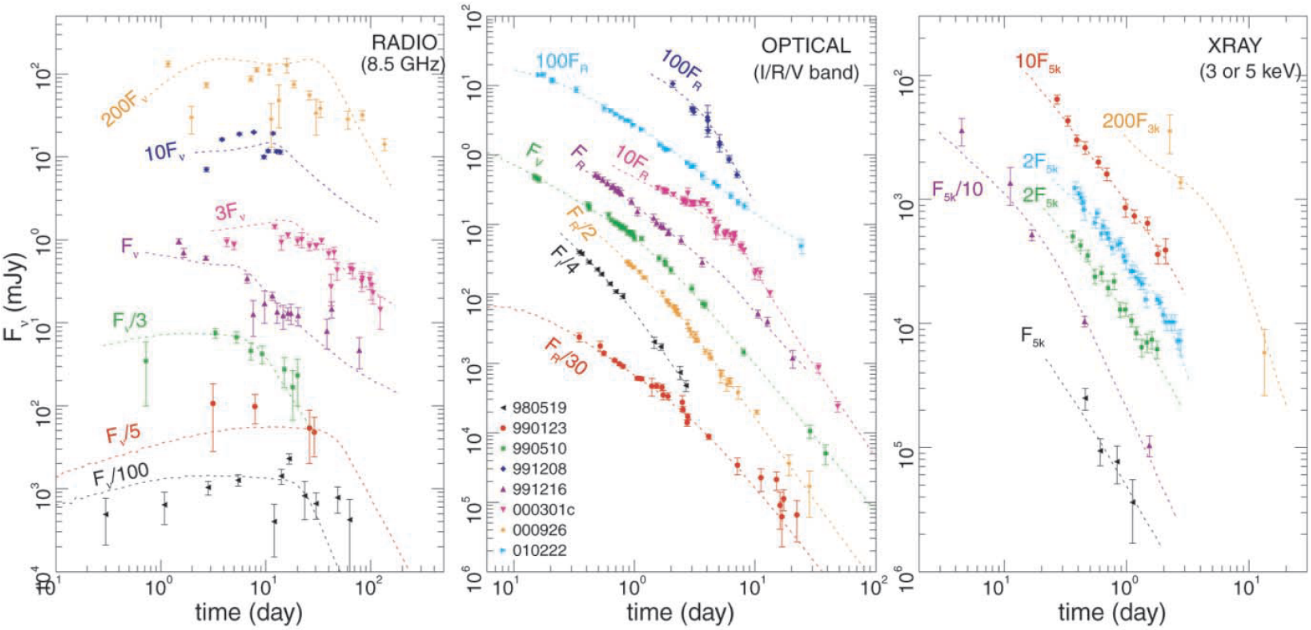

Figure 2.6: Radio, optical, and X-ray model light curves for the GRB afterglows 980519, 990123, 990510, 991208, 991216, 000301c, 000926, and 010222 (the definition of the symbols inside the middle panel applies to all panels). The model light curves were be obtained by the minimization of χ^2 between the model emission and the radio, millimeter, submillimeter, near-infrared, optical, and X-ray data. From Panaitescu & Kumar (2001).

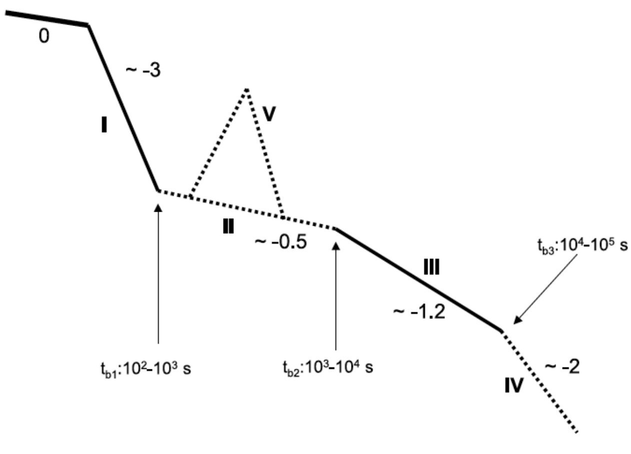

Figure 2.7: Schematic diagram of typical X-ray light curve. I: steep decay phase. II: shallow decay or plateau phase, III: normal decay phase, and IV: X-ray flares. From Zhang et al. (2006).

Figure 2.7 shows a synthetic cartoon of the X-ray light curve based on the observational data from the Swift XRT, which has five components as described below (Nousek et al., 2006; Zhang et al., 2006).

- I. An early-time steep decay phase: a temporal decay index is steeper than $\alpha \sim -2$ during several hundred seconds after the GRB trigger. This component may be the tail of the prompt emission because for some BAT GRBs, the spectral extrapolation of the prompt emission connects to the steep decay phase smoothly (O'Brien et al., 2006). Therefore, the early time steep decay phase is thought to be unrelated to the external shock emission.

- II. Shallow decay phase (or plateau phase): the decay slope of light curves becomes shallow ($\alpha \sim 0.5$) or flat at around $10^2 - 10^3$s. The shallow or plateau phase continues during a few $10^3 - 10^4$ s and is followed by a "normal" decay phase (see below). Even though external shocks generally start to decelerate in this phase, the X-ray flux decays slower than the prediction of the standard model. It is suggested that the shallow decay component is attributed to continuous energy injection from a central engine (Zhang et al., 2006). This means that less energy is contained at the initial stage of the afterglow just after the prompt emission, that is, the gamma-ray efficiency should be very high. This may lead an efficiency crisis in the context of the synchrotron-shock model of the prompt gamma-ray emission (Ioka et al., 2006).

- III. Normal decay phase: Most GRBs have the normal decay phase in which the flux decays with time as t^{-1} after the shallow decay or plateau phase. This is a typical feature expected in the standard external-forward shock model in the pre-Swift era.

- IV. Late steep decay phase: the shallow-to-steep transition at $\sim 10^5$ s is as expected in the external-forward shock model, which corresponds to the "jet break".

- V. X-ray flares: one or more flares are typically seen during the shallow decay phase (Burrows et al., 2005). The amplitudes of the flares are much larger than that of the typical shallow-decay component, so that it is believed that the origin of the flares is not the density variations of CBM but the central engine activity (Ioka et al., 2005; Zhang et al., 2006).

Some early optical follow-up observations detected the beginning of optical afterglows. The early optical afterglow of GRB 060418 showed that the flux increased with time as $t^{2.7^{+1.7}_{-1.0}}$ and peaked typically at ~ 100 s after the burst detection (Molinari et al., 2007). The peak time of the optical afterglow was interpreted as the start of the deceleration of the blast wave, which enables us to infer the initial Lorentz factor of a shock, $\Gamma_0 \sim 100$ (see section 3). After the peak, the optical flux simply decreases without changing the temporal index until the jet break. Some optical and X-ray light curves showed wiggles and bumps which significantly derivate from a smooth power-law (Holland et al., 2003; Bersier et al., 2003; Jakobsson et al., 2004; Lipkin et al., 2004). Such an afterglow variability will have a wealth of information about GRB jet, the central engine, and the CBM. One of the possibility of the temporal variability is thought to be inhomogeneity of the ambient media (Dai & Lu, 2002; Lazzati et al., 2002; Dai & Wu, 2003; Heyl & Perna, 2003; Nakar et al., 2003). The short-term variability (e.g. that is included for the afterglow light curve of GRB 011211 and GRB 021004) is expected to be due to a late-time energy injection from the central engine rather than the density fluctuation (Katz et al., 1998; Kumar & Piran, 2000a; Zhang et al., 2002; Granot et al., 2003). Moreover, angular energy fluctuations within a GRB jet (Kumar & Piran, 2000b; Yamazaki et al., 2004) and two component jet model (Berger et al., 2003; Huang et al., 2004; Racusin et al., 2008) are proposed as the origin of such a temporal variability of the afterglows.

Simultaneous X-ray and optical observations of the early afterglow may help us understanding the physics of the external shock emission. For example, in Figure 2.8, the X-ray (upper panel) and the optical (bottom panel) luminosities at 11 hours after the burst are plotted as a function of the isotropic gamma-ray energy of the prompt GRB emission $E_{\gamma,\mathrm{iso}}$ (Nysewander et al., 2009). The afterglow luminosities in both the X-ray and optical bands are proportional to the prompt gamma-ray fluence. These correlations may imply that the emission mechanism of the X-ray (except the component I) and optical afterglows is the same. However, this is not exactly true because of "chromatic" behavior of X-ray and optical light curves in the early afterglow. For a large fraction of events, there is no break in the optical light curve at the transition from shallow to normal decay phase in the X-ray light curve (Panaitescu et al., 2006). If the X-ray shallow decay component is due to the continuous energy injection, the optical light curve must also show the break simultaneously with the shallow-to-normal transition in the X-ray light curve.

Since the standard model cannot explain such a chromatic behavior, multi-component emissions are required. For example, the two-component jet model assumes that emission regions are different between X-ray and optical, that is, X-ray (optical) emission are produced in a narrow (wide) jet with higher (lower) Lorentz factor. This model can fit some afterglow data (Racusin et al., 2008); however, more parameters are needed and significantly variable from burst to burst (De Pasquale, 2009). Uhm & Beloborodov (2007) and Genet et al. (2007) proposed that afterglow emission are produced not only in the forward shock but in the long-lasting reverse shock. A reverse shock emission is generally expected to be short-lived and dimmer than the forward-shock emission for the same ϵ_{B} and ϵ_{e} in both shocks (Sari & Piran, 1999). On the other hand, Uhm et al. (2012) and Uhm & Zhang (2014) showed that a reverse-shock emission colud explain variable light curves of X-ray and optical afterglows because the strength of the reverse shock sensitively depends on the burst ejecta stratifications. However, their models assume that ϵ_{B} and ϵ_{e} in the reverse shock are higher than in the forward-shock. It is not understood how the brightness of forward-shock emissions are suppressed. Alternatively, there is also a possibility that the evolving microphysics parameters, ϵ_{B} and ϵ_{e}, could produce the shallow decay phase and the chromatic break (Ioka et al., 2006; Fan & Piran, 2006; Granot et al., 2006). Ioka et al. (2006) showed that in order to explain the absence of the optical break at the end of the X-ray shallow decay phase, the magnetic fraction ϵ_{B} decreases with time as $t^{-0.6}$. Although particle-in-cell simulations have also shown that the magnetic field decay with time (Silva et al., 2003; Kato, 2005; Chang et al., 2008; Keshet et al., 2009; Takamoto et al., 2018), it has not been evidenced that particles are accelerated to high energy in the decaying magnetic field within the dynamical time.

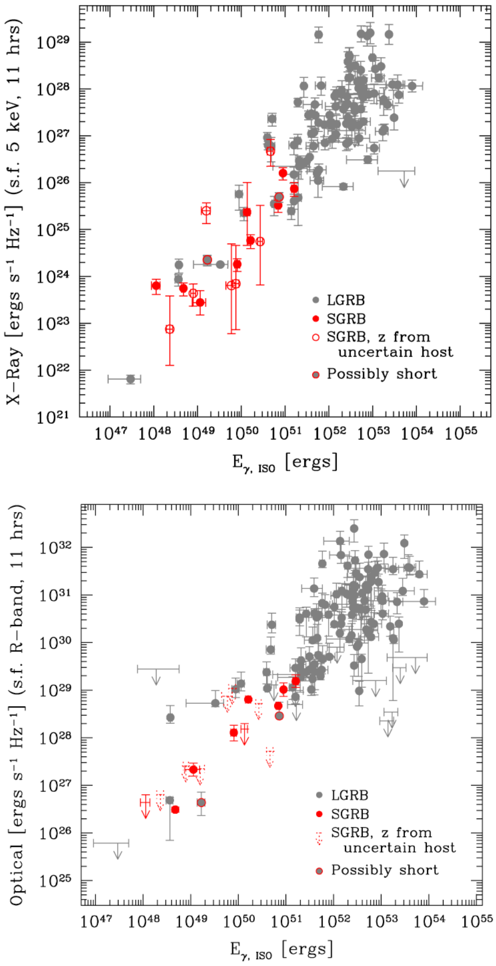

Figure 2.8: The upper panel shows the X-ray (5 keV) afterglow luminosity at 11 hr after the GRB detection in the source frame, as a function of the isotropic equivalent gamma-ray energy of the prompt GRB emission $E_{\gamma,\rm iso}$. The bottom panel shows the same as the upper figure but for the optical R-band afterglow luminosity. From Nysewander et al. (2009).

2.2.3 High-Energy (GeV–TeV) Afterglow Emission

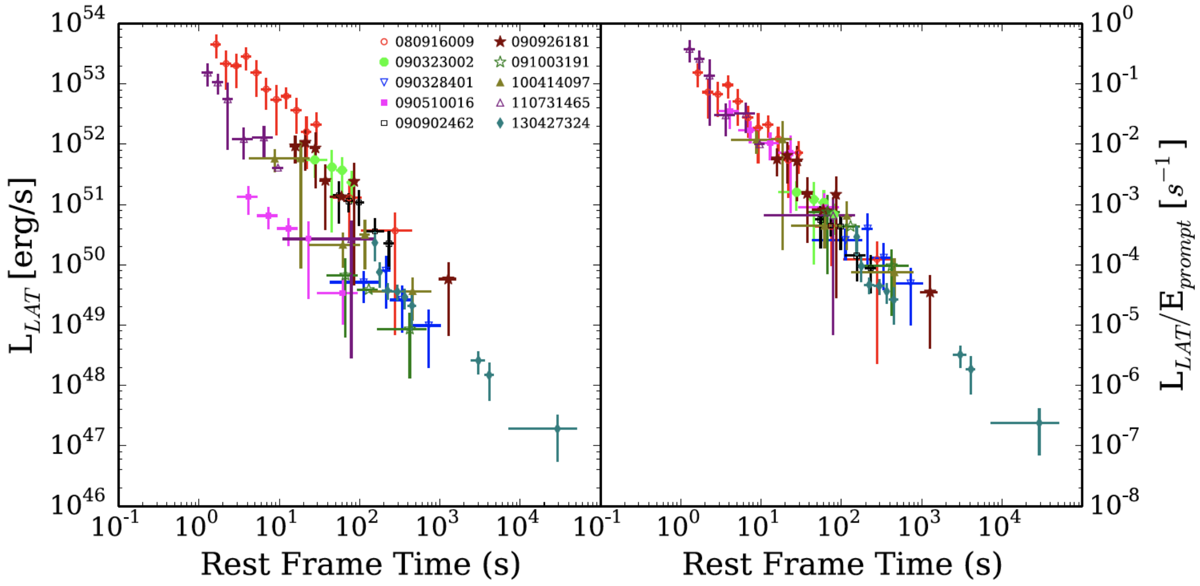

Figure 2.9: Left panel: afterglow light curves in the 0.1–10 GeV energy range for 10 GRBs, where the energy and time since the burst trigger is measured in the cosmological rest frame. Right panel: the 0.1–10 GeV luminosity is normalized by the prompt gamma-ray energy which is estimated from the GBM in the 1 keV–10 MeV band. From Nava et al. (2014).

From some bright GRBs, $0.1-10$ GeV gamma-ray emissions are detected by Fermi/LAT ($\geq 10^2$ MeV) from a few second after the time of the Fermi/GBM (~ 5 keV–10 MeV) trigger (Ajello et al., 2019a) up to 10^3 s (Figure 2.9). Furthermore, recently MAGIC Cherenkov telescope detected photons above 300 GeV with more than 20σ significance from BAT triggered GRB 190114C (Ajello et al., 2019b; Mirzoyan, 2019). Observed LAT light curves are usually characterized by a simple power-law decay with the spectral index ~ 1 (Abdo et al., 2009a,b; Ghisellini et al., 2010; Zhang et al., 2011; Nava et al., 2014). The LAT data for GRB 190114C also showed similar behaviors (Ajello et al., 2019b). In most cases, the spectral feature in the GeV band is consistent with a spectrum of synchrotron emission from external shock in the fast cooling ($\nu > \nu_c$) phase (Kumar & Barniol Duran, 2010; Ghisellini et al., 2010). Thus, the delayed GeV emissions is expected to be produced by synchrotron emission from electrons accelerated in the external shock. However, the maximum synchrotron photon energy is given by $\sim 0.1\Gamma$ GeV, and it is barely able to explain the LAT data if the bulk Lorentz factor Γ is below 100 in the afterglow phase. Alternatively, a proton synchrotron emission and an inverse Compton scattering of synchrotron photons (SSC: synchrotron self-Compton) or external photons (EC: external Compton) are thought to be the other candidates for the origin of the GeV emission. For the emission above 300 GeV, its origin should not be synchrotron but SSC or EC (Wang et al., 2019; Derishev & Piran, 2019; Zhang et al., 2019).

The detection of GeV/TeV gamma-ray photons allows us to constrain the physical parameters regarding the emission process like magnetic field strength. It is thought that the required kinetic energy in the external shock wave becomes larger when the GeV emission is considered (Ajello et al., 2019a). The initial bulk Lorentz factor of the jet also tends to be larger (Ghirlanda et al., 2012). Despite these facts, the observed X-ray and optical afterglows are not so bright. This means that the synchrotron cooling is not effective in the X-ray and optical bands, in particular we expect the cooling frequency ν_c is above the X-ray band. Therefore, the magnetic field in the shocked region may not so strong (Tak et al., 2019) compared with the expected value $\epsilon_B \sim 10^{-2}$ before the era of GeV detections (Kumar & Barniol Duran, 2009, 2010). When it is assumed that the GeV/TeV photons are produced by EC, the ratio of the peaks in the afterglow spectrum of the synchrotron and inverse Compton emissions gives us the upper limit on ϵ_B. According to this ratio, the detection of $<$ TeV photons suggests $\epsilon_B \sim 10^{-5}$ (Zhang et al., 2019). It should be noted that, within such a weak magnetized medium, it is uncertain whether electrons are accelerated to high-energy enough to emit the synchrotron X-rays. Therefore, the radiation mechanisms which can explain the emission extending from sub-GeV to sub-TeV is an open question. Further detection of $>$ 10 GeV photons by MAGIC, H.E.S.S., HAWC[1], as well as upcoming CTA[2] will provide more stringent constraints on the afterglow radiation mechanisms.

[1]High-Altitude Water Cherenkov Gamma-ray observatory (HAWC) covers the energy range from100 GeV to 100 TeV.

[2]Cherenkov Telescope Array (CTA) covers gamma-ray energy range from 20 GeV to 300 TeV

Chapter 3

Standard Model of GRB Afterglows

3.1 Nonthermal Electrons and Magnetic Fields in the External Shocked Region

We derive theoretical light curves of GRB afterglows in this chapter (Sari et al., 1998, for review). We consider a relativistic shock propagating with a Lorenz factor, $\Gamma_{\rm sh}$, through a uniform medium with a number density, n. Physical quantities in the shock downstream region are obtained from that in the shock upstream region by conservation laws of number density, momentum, and energy fluxes, that is, the Rankine-Hugoniort relations. The downstream number density, n_2, and internal energy density, e_2, measured in the fluid frame ($'$) are given by

$$e_2^{'} = 4\Gamma^2 n m_{\rm p} c^2 \tag{3-1-1}$$
$$n_2^{'} = 4\Gamma n \ , \tag{3-1-2}$$

where $\Gamma = \Gamma_{\rm sh}/\sqrt{2}$ is the Lorentz factor of shocked fluid measured in the upstream rest frame, and $m_{\rm p}$ and c are the proton mass and speed of light, respectively (Blandford & McKee, 1976).

In the standard model of the GRB afterglow, the post shock electrons are assumed to be accelerated in the shock. The energy distribution function of the post-shock electrons in the downstream rest frame is written by

$$\frac{dN^{'}}{d\gamma_{\rm e}^{'}} = A\gamma_{\rm e}^{'-p} \ \ (\text{for} \ \ \gamma_{\rm e,min}^{'} \leq \gamma_{\rm e}^{'} \leq \gamma_{\rm e,max}^{'}) \ \ , \tag{3-1-3}$$

where $\gamma_{\rm e,min}^{'}$ and $\gamma_{\rm e,max}^{'}$ are the minimum and maximum Lorentz factors of electrons, and A and p are the normalization factor and the power-law index, respectively. Then, the number and energy densities of electrons are given by

$$
\begin{aligned}
U'_{\rm e} &= \int \frac{dN'}{d\gamma'_{\rm e}} m_{\rm e} c^2 d\gamma'_{\rm e} \\
&= A m_{\rm e} c^2 \int_{\gamma'_{\rm e,min}}^{\gamma'_{\rm e,max}} \gamma'^{1-p}_{\rm e} d\gamma'_{\rm e} \\
&\approx A m_{\rm e} c^2 \frac{\gamma'^{2-p}_{\rm e,min}}{p-2},
\end{aligned}
\tag{3-1-4}
$$

$$
\begin{aligned}
n'_2 &= \int \frac{dN'}{d\gamma'_{\rm e}} d\gamma_{\rm e} \\
&= A \int_{\gamma'_{\rm e,min}}^{\gamma'_{\rm e,max}} \gamma'^{-p}_{\rm e} d\gamma'_{\rm e} \\
&\approx A \frac{\gamma'^{1-p}_{\rm e,min}}{p-1}\ ,
\end{aligned}
\tag{3-1-5}
$$

where power-law index is assumed to be $p > 2$. The downstream electron energy density, $U'_{\rm e}$ is also expressed by $\epsilon_{\rm e} e'_2$ with a microphysics parameter $\epsilon_{\rm e}$. Therefore, the minimum Lorentz factor is given by

$$\gamma'_{\rm e,min} = \epsilon_{\rm e} \frac{p-2}{p-1} \frac{m_{\rm p}}{m_{\rm e}} \Gamma \cong 610 \epsilon_{\rm e} \Gamma, \tag{3-1-6}$$

where we used a typical power-law index of $p = 2.5$ for X-ray and optical afterglow data.

The downstream magnetic field strength in the downstream rest frame is given by

$$B'_2 = (32\pi n \epsilon_{\rm B} m_{\rm p})^{1/2} \Gamma c\ \ , \tag{3-1-7}$$

where $\epsilon_{\rm B} = B'^2_2 / 8\pi e'_2$. In the standard model, the parameters $p, \epsilon_{\rm B}$, and $\epsilon_{\rm e}$ are considered to be constant with time.

3.2 Radiation Spectrum of GRB Afterglows

The power and the characteristic frequency of synchrotron radiation from a single electron in the observer frame are

$$P(\gamma'_{\rm e}) = \frac{4}{3} \sigma_{\rm T} c \gamma'^2_{\rm e} \Gamma^2 \frac{B'^2_2}{8\pi}\ , \tag{3-2-8}$$

$$\nu_{\rm syn}(\gamma'_{\rm e}) = 0.29 \gamma'^2_{\rm e} \Gamma \frac{e B'_2}{2\pi m_{\rm e} c}\ , \tag{3-2-9}$$

where $\sigma_{\rm T}$ is the Thomson cross section (Rybicki & Lightman, 1979). The synchrotron spectrum below $\nu_{\rm syn}(\gamma'_{\rm e})$ is a power law form with $P_\nu \propto \nu^{1/3}$, and it decays exponentially for $\nu > \nu_{\rm syn}(\gamma'_{\rm e})$ (Figure 3.1). Since Eq. (3-2-8) is the power integrated over the frequency

$(P(\gamma_{\rm e}^{'}) = \int_0^\infty P_\nu(\gamma_{\rm e}^{'})d\nu)$, the peak value of the synchrotron spectrum at the characteristic frequency, $\nu_{\rm syn}$, is

$$P_{\nu,\rm max} \approx \frac{P(\gamma_{\rm e}^{'})}{\nu_{\rm syn}(\gamma_{\rm e}^{'})} = \frac{m_{\rm e}c^2\sigma_{\rm T}}{3q_{\rm e}}\Gamma B_2^{'} \ . \tag{3-2-10}$$

Note that the peak of the synchrotron spectrum does not depend on the Lorentz factor of electrons, $\gamma_{\rm e}^{'}$.

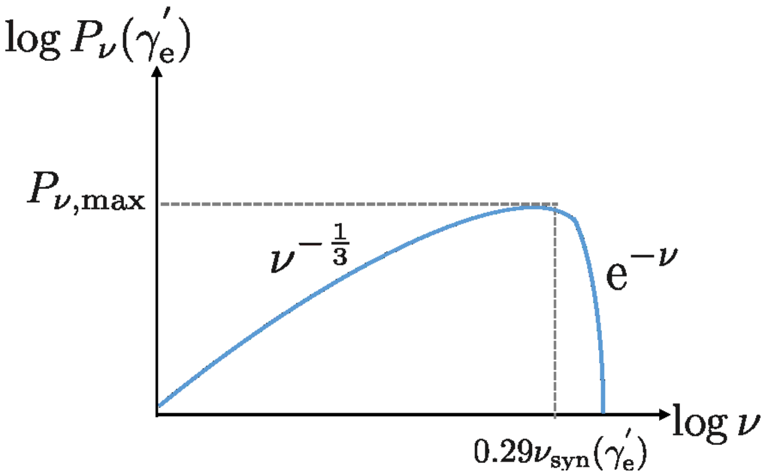

Figure 3.1: A synchrotron spectrum from a single electron.

Electrons accelerated at the shock lose their energy via the synchrotron emission for a time defined as cooling time, $t_{\rm cool}$:

$$t_{\rm cool} = \frac{\Gamma\gamma_{\rm e}^{'}m_{\rm e}c^2}{P(\gamma_{\rm e}^{'})} = \frac{6\pi m_{\rm e}c}{\sigma_{\rm T}B_2^{'2}\gamma_{\rm e}^{'}\Gamma} = 1.3\times10^{-6}\left(\frac{B_2^{'}}{10^5\rm G}\right)^{-2}\left(\frac{\Gamma}{10^2}\right)^{-1}\left(\frac{\gamma_{\rm e}^{'}}{600}\right)^{-1}\ {\rm s}\ . \tag{3-2-11}$$

At $t = t_{\rm cool}$, the Lorentz factor of electrons decreases to $\gamma_{\rm c}^{'}$:

$$\begin{aligned}\gamma_{\rm c}^{'} &= \frac{6\pi m_{\rm e}c}{\sigma_{\rm T}\Gamma B'^2 t} \\ &= \frac{3m_{\rm e}}{16\epsilon_{\rm B}\sigma_{\rm T}m_{\rm p}c}\frac{1}{t\Gamma^3 n}\ ,\end{aligned} \tag{3-2-12}$$

where we used Eq. (3-1-7). We can define a characteristic frequency here, $\nu_{\rm c} \equiv \nu(\gamma_{\rm c}^{'})$. In reality, the cooling time is shorter than the dynamical time scale. Therefore, the cooling changes the energy spectrum of electrons in the shock downstream region. Hereafter, we omit the primes from all quantities defined in the shock downstream frame.

The continuity equation in the energy space is given by

$$\frac{\partial}{\partial t}\left(\frac{\partial N}{\partial\gamma_{\rm e}}\right) + \frac{\partial}{\partial\gamma_{\rm e}}\left(\dot{\gamma}_{\rm e}\frac{\partial N}{\partial\gamma_{\rm e}}\right) = S(\gamma_{\rm e})\ , \tag{3-2-13}$$

where $\dot{\gamma}_{\rm e} = -\gamma_{\rm e}/t_{\rm cool} \propto -\gamma_{\rm e}^{-2}$ and $S(\gamma_{\rm e})$ is the source term of nonthermal electrons in the shock downstream region. For simplicity, we here consider steady-state solutions of the above equation.

For $\gamma_c < \gamma_e < \gamma_{e,mim}$, because of $S(\gamma_e) = 0$, the steady-state continuity equation is reduced to

$$\frac{\mathrm{d}}{\mathrm{d}\gamma_e}\left(\dot{\gamma}_e \frac{\mathrm{d}N}{\mathrm{d}\gamma_e}\right) = 0 \quad .$$

The solution to the above equation is given by

$$\frac{\mathrm{d}N}{\mathrm{d}\gamma_e} \propto \gamma_e^{-2} \ . \tag{3-2-14}$$

In this case, the synchrotron spectrum in the frequency range, $\nu_c < \nu < \nu_m \equiv \nu(\gamma_{e,min})$, is

$$\begin{aligned} F_\nu &\propto \int_{\gamma_{e,c}}^{\gamma_{e,mim}} P_\nu(\gamma_e)\frac{\mathrm{d}N}{\mathrm{d}\gamma_e} d\gamma_e \\ &\propto \int_{\gamma_{e,min}}^{\gamma_{e,max}} \gamma_e^2 \delta(\nu_{syn}(\gamma_e) - \nu)\gamma_e^{-2} d\gamma_e \\ &\propto \nu^{-\frac{1}{2}} \int \delta(x) dx \\ &\propto \nu^{-\frac{1}{2}} \ , \end{aligned} \tag{3-2-15}$$

where $x = \nu_{syn}(\gamma_e) - \nu$.

For $\gamma_{e,min} < \gamma_c < \gamma_e$, the steady-state continuity equation is reduced to

$$\frac{\mathrm{d}}{\mathrm{d}\gamma_e}\left(\dot{\gamma}_e \frac{\mathrm{d}N}{\mathrm{d}\gamma_e}\right) = A\gamma_e^{-p}$$

The solution to the above equation is given by

$$\frac{\mathrm{d}N}{\mathrm{d}\gamma_e} \propto \gamma_e^{-(p+1)} \ . \tag{3-2-16}$$

In this case, the synchrotron spectrum in the frequency range, $\nu_c < \nu$, is given by

$$\begin{aligned} F_\nu &\propto \int_{\gamma_{e,min}}^{\gamma_{e,max}} \gamma_e^2 \delta(\nu_{syn}(\gamma_e) - \nu)\gamma_e^{-(p+1)} d\gamma_e \\ &\propto \nu^{-\frac{p}{2}} \ . \end{aligned} \tag{3-2-17}$$

Finally, for $\gamma_{e,min} < \gamma_e < \gamma_c$, since the cooling is negligible for the electrons with γ_e, the energy spectrum of electrons is given by

$$\frac{\mathrm{d}N}{\mathrm{d}\gamma_e} \propto S(\gamma_e) \propto \gamma_e^{-p} \ . \tag{3-2-18}$$

Then, the synchrotron spectrum in the frequency range, $\nu_m < \nu < \nu_c$, is given by

$$\begin{aligned} F_\nu &\propto \int_{\gamma_{e,min}}^{\gamma_{e,max}} \gamma_e^2 \delta(\nu_{syn}(\gamma_e) - \nu)\gamma_e^{-(p+1)} d\gamma_e \\ &\propto \nu^{-\frac{p-1}{2}} \ . \end{aligned} \tag{3-2-19}$$

To summarize the above, observed synchrotron spectra have two cases: (i) $\nu_{\rm c} < \nu_{\rm m}$ and (ii) $\nu_{\rm c} > \nu_{\rm m}$. For $\nu_{\rm c} < \nu_{\rm m}$ (fast cooling regime), since all the electrons with $\gamma_{\rm c} < \gamma_{\rm e}$ cool down to $\gamma_{\rm c}$, the observed spectrum is given by

$$F_\nu = \begin{cases} (\frac{\nu}{\nu_{\rm c}})^{1/3} F_{\nu,{\rm max}} & (\nu_{\rm c} > \nu) \\ (\frac{\nu}{\nu_{\rm c}})^{-1/2} F_{\nu,{\rm max}} & (\nu_{\rm m} > \nu > \nu_{\rm c}) \\ (\frac{\nu_{\rm m}}{\nu_{\rm c}})^{-1/2} (\frac{\nu}{\nu_{\rm m}})^{-p/2} F_{\nu,{\rm max}} & (\nu > \nu_{\rm m}) \ . \end{cases} \tag{3-2-20}$$

where $F_{\nu,{\rm max}}$ is the peak flux.

For $\nu_{\rm m} < \nu_{\rm c}$ (slow cooling regime), the electrons with $\gamma_{\rm e} > \gamma_{\rm c}$ lose their energy, but the other electrons with $\gamma_{\rm e,min} < \gamma_{\rm e} < \gamma_{\rm c}$ do not cool. Then, the observed spectrum follows as

$$F_\nu = \begin{cases} (\frac{\nu}{\nu_{\rm m}})^{1/3} F_{\nu,{\rm max}} & (\nu_{\rm m} > \nu) \\ (\frac{\nu}{\nu_{\rm c}})^{-(p-1)/2} F_{\nu,{\rm max}} & (\nu_{\rm c} > \nu > \nu_{\rm m}) \\ (\frac{\nu_{\rm c}}{\nu_{\rm m}})^{-(p-1)1/2} (\frac{\nu}{\nu_{\rm c}})^{-p/2} F_{\nu,max} & (\nu > \nu_c). \end{cases} \tag{3-2-21}$$

The synchrotron spectra for the two cases are described as Figure 3.2.

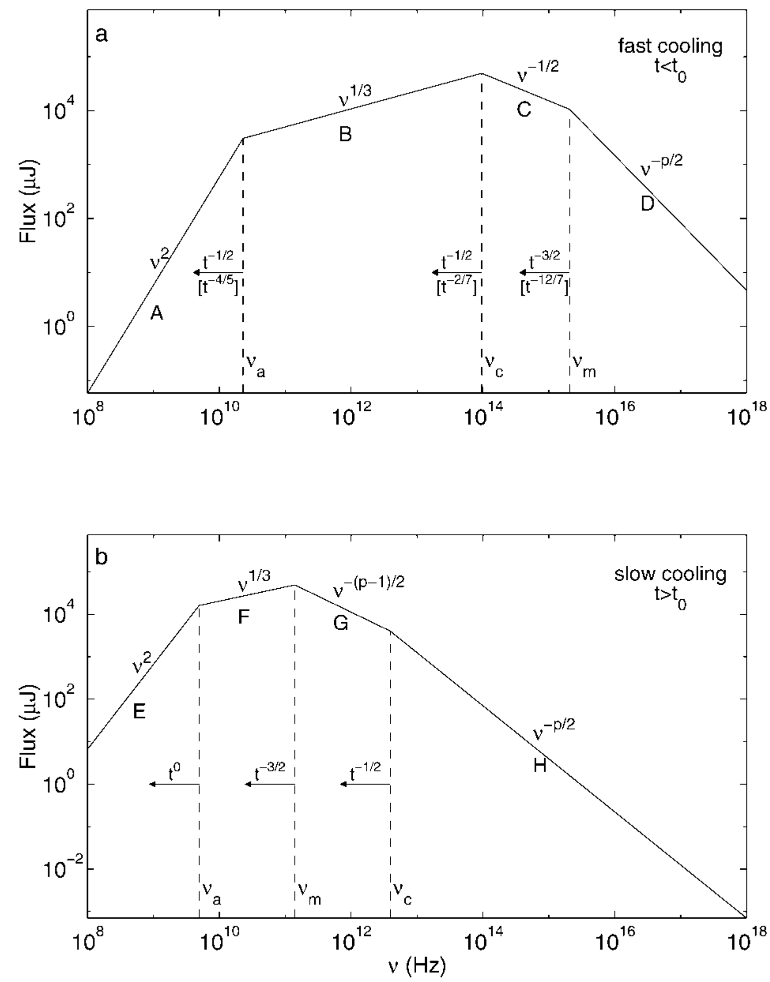

Figure 3.2: The synchrotron spectra for the case (a) $\nu_{\rm c} < \nu_{\rm m}$ (fast cooling) and (b) $\nu_{\rm c} < \nu_{\rm m}$ (slow cooling). $\nu_{\rm a}$ is synchrotron self-absorption frequency, where the emergent synchrotron flux is equal to the black-body flux. From Sari et al. (1998).

3.3 Light Curve of GRB Afterglows

The light curve of GRB afterglow can be derived by considering time evolutions of the peak flux and characteristic frequencies in the synchrotron spectrum (Sari et al., 1998). First of all, we consider a collision between an expanding shell with a rest mass M and a homogeneous external medium with a rest mass of $\mathrm{d}m$ in the observer frame. The conservation laws of the energy and momentum are given by

$$\begin{aligned} &\text{the energy conservation :} \\ &\Gamma M c^2 + \mathrm{d}m c^2 = (\Gamma + \mathrm{d}\Gamma)((M + \mathrm{d}m)c^2 + \mathrm{d}E') \qquad (3\text{-}3\text{-}22) \\ &\text{the momentum conservation :} \\ &\sqrt{\Gamma^2 - 1} M c = \sqrt{(\Gamma + \mathrm{d}\Gamma)^2 - 1}(M + \mathrm{d}m + \frac{\mathrm{d}E'}{c^2})c \ , \qquad (3\text{-}3\text{-}23) \end{aligned}$$

where $\Gamma + \mathrm{d}\Gamma$ and $\mathrm{d}m + \frac{\mathrm{d}E'}{c^2}$ are the Lorentz factor of the merged shell and the swept up external mass with the internal energy $\mathrm{d}E'$ measured in the merged shell rest frame, respectively. The two conservation laws are approximately reduced to

$$-M\mathrm{d}\Gamma = (\Gamma - 1)\mathrm{d}m + \Gamma\frac{\mathrm{d}E'}{c^2} \qquad (3\text{-}3\text{-}24)$$

$$-\frac{M\Gamma}{\Gamma^2 - 1}\mathrm{d}\Gamma = \mathrm{d}m + \frac{\mathrm{d}E'}{c^2} \ . \qquad (3\text{-}3\text{-}25)$$

From Eq.(3-3-24) and Eq.(3-3-25), we obtain

$$\mathrm{d}E' = (\Gamma - 1)\mathrm{d}m c^2 \ . \qquad (3\text{-}3\text{-}26)$$

Substituting Eq. (3-3-26) for Eq. (3-3-25), we find

$$\frac{\mathrm{d}\Gamma}{\Gamma^2 - 1} = -\frac{\mathrm{d}m}{M} \ . \qquad (3\text{-}3\text{-}27)$$

When the internal energy can lose a fraction ϵ of the internal energy due to radiation, the incremental total mass is written as,

$$\mathrm{d}M = \mathrm{d}m + (1 - \epsilon)\frac{\mathrm{d}E}{c^2} \ .$$

If the energy loss is negligible, that is, for the adiabatic case, the above equation is reduced to

$$\mathrm{d}M \approx \Gamma \mathrm{d}m \ . \qquad (3\text{-}3\text{-}28)$$

The initial energy of a cold shell is

$$E_0 = \Gamma_0 M_0 c^2 \ . \qquad (3\text{-}3\text{-}29)$$

where E_0, Γ_0, and M_0 are initial values of energy, Lorentz factor, and mass, respectively. Substituting Eq. (3-3-27) for Eq. (3-3-26), we find a relation of M and Γ:

$$\begin{aligned}
\frac{d\Gamma}{\Gamma^2 - 1} &= -\frac{dm}{\Gamma M} \\
\frac{1}{2}\frac{2\Gamma}{\Gamma^2 - 1}d\Gamma &= -\frac{dM}{M} \\
\ln|\Gamma^2 - 1|^{1/2} &= \ln M + \mathrm{A} \\
|\Gamma^2 - 1|^{1/2} &\propto M^{-1} \ , \\
\rightarrow \frac{M}{M_0} &= \left(\frac{\Gamma_0^2 - 1}{\Gamma^2 - 1}\right)^{\frac{1}{2}} \ .
\end{aligned} \tag{3-3-30}$$

From Eq. (3-3-28), the above equation becomes as follow:

$$\frac{m}{M_0} = \Gamma\left(\left(\frac{\Gamma_0^2 - 1}{\Gamma^2 - 1}\right)^{\frac{1}{2}} - \frac{\Gamma_0}{\Gamma}\right) \ . \tag{3-3-31}$$

For limit of $\Gamma_0 \gg \Gamma \gg 1$, Eq. (3-3-31) can be simplified as

$$m = \frac{M_0\Gamma_0}{2\Gamma^2} \ . \tag{3-3-32}$$

For a spherical expansion, the swept up mass is proportional to the inside volume of the expanding shell, $m \propto R^3 n m_{\rm p}$. Using this, Eq. (3-3-29) and Eq. (3-3-32), we can obtain the following relation (Blandford & McKee, 1976):

$$\begin{aligned}
E_0 &= \Gamma_0 M_0 c^2 \propto m\Gamma^2 c^2 \\
&= R^3\Gamma^2 n m_p c^2 \\
R^3\Gamma^2 &= const \ ,
\end{aligned} \tag{3-3-33}$$

Considering the relativistic beaming effect, we can write the observer time t as

$$\begin{aligned}
\mathrm{d}t &\approx \frac{\mathrm{d}R}{2\Gamma^2 c} \\
t &\sim \frac{R}{C_t\Gamma^2 c} \ ,
\end{aligned} \tag{3-3-34}$$

where C_t is a numerical factor which depends on details of the hydrodynamic evolution. We here use $C_t = 4$. Substituting the kinetic energy of a spherical shock : $E_0 \sim \Gamma^2 R^3 n m_{\rm p} c^2$ for Eq. (3-3-33), we obtain relations connecting R, Γ, and t for the adiabatic case.

$$R(t) \sim \left(\frac{E_0 t}{m_{\rm p} n c}\right)^{\frac{1}{4}} \tag{3-3-35}$$

$$\Gamma(t) \sim \left(\frac{E_0}{m_{\rm p} n c^5 t^3}\right)^{\frac{1}{8}} \ . \tag{3-3-36}$$

Using the above equations, the temporal evolution of the characteristic frequency, $\nu_{\rm c}$ and $\nu_{\rm m}$, and the peak flux, $F_{\nu,\max}$, are written as,

$$\begin{aligned}
\nu_c &\sim 10^{12}\epsilon_{\rm B}^{3/2}E_{0,52}^{-1/2}n_1^{'-1}t_{\rm d}^{-1/2}\ \ {\rm Hz} && (3\text{-}3\text{-}37)\\
\nu_m &\sim 10^{14}\epsilon_{\rm B}^{1/2}\epsilon_{\rm e}^{2}E_{0,52}^{1/2}t_{\rm d}^{-3/2}\ \ {\rm Hz} && (3\text{-}3\text{-}38)\\
F_{\nu,\max} &\sim 10^{5}\epsilon_{\rm B}^{1/2}E_{0,52}n_1^{'1/2}D_{28}^{-2}\ \ {\rm mJy}\ , && (3\text{-}3\text{-}39)
\end{aligned}$$

where $t_{\rm d}$ is the time in units of day, n_1 is the density in unit of cm^{-3}, $D_{28}=D/10^{28}$cm is the distance to the GRB source, and $E_{0,52}=E_0/10^{52}$erg. The temporal evolution of the characteristic frequencies are summarized in the left arrows described in Figure 3.2. At early time of a GRB afterglow, the synchrotron spectrum is the fast cooling regime ($\nu_{\rm c}<\nu_{\rm m}$), while at later time, the synchrotron spectrum becomes the slow cooling regime ($\nu_{\rm c}>\nu_{\rm m}$).

We define its transition time as t_0, which is written as,

$$t_0 = 10^2\epsilon_{\rm B}^2\epsilon_e^2E_{52}n_1^{'}\ \ {\rm days}\ . \qquad (3\text{-}3\text{-}40)$$

We here define the critical frequency, $\nu_0=\nu_{\rm c}(t_0)=\nu_{\rm m}(t_0)$, which is given by

$$\nu_0 \approx 10^{11}\epsilon_{\rm B}^{-5/2}\epsilon_{\rm e}^{-1}E_{52}^{-1}n_1^{'-3/2}{\rm Hz}. \qquad (3\text{-}3\text{-}41)$$

In addition, we define two times when an observed frequency, ν, becomes $\nu_{\rm c}$ and $\nu=\nu_{\rm m}$, as $t_{\rm c}$ and $t_{\rm m}$. From Eq. (3-3-37) and (3-3-38), the two time scales are given by

$$\begin{aligned}
t_{\rm c} &\sim 10^{-6}\nu_{15}^{-2}\epsilon_{\rm B}^{-3}E_{0,52}^{-1}n_1^{'-2}\ \ {\rm days} && (3\text{-}3\text{-}42)\\
t_{\rm m} &\sim 10^{-2/3}\nu_{15}^{-2/3}\epsilon_{\rm B}^{1/3}\epsilon_{\rm e}^{4/3}E_{0,52}^{1/3}\ \ {\rm days}, && (3\text{-}3\text{-}43)
\end{aligned}$$

where $\nu_{15}=\nu/10^{15}$Hz. If an observed frequency is higher than ν_0 ($\nu>\nu_0$), the order of three time scales becomes $t_c<t_{\rm m}<t_0$ and the synchrotron spectrum is the fast cooling regime. On the other hand, if an observed frequency is lower than ν_0 ($\nu<\nu_0$), the order of three time scales becomes $t_0<t_{\rm m}<t_{\rm c}$ and the synchrotron spectrum becomes the slow cooling regime. From Eqs. (3-2-20), (3-2-21), and Eqs. (3-3-37)-(3-3-39), light curves for the two regime are summarized as follows.

- For $\nu>\nu_0$ (fast cooling)

$$F_\nu = F_{\nu,\max}\times\begin{cases}\nu^{1/3}t^{1/6} & (\nu<\nu_{\rm c}<\nu_{\rm m})\\ \nu^{-1/2}t^{-1/4} & (\nu_{\rm c}<\nu<\nu_{\rm m})\\ \nu^{-p/2}t^{2-3p/4} & (\nu>\nu_{\rm m})\ .\end{cases} \qquad (3\text{-}3\text{-}44)$$

- For $\nu<\nu_0$ (slow cooling)

$$F_\nu = F_{\nu,\max}\times\begin{cases}\nu^{2}t^{1/2} & (\nu<\nu_{\rm m})\\ \nu^{(1-p)/2}t^{3(1-p)/4} & (\nu_{\rm m}<\nu<\nu_{\rm c})\\ \nu^{-p/2}t^{2-3p/4} & (\nu_{\rm c}<\nu)\ .\end{cases} \qquad (3\text{-}3\text{-}45)$$

Figure 3.3 shows the above light curves.

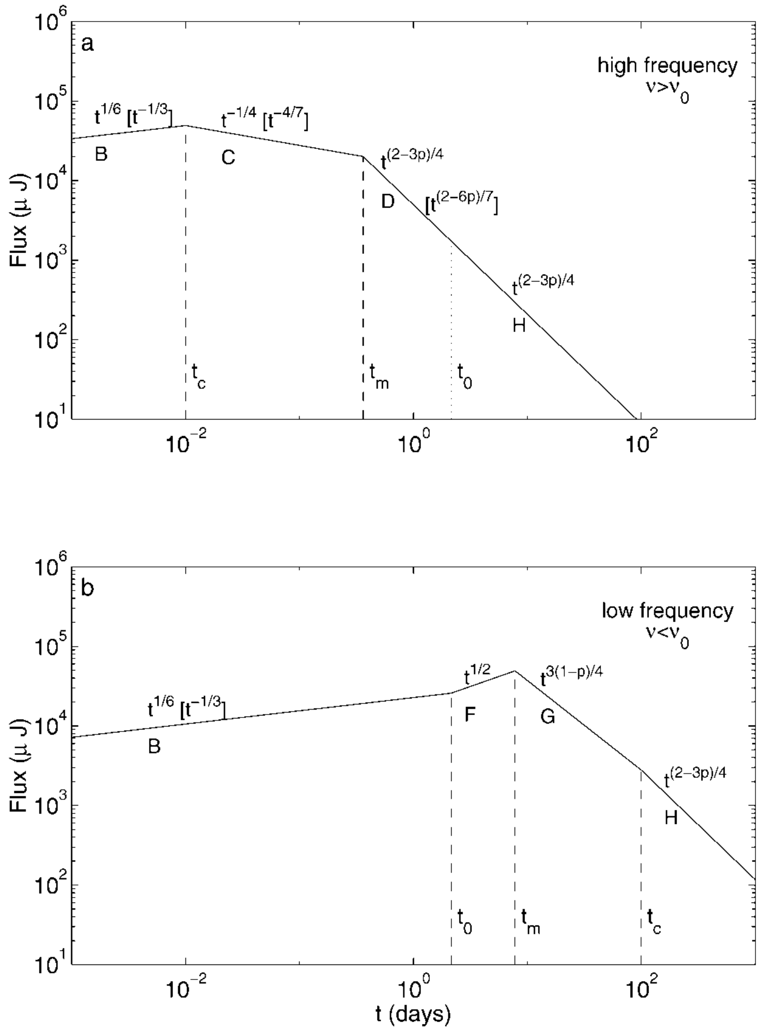

Figure 3.3: Light curves of GRB afterglows. From Sari et al. (1998)

.

Chapter 4

Problem about Magnetic Field in GRB Afterglows

4.1 Introduction

In spite of a large number of GRB events and associated studies, a lot of problems have not been solved in the radiation mechanism of GRB afterglows. The origin of GRB is also still an open problem. In this thesis, we focus on problems about the shock dissipation because physics of the shock dissipation is always important to understand high-energy astrophysical objects and origin of cosmic rays. In the standard model of GRB afterglows, ϵ_{e}, ϵ_{B}, and p are parameters on the shock dissipation. These parameters have been investigated by plasma particle simulations and estimated from observations of GRB afterglows. In this chapter, we especially review early studies for ϵ_{B} which describes the magnetic field strength in the shock downstream region.

The energy dissipation in relativistic shocks is important in studies of the production of nonthermal particles (cosmic rays) and radiation from high-energy astrophysical transients. Such phenomena occur in dilute environments, so that the relativistic shocks dissipate the bulk flow through kinetic processes in a collisionless plasma. Here, the collisionless plasma means that a momentum exchange by the Coulomb collision between two bodies can be negligible. The Weibel instability, which occurs in the collisonless plasma with a temperature anisotropy (Weibel, 1959), has been actively investigated in this field. The Weibel instability generates magnetic fields and would be important in the particle acceleration in the relativistic collisionless shock (Medvedev & Loeb, 1999; Spitkovsky, 2008b; Sironi et al., 2013; Matsumoto et al., 2017). The Weibel instability also works for the dissipation of non-relativistic collisionless shocks and especially plays a crucial role in an electron acceleration (Kato & Takabe, 2010; Matsumoto et al., 2015). Recently, a formation of the Weibel mediated shock has been also studied using high-power lasers (Fox et al., 2013; Huntington et al., 2015; Ross et al., 2017).

However, the recent particle-in-cell (PIC) simulations have shown that the magnetic field generated by the Weibel instability cannot persist for the radiation time of the observed afterglows. In addition, the coherent length of the Weibel generated field is much smaller than the gyroradii of high-energy particles. This means that the radiation mechanism is not synchrotron radiation but jitter radiation (Medvedev, 2000), and the efficiency of particle acceleration becomes inefficient. Thus, the understanding of the mechanism of magnetic field amplification is important for understanding the radiation mechanism of the GRB afterglows and particle acceleration. Observational and theoretical studies regarding the magnetic field in the GRB afterglows are summarized below.

4.2 Linear analysis for collisionless plasma instabilities in an unmagnetized plasma

In this section, we perform linear analysis for collisionless plasma instabilities in an unmagnetized plasma. We here consider only nonrelativistic particles for simplicity because the relativistic effect is not important to understand the essence of the Weibel instability.

Although there is a finite magnetic field in the interstellar and circumstellar media, effects of the background magnetic field can be negligible as long as we consider a plasma dynamics in a short timescale compared with the gyro period and in a smaller scale than the gyroradius.

The linearized Maxwell's equations are given as follows:

$$\begin{aligned} \vec{\nabla} \times \delta\vec{B} &= \frac{4\pi}{c}\delta\vec{j} + \frac{1}{c}\frac{\partial \delta\vec{E}}{\partial t} \quad , \\ \vec{\nabla} \times \delta\vec{E} &= -\frac{1}{c}\frac{\partial \delta\vec{B}}{\partial t} \quad . \end{aligned}$$

Any perturbations are described as a superposition of plane waves as long as we consider a uniform background system. Performing the Fourier expansion in $\delta\vec{B}, \delta\vec{E}$ and $\delta\vec{j}$, the linearized Maxwell's equations are

$$i\vec{k} \times \delta\vec{B}_k = \frac{4\pi}{c}\delta\vec{j}_k - i\frac{\omega}{c}\delta\vec{E}_k \quad , \tag{4-2-1}$$

$$i\vec{k} \times \delta\vec{E}_k = i\frac{\omega}{c}\delta\vec{B}_k \quad . \tag{4-2-2}$$

Since the current can be replaced by the electric field $\delta\vec{E}$ using the Ohm's law: $\delta\vec{j} = \overleftrightarrow{\sigma}\delta\vec{E}$, where $\overleftrightarrow{\sigma}$ is the electric conductivity tensor, Eq. (4-2-1) becomes

$$\begin{aligned} -\frac{c}{\omega}\vec{k} \times \delta\vec{B}_k &= \left(\frac{4\pi i\overleftrightarrow{\sigma}}{\omega} + 1\right)\delta\vec{E}_k \\ &= \left(\overleftrightarrow{I} + \frac{4\pi i\overleftrightarrow{\sigma}}{\omega}\right)\delta\vec{E}_k \equiv \overleftrightarrow{\epsilon}\delta\vec{E}_k \quad , \end{aligned} \tag{4-2-3}$$

where $\overleftrightarrow{\epsilon}(\vec{k},\omega) \equiv \overleftrightarrow{I} + 4\pi i\overleftrightarrow{\sigma}/\omega$ is the permittivity tensor. Using Eq. (4-2-2), we can express Eq. (4-2-3) without the magnetic field $\delta\vec{B}_k$ as follows:

$$\begin{aligned} -\frac{c}{\omega}\vec{k} \times \frac{c}{\omega}\vec{k} \times \delta\vec{E}_k &= \overleftrightarrow{\epsilon}\delta\vec{E}_k \\ \overleftrightarrow{\epsilon}\delta\vec{E}_k + \left(\frac{c}{\omega}\right)^2 \vec{k} \times (\vec{k} \times \delta\vec{E}_k) &= 0 \\ \left[\overleftrightarrow{\epsilon} - \left(\frac{c}{\omega}\right)^2 (\overleftrightarrow{I} - \frac{\vec{k}\otimes\vec{k}}{k^2})\right]\delta\vec{E}_k &= 0 \quad . \end{aligned} \tag{4-2-4}$$

Replacing the term inside the bracket by a tensor $\overleftrightarrow{D}(\vec{k},\omega)$, the linearized Maxwell's equations can be reduced to a simple equation,

$$\overleftrightarrow{D}(\vec{k},\omega)\cdot\delta\vec{E}_k = 0 \quad . \tag{4-2-5}$$

In order for this equation to have a non-trivial solution, the determination of the tensor $\overleftrightarrow{D}$ must be 0. This condition gives a dispersion relation for electromagnetic waves in a homogeneous plasma:

$$\begin{aligned} \det\overleftrightarrow{D}(\vec{k},\omega) &= 0 \\ \det\left[\overleftrightarrow{\epsilon} - \left(\frac{c}{\omega}\right)^2 (\overleftrightarrow{I} - \frac{\vec{k}\otimes\vec{k}}{k^2})\right] &= 0 \quad . \end{aligned} \tag{4-2-6}$$

The perturbed current $\delta\vec{j}_k$ included in the permittivity tensor $\overleftrightarrow{\epsilon}$ is given by

$$\delta\vec{j}_k = \sum_s q_s \int \vec{v}\delta f_{s,k}(\vec{v}) d^3\vec{v} \quad , \tag{4-2-7}$$

where $\delta f_{s,k}$ is the perturbed distribution function of particle, s, and $\vec{v}$ is the velocity of particles. Then, $\overleftrightarrow{\epsilon}\delta\vec{E}_k$ is expressed as follows:

$$\overleftrightarrow{\epsilon}(\vec{k},\omega)\delta\vec{E}_k = \delta\vec{E}_k + \frac{4\pi i}{\omega}\sum_s q_s \int \vec{v}\delta f_s(\vec{v}) d^3\vec{v} \quad . \tag{4-2-8}$$

To obtain $\overleftrightarrow{\epsilon}(\vec{k},\omega)$, we have to represent the second term in the right hand side of the Eq. (4-2-8) as a function of electric field $\delta\vec{E}_k$.

The collisionless Boltzmann equation is

$$\frac{\partial f_s}{\partial t} + \vec{v}\cdot\vec{\bigtriangledown}_x f_s + \frac{q_s}{m_s}\left(\vec{E} + \frac{\vec{v}}{c}\times\vec{B}\right)\cdot\vec{\bigtriangledown}_v f_s = 0 \quad , \tag{4-2-9}$$

where m_s and q_s are the particle mass and the particle charge, respectively. The distribution function is $f_s = f_{s0} + \delta f_s$, so that the linearized collisionless Boltzmann equation is

$$\frac{\partial \delta f_s}{\partial t} + \vec{v}\cdot\vec{\bigtriangledown}_x \delta f_s + \frac{q_s}{m_s}\left(\delta\vec{E} + \frac{\vec{v}}{c}\times\delta\vec{B}\right)\cdot\vec{\bigtriangledown}_v f_{s0} = 0 \quad . \tag{4-2-10}$$

The first and second term in the left hand side of Eq. (4-2-10) represents the total differential of δf_s. In addition, the perturbations of electromagnetic fields can be expressed as follows:

$$\begin{aligned} \delta\vec{E}(\vec{x},t) &= \int_{-\infty}^{\infty}\int_{-\infty}^{\infty} \delta\vec{E}_k \exp(i(\vec{k}\cdot\vec{x} - \omega t)) d^3k d\omega \\ \delta\vec{B}(\vec{x},t) &= \int_{-\infty}^{\infty}\int_{-\infty}^{\infty} \delta\vec{B}_k \exp(i(\vec{k}\cdot\vec{x} - \omega t)) d^3k d\omega \ , \end{aligned}$$

so that Eq. (4-2-10) becomes

$$\frac{d\delta f_s}{dt} = -\int_{-\infty}^{\infty}\int_{-\infty}^{\infty} \frac{q_s}{m_s}\left(\delta\vec{E}_k + \frac{\vec{v}}{c}\times\delta\vec{B}_k\right)\cdot\vec{\nabla}_v f_{s0} e^{i(\vec{k}\cdot\vec{x}-\omega t)} d^3k d\omega \tag{4-2-11}$$

$$= -\int_{-\infty}^{\infty}\int_{-\infty}^{\infty} \frac{q_s}{m_s}\left\{\left(1-\frac{\vec{k}\cdot\vec{v}}{\omega}\right)\overleftrightarrow{I} + \frac{\vec{k}\otimes\vec{v}}{\omega}\right\}\delta\vec{E}_k\cdot\vec{\nabla}_v f_{s0} e^{i(\vec{k}\cdot\vec{x}-\omega t)} d^3k d\omega \ , \tag{4-2-12}$$

where we used Eq. (4-2-2) in order to remove the magnetic field $\delta\vec{B}_k$ from Eq. (4-2-11). Performing the Fourier expansion and integrating Eq. (4-2-12) with regard to a time over the interval $[-\infty : t]$, we obtain the Fourier component of the perturbed distribution function, δf_k:

$$\delta f_k = \frac{q_s}{m_s\omega i}\left\{\delta\vec{E}_k\cdot\vec{\nabla}_v f_{s0} - \vec{k}\cdot(\vec{\nabla}_v f_{s0})\vec{v}\cdot\delta\vec{E}_k\frac{1}{\vec{k}\cdot\vec{v}-\omega}\right\} \ . \tag{4-2-13}$$

Eq. (4-2-13) suggests that the particles with the velocity $\vec{v} = (\omega/k)\hat{k}$ significantly contribute to the perturbed current, $\delta\vec{j}$. From Eq. (4-2-13), the perturbed current density becomes

$$\delta\vec{j}_k = -\sum_s \frac{q_s^2}{m_s\omega_i}\left\{n_{s0}\delta\vec{E}_k + \int\vec{k}\cdot(\vec{\nabla}_v f_{s0})\frac{\vec{v}\otimes\vec{v}\cdot\delta\vec{E}_k}{\vec{k}\cdot\vec{v}-\omega}d^3\vec{v}\right\} \ , \tag{4-2-14}$$

where n_{s0} is the number density of the particle species s. Therefore, from Eq. (4-2-8), (4-2-14), and the total plasma frequency $\omega_{\rm p} = \sum_s 4\pi q_s^2 n_{s0}/m_s$, the permittivity tensor $\overleftrightarrow{\epsilon}$ is given by

$$\overleftrightarrow{\epsilon}(\vec{k},\omega) = \left(1-\frac{\omega_{\rm p}^2}{\omega^2}\right)\overleftrightarrow{I} + \sum_s\frac{4\pi q_s^2}{m_s\omega^2}\int(\vec{k}\cdot\vec{\nabla}_v f_{s0})\frac{\vec{v}\otimes\vec{v}}{\omega-\vec{k}\cdot\vec{v}}d^3\vec{v} \ . \tag{4-2-15}$$

Substitute Eq. (4-2-15) for Eq. (4-2-6), we can obtain the dispersion relation for electromagnetic waves.

4.3 The Weibel Instability

In Figure 4.1, the physical mechanism of the Weibel instability is described. There are two counter-streaming electron plasmas with drift velocities $\boldsymbol{v} = \pm v_e\hat{x}$ in a magnetic field perturbation $\delta\boldsymbol{B} = \delta B_z \cos ky\hat{z}$ which is generated by thermal fluctuations. The directions of streaming plasma are deflected by the Lorentz force, $-e(\boldsymbol{v}/c)\times\delta\boldsymbol{B}$, as shown by the dashed lines in Figure 4.1. As a result, the electrons moving to the $+(-)x$-direction concentrate in the region I (II), and currents are generated in the regions I and II. Then, magnetic fields in the $\pm z$-direction is produced around the currents. The direction of the produced magnetic field is the same as that of the initial perturbed magnetic field. Therefore, the two counter-streaming plasmas are unstable and generates a magnetic field. In the next two subsections, we derive the dispersion relation and growth rate of the Weibel instability for two cases, two counter-streaming plasmas and anisotropic temperature plasmas.

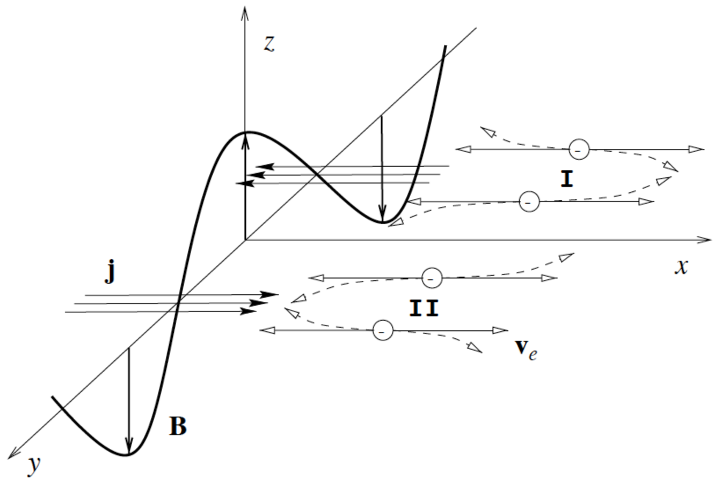

Figure 4.1: Physical picture of the Weibel instability . From Medvedev & Loeb (1999)

.

4.3.1 Two Counter-streaming plasmas

We here set the wave vector $\vec{k}$ of the perturbed electromagnetic field along the y-axis. The initial distribution function of each species f_{s0} is the Maxwell distribution with the drift velocity $v_{\rm d}$ of the x-direction,

$$f_{\rm s0} = \frac{n_{\rm s0}}{\pi^{3/2} v_{{\rm th},s}^3} \exp\left[-\frac{(v_x - v_{\rm d})^2 + v_y^2 + v_z^2}{v_{{\rm th},s}^2} \right] \quad , \tag{4-3-16}$$

where $v_{{\rm th},s}$ is the thermal velocity. Then, the dispersion relation for the electromagnetic waves is given by,

$$1 - \left(\frac{ck}{\omega}\right)^2 - \sum_s \frac{\omega_{{\rm p},s}}{\omega} + \sum_s \frac{\omega_{{\rm p},s}}{\omega} \left[\left(\frac{v_{\rm d}}{v_{{\rm th},s}} \right)^2 + \frac{1}{2} \right] (1 + \xi_s Z(\xi_s)) = 0 \quad , \tag{4-3-17}$$

where $\omega_{{\rm p},s}$ is the plasma frequencies for each species, $\xi_s = \omega / k v_{{\rm th},s}$, and $Z(\xi_s)$ is the plasma dispersion function:

$$Z(\xi_s) \equiv \frac{1}{\sqrt{\pi}} \int_{-\infty}^{\infty} \frac{e^{-z^2}}{z - \xi_s} dz \quad .$$

The dispersion function is approximately expressed as follows:

$$Z(\xi_s) \simeq \begin{cases} i\sqrt{\pi} e^{-\xi_e^2} - 2\xi_s \left(1 - \frac{2}{3}\xi_s^2 + \cdots\right) & \text{for } |\xi_s| \ll 1 \\ i\sqrt{\pi} e^{-\xi_s^2} - \frac{1}{\xi_s}\left(1 + \frac{1}{2}\xi_e^{-2} + \cdots\right) & \text{for } |\xi_s| \gg 1 \quad . \end{cases}$$

When the counter-streaming flows are cold ($\xi_{\rm e} \gg 1$) electron-positron plasma, the dispersion relation becomes

$$1 - \left(\frac{ck}{\omega}\right)^2 - 4\left(\frac{\omega_{\rm p}}{\omega}\right)^2 - 2\left(\frac{\omega_{\rm p}}{\omega}\right)^2 \left(\frac{k v_{\rm d}}{\omega}\right)^2 = 0 \; . \tag{4-3-18}$$

Solving Eq. (4-3-18) with regard to ω, we obtain the growth rate γ of the Weibel instability excited in the two counter-streaming plasmas. For a short wavelength limit, the growth rate is given by

$$\gamma = \left(\frac{v_\mathrm{d}}{c}\right)\omega_\mathrm{p} \quad \text{at } k \gg \frac{\omega_\mathrm{p}}{c} \quad . \tag{4-3-19}$$

For $k < \omega_\mathrm{p}/c$, the growth rate decreases as the wavelength becomes longer. Therefore, the characteristic wavelength of the Weibel instability is the plasma skin depth, c/ω_p.

4.3.2 Anisotropic temperature plasmas

Next, we derive the dispersion relation and the maximum growth rate of the Weibel instability excited in an anisotropic temperature plasma as $T_x > T_y$. The initial distribution function is given by,

$$f_{s0} = \frac{n_{s0}}{\pi^{3/2} v_{\mathrm{th},x}^2 v_{\mathrm{th},y}^2} \exp\left[-\left(\frac{v_x}{v_{\mathrm{th},x}}\right)^2 - \frac{v_y^2 + v_z^2}{v_{\mathrm{th},y}^2}\right] \quad .$$

The temperature in the z-direction is the same as the y-direction. We set the wave vector along the x-axis. Then, the dispersion relation becomes

$$1 - \left(\frac{ck}{\omega}\right)^2 \frac{\omega_\mathrm{p}^2}{\omega^2} + \sum_s \left(\frac{\omega_{\mathrm{p},s}}{\omega}\right)^2 (A+1)\{1 + \xi_s Z(\xi_s)\} = 0 \quad , \tag{4-3-20}$$

where A is the temperature anisotropy:

$$A \equiv \left(\frac{v_{\mathrm{th},y}}{v_{\mathrm{th},x}}\right)^2 - 1 \quad . \tag{4-3-21}$$

For hot electron plasmas ($\xi_s \ll 1$, $A \ll 1$), Eq. (4-3-20) becomes

$$\omega^2 + \omega_\mathrm{p}^2 \frac{(A+1)}{k v_{\mathrm{th},x}} i\sqrt{\pi} - c^2k^2 + \omega_\mathrm{p}^2 A = 0 \ . \tag{4-3-22}$$

Solving Eq. (4-3-22) for ω, we obtain the linear growth rate of the Weibel instability driven by the temperature anisotropy,

$$\gamma_k = \frac{1}{\sqrt{\pi}} \frac{kc}{A+1} \left(A - \frac{k^2c^2}{\omega_\mathrm{p}^2}\right) \quad . \tag{4-3-23}$$

Because the electromagnetic wave grows for $\gamma_k \geq 0$, the unstable region in the wavenumber space is from 0 to k_max where

$$k_\mathrm{max}^2 = \frac{\omega_\mathrm{p}^2}{c^2} A \quad .$$

The maximum growth rate is given by

$$\gamma_\mathrm{max} = \left(\frac{4}{27\pi}\right)^{1/2} \frac{v_\mathrm{th}}{c} \frac{A^{3/2}}{A+1} \omega_\mathrm{p} \quad \text{at } k = \frac{1}{\sqrt{3}} k_\mathrm{max} \tag{4-3-24}$$

(Davidson et al., 1972). The characteristic wave length of the Weibel instability is about the plasma skin depth, c/ω_p. In addition, the wave length that has the maximum growth rate becomes longer as the temperature anisotropy becomes small.

4.4 Observational Studies for Magnetic Field in GRB Afterglows

In the standard model, the afterglow emission of GRB is thought to be the synchrotron emission from energetic electrons in post-shock regions (Sari et al., 1998). Various studies based on the standard model of the afterglow suggest that the fraction of the magnetic-field energy density converted from kinetic energy density, $\epsilon_{\rm B}$, widely ranges from $\sim 10^{-8}$ to $\sim 10^{-2}$ with the mean of about 10^{-5}, with an assumption that the density of 1 $\rm cm^{-3}$ (Santana et al., 2014, see Figure 4.2). The lower limit is still larger than the shock-compressed value of interstellar magnetic field ($\sim 10^{-9}$), so that the field amplification is necessary. Moreover, since afterglows continue to be bright over a period of days to years, the field should remain strong in flowing downstream (Gruzinov & Waxman, 1999; Piran, 2004; Katz et al., 2007). In principle, the value of $\epsilon_{\rm B}$ may be constrained from the observed ratio of the peaks in the photon energy spectrum of the synchrotron and inverse Compton emissions. However, it still has large uncertainty because of the small number of events detected in GeV-TeV energy bands. Therefore, it is important to theoretically estimate the value of $\epsilon_{\rm B}$ through the microprocesses at the shock for understanding of the radiation mechanism of the GRB afterglows.

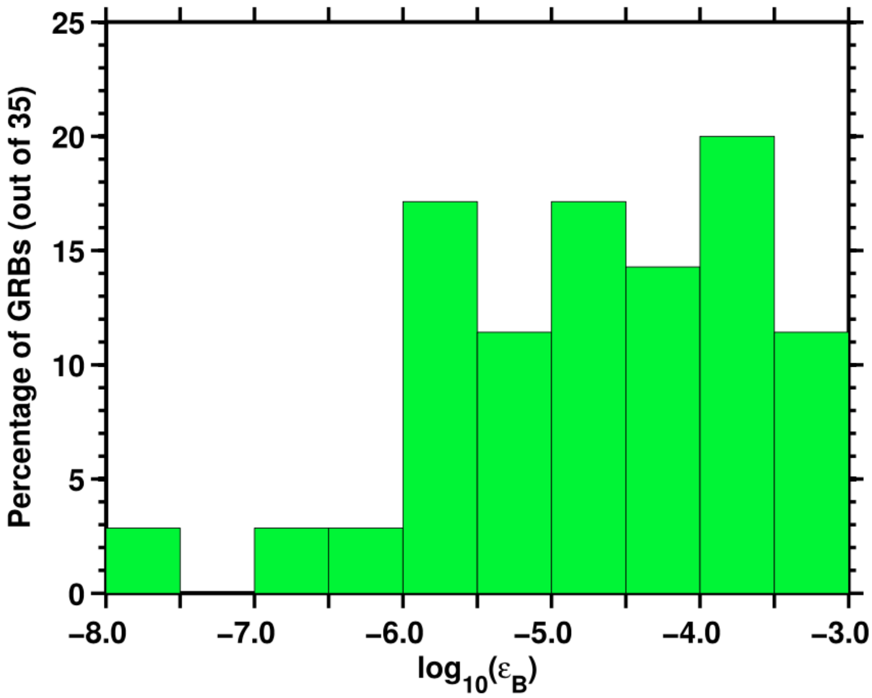

Figure 4.2: Distribution of $\epsilon_{\rm B}$ determined from optical afterglow data. The authors assumed that $\epsilon_{\rm e} = 0.2$, $n = 1\ {\rm cm}^{-3}$, and kinetic energy of the bulk flow is 4 times the energy in prompt gamma-ray emission. From Santana et al. (2014).

Since the long-term evolution of the magnetic field generated by the Weibel instability in three-dimensional shock structures has not been investigated yet, it is currently unknown whether the Weibel generated field can survive long enough to explain the GRB afterglow emission. If we extrapolate the scaling, $\epsilon_{\rm B} \approx (t\omega_{\rm pe})^{-1}$, the post-shock magnetic field in the Weibel-mediated shocks propagating into homogeneous media is too small to explain the GRB afterglow emission lasting for $t\omega_{\rm pp} \sim 10^7$. If a large scale magnetic field is generated, the decay of the magnetic field becomes slower. In addition, the coherent length scale of the magnetic field generated by the Weibel instability around the shock transition region is about $10\ c/\omega_{\rm pp}$ which is smaller than the gyroradius of nonthermal particles. Then, the radiation from the nonthermal electrons is not the synchrotron radiation, but the jitter radiation (Medvedev, 2000). However, the standard model of the GRB afterglow which assumes the synchrotron radiation can explain many observed features of the GRB afterglow. Therefore, a large scale magnetic field amplification is desired.

The observed large dispersion of $\epsilon_{\rm B}$ appears to be a key ingredient in understanding the origin of the amplified magnetic field. Santana et al. (2014) shows the distribution of the amplification factor which characterizes how much the seed magnetic field was amplified beyond the shock compression (Figure 4.3). The amplification factor is given by,

$$\begin{aligned} \mathrm{AF} &= \left(\frac{\epsilon_{\rm B}}{\epsilon_{\rm B,sc}}\right)^{1/2} \\ &\propto n^{0.2} B_0^{-1} \ , \end{aligned} \tag{4-4-25}$$

where $\epsilon_{\rm B,sc}$ is the ratio of the energy density of the magnetic field compressed by the shock to the kinetic energy density. The amplification factor has a weak dependence of the upstream density compared with magnetic fields. As seen in Figure 4.3 where the seed magnetic field is assumed to be 10μG, the amplification factor ranges from 1 to ~ 1000. If the distribution of the upstream magnetic field spans from 10 μG to 10 mG, the downstream magnetic field could be explained by the shock compression of the upstream magnetic field. On the other hand, if the magnetic field strength and the plasma temperature in the upstream region are similar to those in the Galactic ISM, then both Alfvén and sonic Mach numbers are much larger than unity at early afterglows, where we assume the Lorentz factor of the flow of $10 - 100$. Then, the downstream shock structure does not depend on these quantities, that is, they are not important parameters in calculating the GRB afterglow emission (Sari et al., 1998). In that case, since the dispersion of $\epsilon_{\rm B}$ is not determined by the upstream density alone, there should be another piece controlling the downstream state.

4.5 Simulation Studies for Magnetic Field in GRB Afterglows

So far, the nonlinear evolution of the magnetic field generated by the Weibel instability has been investigated for shocks propagating into homogeneous plasmas (Silva et al., 2003; Kato, 2005; Chang et al., 2008; Keshet et al., 2009; Medvedev et al., 2011; Lemoine, 2015; Takamoto et al., 2018; Ruyer & Fiuza, 2018). Very recently, a comprehensive theoretical model of Weibel-mediated relativistic pair shocks was provided (Lemoine et al., 2019a; Pelletier et al., 2019; Lemoine et al., 2019b,c). In this section, we review the evolution of

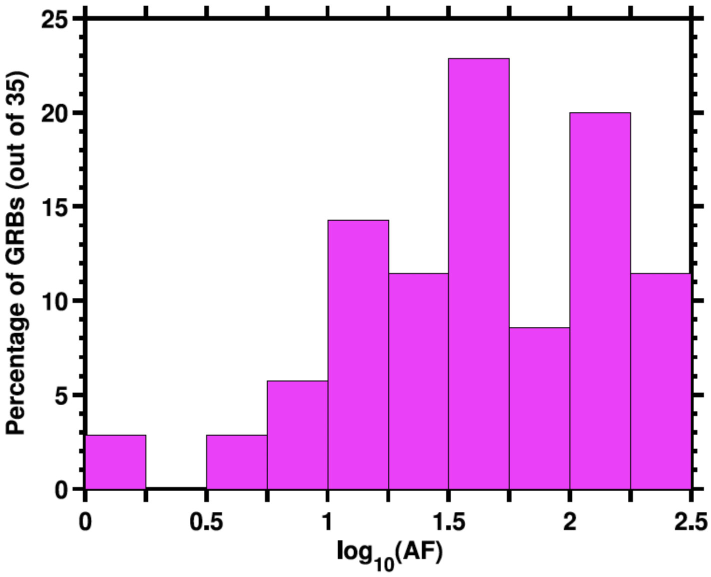

Figure 4.3: Distribution of the magnetic field amplification factor for the optical afterglow samples same as Figure 4.2, where $n = 1\ \mathrm{cm}^{-3}$ and $B_0 = 10\mu\mathrm{G}$ were assumed. From Santana et al. (2014)

the magnetic field generated by the Weibel instability in a relativistic collisionless shock propagating into a homogeneous medium.

Figure 4.4 shows the time evolution of the post-shock magnetic field, where two-dimensional structures of the magnetic energy density, $B^2/4\pi\Gamma n_0 c^2$, at different times separated by $450\omega_{\mathrm{pe}}^{-1}$ are displayed in the panels (a)-(d). The black, red, green, and blue curves in the panel (e) show spatial profiles of the magnetic energy density averaged over the y-direction for each panel (a)-(d). The time evolution of magnetic clumps around the yellow vertical line shows that the magnetic field with a smaller scale rapidly decays, while the magnetic field with a larger scale decays more slowly. According to the two-dimensional electron-positron plasma shock simulation in Chang et al. (2008), the decay rate is given by $\epsilon_{\mathrm{B}} \approx (t\omega_{\mathrm{pe}})^{-1}$, where ω_{pe} is the plasma frequency of electrons measured in the downstream rest frame. This means that the magnetic field generated by the Weibel instability in the shock transition region cannot persist during the GRB afterglow emission lasting for $t\omega_{\mathrm{pp}} \sim 10^7$ in the downstream rest frame, where ω_{pp} is the plasma frequency of protons measured in the downstream rest frame (Sironi & Goodman, 2007).

In the long-term simulation ($t\omega_{\mathrm{pe}} \sim 10^4$) performed by Keshet et al. (2009), the field is moderate in decaying because the length scale of the magnetic field becomes large thanks to the high-energy particles accelerated at the shock (Figure 4.5). The decay rate depends on the time evolution of the spectrum of the magnetic field fluctuation (Chang et al., 2008; Lemoine, 2015). Chang et al. (2008) gave the analytic form of the decay rate as, $\epsilon_{\mathrm{B}} \propto (t\omega_{\mathrm{pe}})^{-2(p+1)/3}$, where p is the index of the magnetic field fluctuation with a large wavelength, assuming that: the scattering time t_{s} of particles is larger than the coherence time t_{c}, $t_{\mathrm{s}}/\tau_{\mathrm{c}} > 1$, and relativistic plasma with isotropic momentum space. Their simulation shows $p \simeq 1/2$ at late time ($t\omega_{\rm pe} \sim 10^3$), so that the magnetic field decays as $\epsilon_{\rm B} \approx (t\omega_{\rm pe})^{-1}$. Chang et al. (2008) consider that the total magnetic power is determined by long-wavelength components because the small-scale component decays steeper than the large-scale component, from $|\delta B_k|^2 = -k^3c^3/\omega_{\rm pe}^2$. As shown in Figure 4.6, the small-scale components shown in their simulation result are maintained for longer time than that in their analytical result. This is because the simulation result includes the nonlinear effect of magnetic trapping. According to Lemoine (2015), when the spectral index $\alpha_{\rm B}$ of the magnetic power spectrum is below -1, one can derive from $t_{\rm s}/\tau_{\rm c} \propto k^{-\alpha_{\rm B}-1}$ that the magnetic trapping of particles becomes prominent for the dissipation of small-scale magnetic fluctuation. If we assume that the afterglow is due to the synchrotron radiation in decaying magnetic field, the broadband spectrum ranging from optical to GeV requires the temporal decay index of the magnetic field, $\epsilon_{\rm B} \propto (t\omega_{\rm pe})^{0.5}$ (Lemoine, 2013). In that case, the analytical prediction of the spectral index of the magnetic field fluctuation is $\alpha_{\rm B} = -1.5$, that is, a prominent nonlinear effect on the magnetic dissipation is suggested. Magnetic trapping of particles can lead to MHD-like behaviors and modify the decay rate of the magnetic field. It is important to understand the nonlinear evolution of the magnetic field for the case of $\tau_{\rm c}/t_{\rm c} < 1$. Because the present calculation cannot investigate such a regime, other theoretical tools are needed (Lemoine, 2015). Therefore, the long-term evolution of magnetic fields generated by the Weibel instability has not been theoretically understood yet.

Previous local PIC simulations with periodic boundary conditions have shown that the current filaments more easily merge in the three-dimensional case than in the two-dimensional case. Thanks to the merging of current filaments, the length scale of the magnetic field becomes longer and the decay rate decreases (Silva et al., 2003; Takamoto et al., 2018). Medvedev et al. (2011) suggested that the decay index is -2 in electron-positron plasmas, although the simulation time ($t\omega_{\rm pe} \simeq 50$) is much shorter than the timescale of GRB afterglows. Recent two- and three-dimensional simulations with a larger simulation box in the flow direction have shown that the current filament is destructed by the drift-kink instability before being large scale (Ruyer & Fiuza, 2018; Vanthieghem et al., 2018, see Figure 4.7). The authors claimed that magnetic fields generated by the Weibel instability rapidly decay in a realistic three dimensional system. These simulations were, however, performed with the periodic boundary condition along the flow direction, which is different from the non-periodic shock structure, and no effect of particle acceleration was considered.

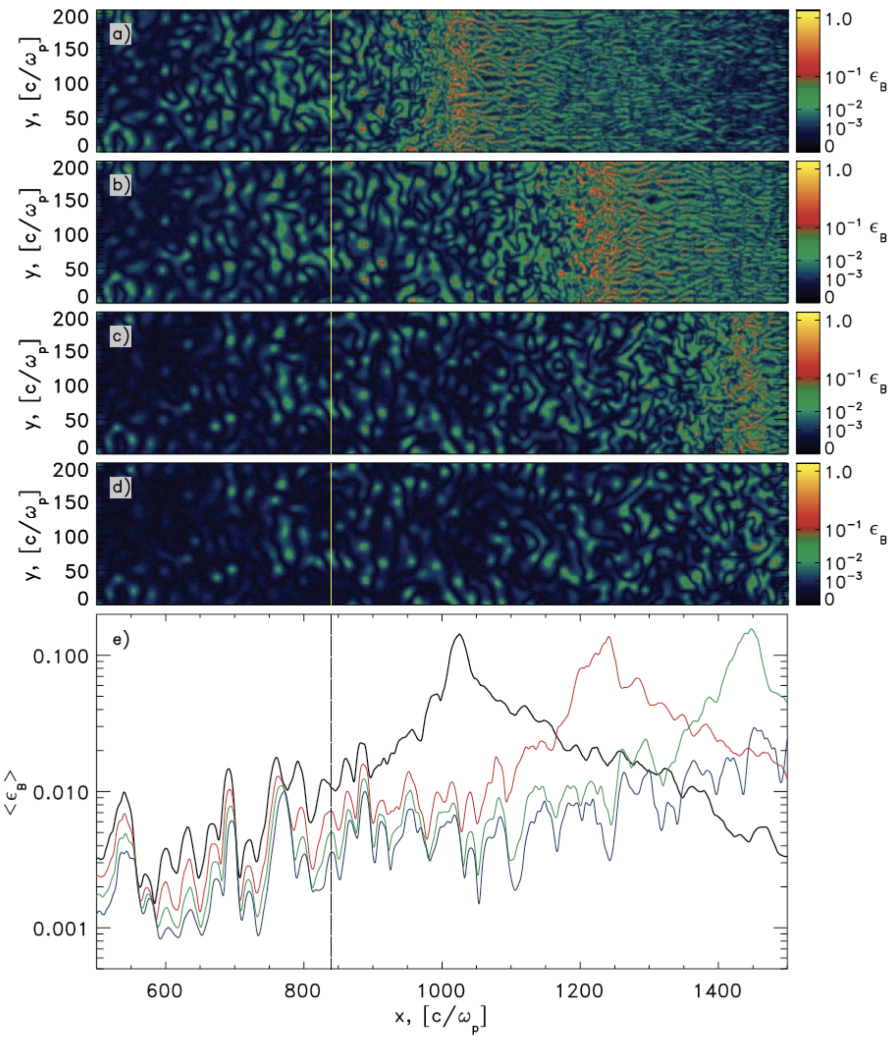

Figure 4.4: Panel (a) – (d):Two-dimensional structures of the magnetic energy density, $B^2/4\pi\Gamma nc^2$, at different times separated by $450\omega_{\rm pe}^{-1}$. Each of the curves in the panel (e) shows the spatial profile of the magnetic energy density averaged over the y-direction for each of the top panels: (a) black, (b) red, (c)green, and (d) blue. From Chang et al. (2008).

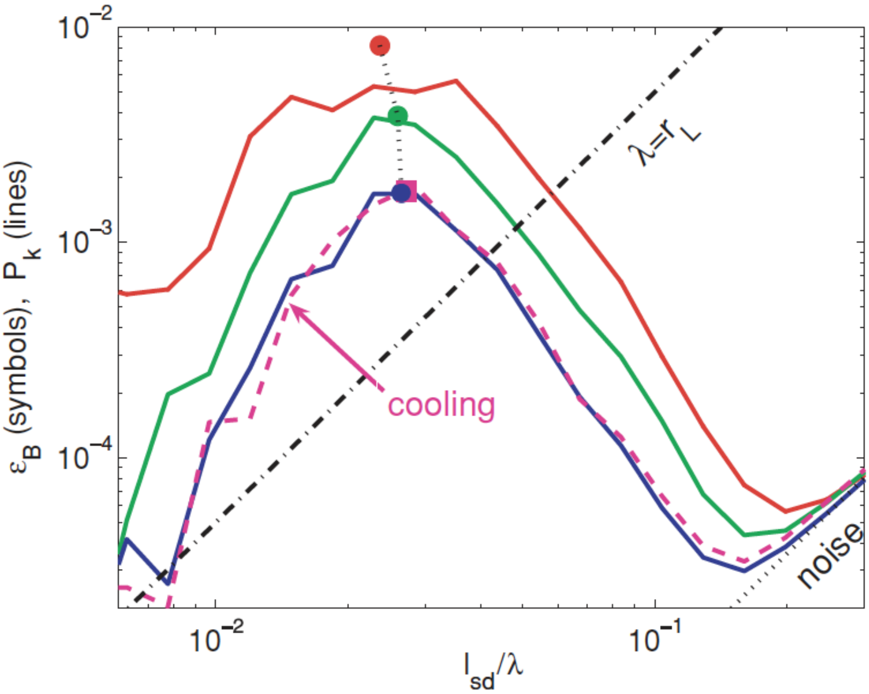

Figure 4.5: Power spectra of the magnetic field in a part of the downstream region of shock propagating into a homogeneous plasma at $t\omega_{\rm pe}$ =1900 (blue curve), 4600 (green curve), and 12600 (red curve). The wavenumber λ^{-1} of the magnetic field is normalized by the skin depth, $l_{\rm sd}$. The integrated energy fraction $\epsilon_{\rm B}$ (filled circles) increases with time and the growth of magnetic coherent length. The dashed line and the square show the power spectrum and $\epsilon_{\rm B}$ at $t\omega_{\rm pe} = 5750$ for the case introducing an artificial cooling of particles (i.e. the energy gain of all particles with the Lorentz factor above 80 are artificially suppressed). It is found that the particle acceleration has significant effects on the evolution of downstream magnetic field. From Keshet et al. (2009).

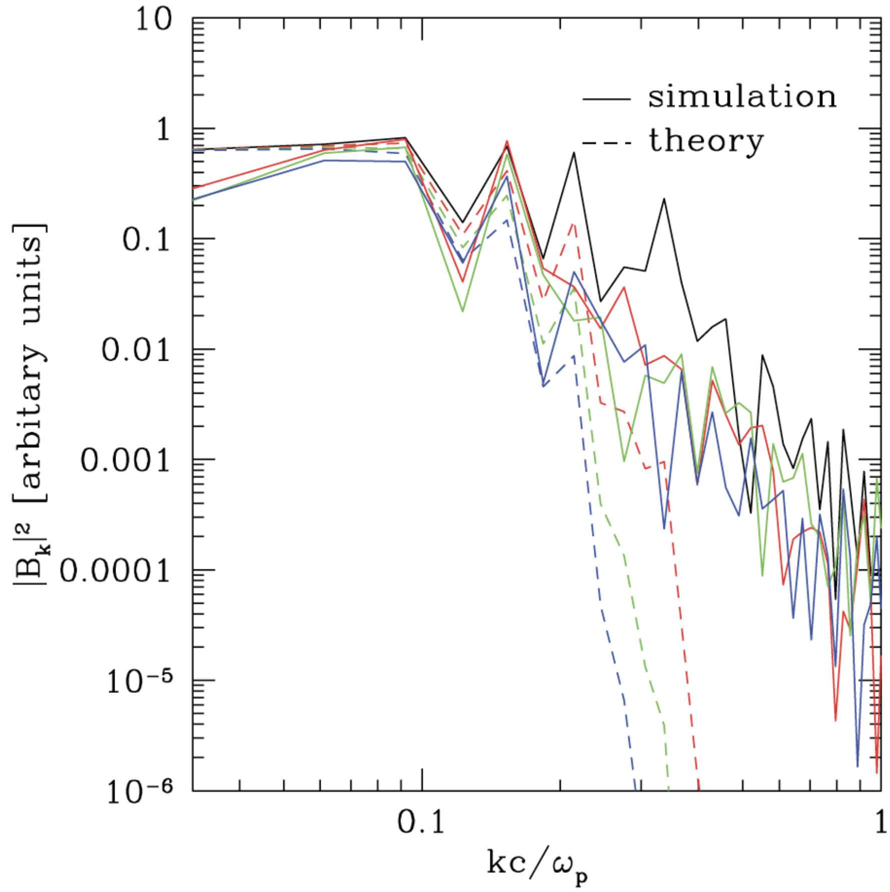

Figure 4.6: Spectral evolution of magnetic field at the 840 $c/\omega_{\rm pe}$ in Figure 4.4. The black line shows the magnetic power spectrum at early time. The blue, green, and red lines shows the magnetic power spectrum at $t\omega_{\rm pe} = 1900, 4600, 12600$, based on simulation data. The dashed curves represent analytic evolution of the magnetic power spectrum. From Chang et al. (2008).

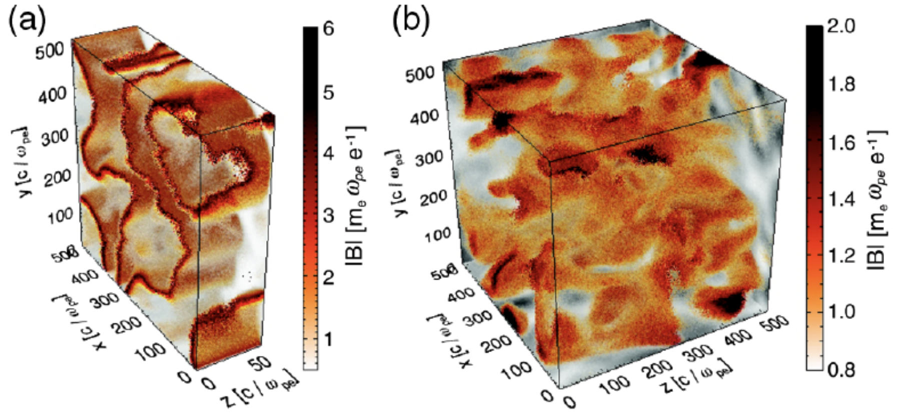

Figure 4.7: The spatial structures of the magnetic field in the interaction of initially unmagnetized counter-streaming plasmas with drift velocity of 0.7 c and mass ratio $m_\mathrm{p}/m_\mathrm{e} = 128$, at $t\omega_\mathrm{pp} = 400$ in three-dimensional simulations. The panel (b) shows that if the simulation box is sufficiently large, the current structures are destructed and the growth of the length scale of the magnetic field is saturated. From Ruyer & Fiuza (2018).

Chapter 5

Relativistic Shocks Propagating into Inhomogeneous Media

5.1 Introduction

Since the interstellar medium (ISM) has a density fluctuation, the upstream medium of shock waves that emit GRB afterglows is generally inhomogeneous. The characteristic length scale of the ISM fluctuations is on the order of 100 pc for the ISM turbulence (Armstrong et al., 1995). In addition, progenitors of long GRBs are thought to be massive stars. The environment around them, circumstellar matter (CSM), has a density fluctuation produced by the stellar wind. The length scale of the CSM turbulence is smaller than one of ISM (Chugai & Danziger, 1994; Ramirez-Ruiz et al., 2005; Smith et al., 2009; Yalinewich & Portegies Zwart, 2019). Ramirez-Ruiz et al. (2005) showed that the CSM becomes inhomogeneous owing to some instabilities (see Figure 5.1). Yalinewich & Portegies Zwart (2019) investigated the evolution of the CSM in a binary system and showed that the density around the massive star is modulated by the orbital motion (see Figure 5.1). Some observations of radio supernovae suggest that the CSM is actually inhomogenous (Wang & Loeb, 2000; Lazzati et al., 2002; Dai & Lu, 2002; Heyl & Perna, 2003; Schaefer et al., 2003; Nakar et al., 2003).

Then, the large dispersion of $\epsilon_{\rm B}$ may come from the inhomogeneity of the surrounding environment, that is, the wavelength of the upstream fluctuation potentially becomes an important parameter in describing the downstream magnetic field. In fluid scale, the field amplification process depends on the environment around a progenitor star. Magnetohydrodynamics (MHD) simulations have shown that the magnetic field is amplified by turbulent dynamo when the shock is propagating into the inhomogeneous media (Sironi & Goodman, 2007; Inoue et al., 2011; Mizuno et al., 2011). The interaction between a shock front and a high density clump distorts the shock front. The disturbed shock front drives a rotational fluid motion (vorticity) in the downstream region, which amplify the magnetic field by stretching magnetic field lines. In this case, the decay timescale of the amplified magnetic field is given by about the eddy turn over time. Inoue et al. (2011) have performed a three-dimensional MHD simulation of a relativistic shock propagating into an inhomogeneous medium. As seen in Figure 5.3, the magnetic field amplified by the dwonstream turbulence depends on the amplitude of the upstream density fluctuation.

When the turbulent kinetic energy is dissipated, particle diffusion or kinetic plasma

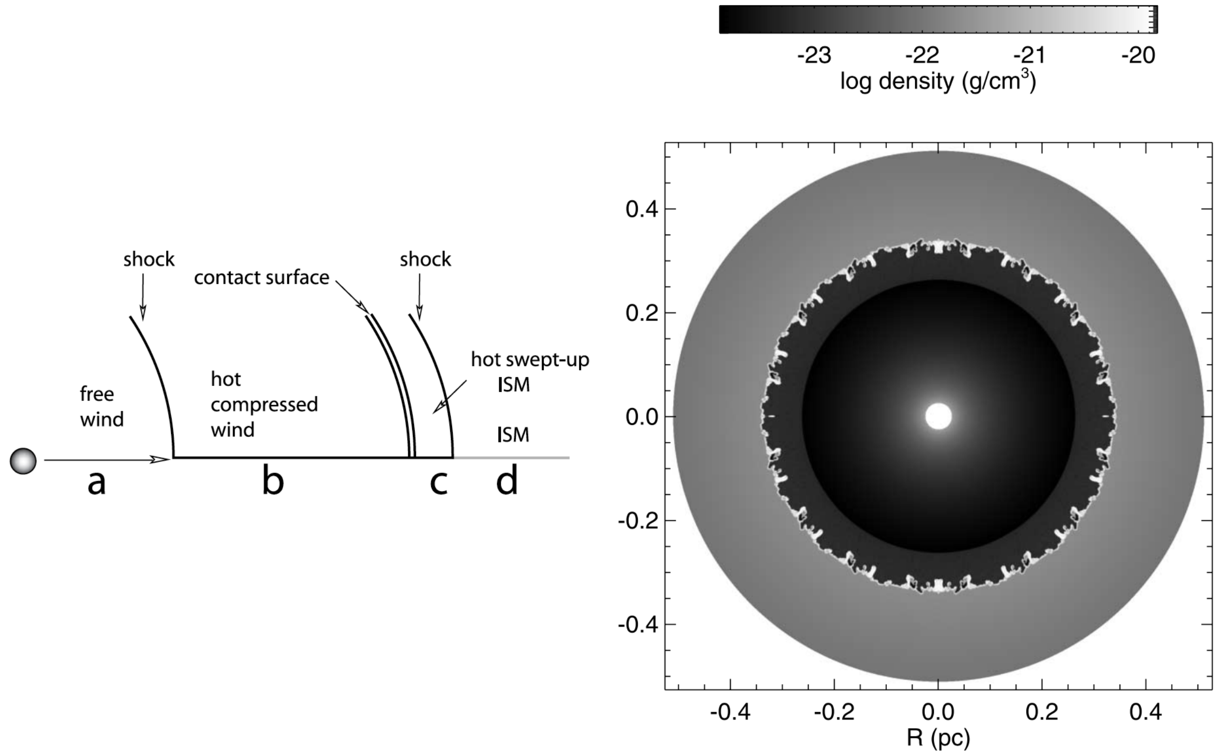

Figure 5.1: A four-zone structure around a GRB progenitor (left panel), where the density discontinuity and two shocks are formed by the wind - ISM interaction. The right panel shows the structure of a CSM gas density around a 29 $M_{\odot}$ massive star after 8000 yr of evolution since the onset of the Wolf-Rayet star in the hydrodynamic simulation of the wind - ISM interaction around a massive star. From Ramirez-Ruiz et al. (2005) .

instabilities are excited in a collisionless plasma. In addition, the diffusive motion of high-energy particles may potentially impact on the shock structure. With fluid approximation, a linear analysis of an interaction between a shock and an incident entropy wave shows that entropy and subsonic modes are excited by the mode conversion in front of and behind the shock (McKenzie & Westphal, 1968; Lemoine et al., 2016). Shu & Osher (1989) and Arshed & Hoffmann (2013) studied a shock tube problem in the case of the interaction between the shock and some waves. They claimed that an upstream incident entropy wave is compressed at the shock front, being advected stably in the downstream region. However, it is not clear whether the incident waves passing through the shock front can persist in kinetic scale when the particle diffusion is nonnegligible. In this case, the density fluctuations may rapidly decay before the magnetic field is amplified by the turbulence in large scale. Moreover, the energy dissipation by the particle diffusion is expected to lead to the plasma heating and particle acceleration. The kinetic plasma instability may convert the turbulent kinetic energy to the magnetic energy. In this thesis, using a first principles approach, we investigate possible effects of the upstream density fluctuation on the evolution of downstream magnetic field.

In Section 5.2[1], two-dimensional local PIC simulations are performed to see the nonlinear

[1]A version of Section 5.2 was first published in *The Astrophysical Journal* (Tomita & Ohira, 2016)

evolution of the Weibel instability in electron-positron plasma with an anisotropic density structure, which mimics the downstream region of a relativistic shock propagating into an inhomogeneous medium. We show that particles escape from an anisotropic high-density region, leading a temperature anisotropy large enough for the Weibel instability to make the magnetic field fluctuation.

In Section 5.3[2], we conduct two-dimensional PIC simulations of relativistic shocks propagating into the inhomogeneous medium for the first time. Our simulation shows that the Weibel magnetic field has a larger scale and higher magnitude than that for the case of the homogeneous density distribution. Such magnetic fields can persist in the far downstream region without significant decay. We also confirm there are entropy and sound waves in the downstream region during the simulation time. The temperature anisotropy is generated by the diffusion of high-energy particles, being maintained in the far downstream region. The magnetic field amplification by the Weibel instability is however, less significant in the downstream region.

[2]A version of Section 5.3 was first published in *The Astrophysical Journal* (Tomita et al., 2019)

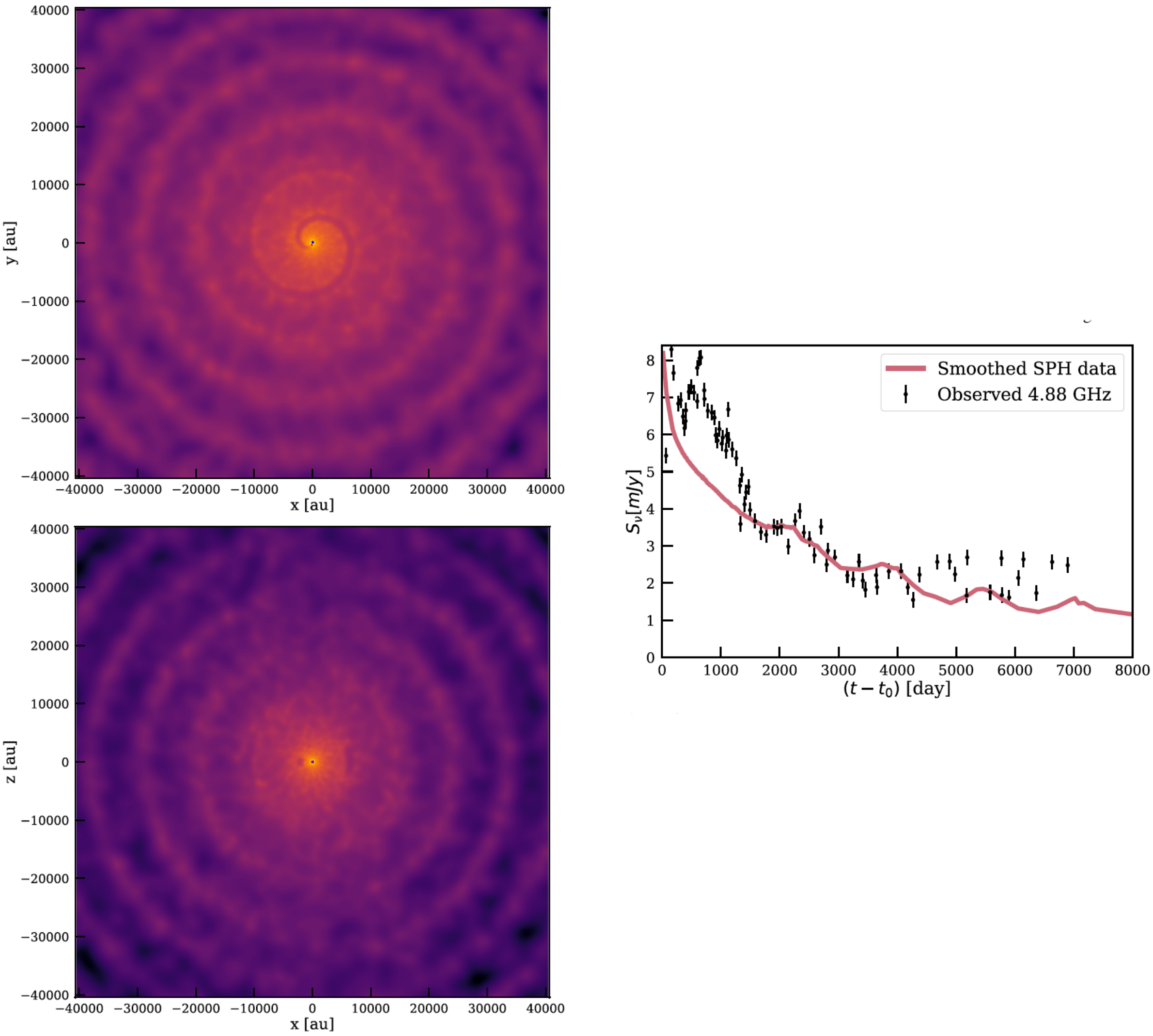

Figure 5.2: Left panel: Inhomogeneous gas-density distribution in $x - y$ plane (top) and $x - z$ plane (bottom) in the three-dimensional numerical simulation of the wind evolution of the binary system. The primary is located at the center of the image (blue bullet) and the red bullets represent the companion. Right panel: Radio light curve inferred from the simulation (red line) and the observed light curve for SN 1979C. From Yalinewich & Portegies Zwart (2019).

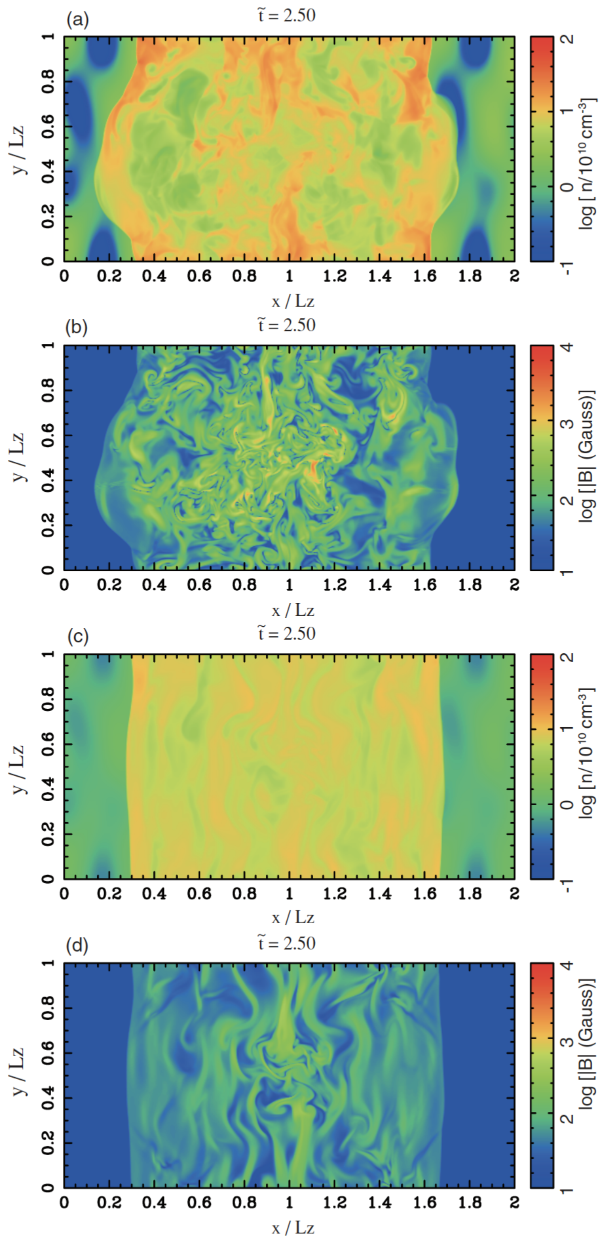

Figure 5.3: The result of a three-dimensional MHD simulation of a shock propagating into an inhomogeneous medium. The shock propagates to $\pm x$-direction. The background magnetic field B_0 is set in the y-direction. The upper two panels show the spatial structure of the density (a) and the strength of the magnetic field (b) for the case of $B_0 = 7.5$ G and the initial density perturbation $\Delta n/n_0 = 0.9$. The bottom two panels show the spatial structure of the density (c) and the strength of the magnetic field (d) for the case of $B_0 = 7.5$ G and the initial density perturbation $\Delta n/n_0 = 0.3$. All panels shows the structure at $z = 0.0$ in $x - y$ plane. From Inoue et al. (2011).

5.2 The Weibel Instability Excited in Anisotropic Density Structures

5.2.1 Downstream-Weibel Model

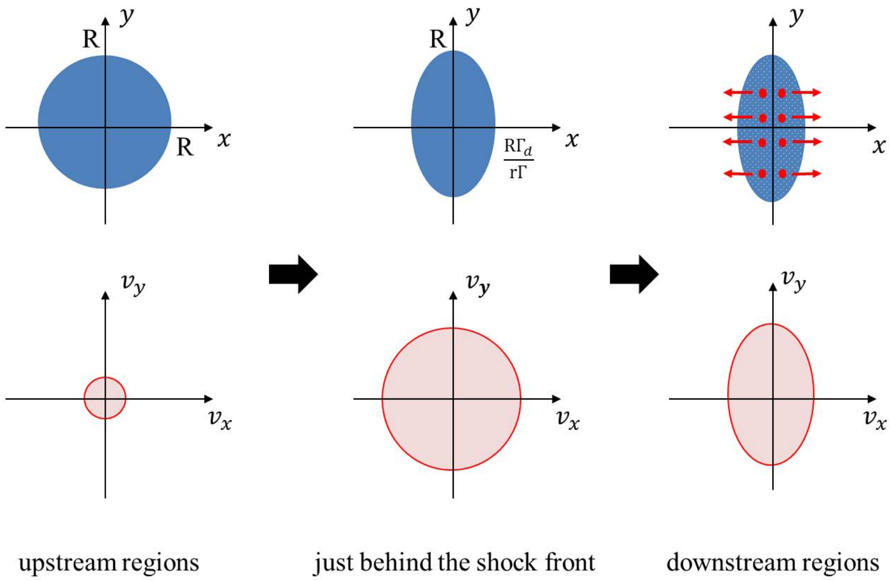

Figure 5.4: Generation mechanism of the temperature anisotropy in the post shock region. The upper and lower panels show the structure of a high-density region and the velocity distribution in the high-density region, respectively. The left, middle, and right columns show the shock upstream region, the region just behind the shock, and the downstream region, respectively. Each cartoon is illustrated in the local fluid rest frame. From Tomita & Ohira (2016).

In addition to the magnetic field amplification due to the Weibel instability and turbulent dynamo near the shock front, we propose a new model of the magnetic field generation in the shock downstream region. We consider an interaction between a shock wave and an isotropic cold density clump in the collisionless system, where the density clump corresponds to entropy or sound modes. We focus on only the evolution of an entropy wave in this model. Figure 5.4 shows the cartoons illustrating the structure of the density clump and velocity distribution in the density clump. Each cartoon is illustrated in the local fluid rest frame. The upstream density clump is isotropic and cold in the upstream rest frame. After the shock passes through the density clump, the density clump is compressed in the shock-normal direction (x-direction). The length scale of the downstream clump in the x-direction is compressed by $\Gamma_{\mathrm{d}}/(r\Gamma)$, where r and Γ_{d} are the shock compression ratio and the Lorentz factor of the downstream flow at the shock rest frame. For unmagnetized plasma, the magnetic field produced by the Weibel instability dissipates the bulk flow of plasma in the shock transition region, and makes the velocity dispersion large in the downstream region. Then, high-energy particles escape from the anisotropic high-density clump in the shock-normal direction with the sound velocity (right panel in Figure 5.4). On the other hand, it takes longer time to escape in the shock-tangential direction, so that temperature anisotropy ($T_x < T_y$) is generated in the high-density clump as shown in the right panel in Figure 5.4. Since in the low-density region the number of particles with high velocity v_x are increased, the temperature in the shock-normal direction, T_x, becomes higher than the shock-tangential direction, T_y. As a result, the Weibel instability is excited and generates the magnetic field in the downstream high- and low- density regions. Therefore, the upstream inhomogeneity can also cause a magnetic field generation by the Weibel instability in the downstream region.

In order for this model to explain the observation of afterglow emissions of GRBs, the generation timescale of the temperature anisotropy t_{ta} should be comparable to the timescale of the afterglow emission t_{dec}. This time t_{dec} corresponds to the deceleration time of blast waves, so that it is written as,

$$t_{\mathrm{dec}}\omega_{\mathrm{pp}} = 7.4 \times 10^7 E_{\mathrm{iso}}^{1/3} n_0^{1/6} \Gamma_2^{-5/3} \quad , \tag{5-2-1}$$

where ω_{pp} is the plasma frequency of protons, $E_{\mathrm{iso}} = 10^{53} E_{\mathrm{iso},53}$ erg is the isotropic equivalent energy of the GRB, $n = 10^0 n_0$ cm^{-3} is the upstream number density in the upstream rest frame, and $\Gamma_2 = 10^2\Gamma$ is the Lorentz factor of the blast wave. The generation time scale of the temperature anisotropy t_{ta} is determined by the sound crossing time,

$$t_{\mathrm{ta}} = \frac{R\Gamma_{\mathrm{d}}}{\Gamma r v_{\mathrm{th}}} \quad , \tag{5-2-2}$$

where v_{th} and R are the thermal velocity in the downstream region and the length scale of the high density clump in the upstream region. Then, from Eq. (5-2-2), the length scale of density clump should be

$$R \approx 4.8 \times 10^{17} \mathrm{cm} \left(\frac{r/\Gamma_{\mathrm{d}}}{2\sqrt{2}} \right) \frac{v_{\mathrm{th}}}{c} E_{\mathrm{iso},53}^{1/3} n_0^{-1/3} \Gamma_2^{-2/3}, \tag{5-2-3}$$

where $r/\Gamma_{\mathrm{d}} = 2/\sqrt{2}$ for ultra-relativistic shock limit. This corresponds to the characteristic length scale of density fluctuation in ISM, although the characteristic length scale in the environment around GRB progenitors, of course, is uncertain. We can expect that in any length scale of density fluctuation, our model could contribute to the magnetic field amplification for the afterglow emissions in GRBs.

5.2.2 Simulation of the Weibel Instability in Anisotropic Density Structures

In order to confirm whether our model actually works or not, we first perform two-dimensional periodic PIC simulations for the Weibel instability in anisotropic density structures.

Setting

In our study, we use the two-dimensional electromagnetic PIC code (pCANS). We use the first order shape factor (the cloud in cell method). We set a two-dimensional periodic box in the $x - y$ plane, and track three component of velocity, magnetic fields, and electric fields. Preparing two counter-streaming unmagnetized electron-positron plasmas which are unstable velocity distribution for the Weibel instability, we first excite the Weibel instability in this simulation. The streaming direction is the y-direction and the drift and thermal velocities of electron-positron plasma are $v_{\rm d} = \pm 0.5c$ and $v_{\rm th} = 0.1c$, respectively. For an early afterglow phase, the shock is relativistic (e.g. $\Gamma = 100$), and eventually becomes nonrelativistic at a later phase. In PIC simulations, a cold relativistic plasma flow unphysically generate electromagnetic field fluctuations and unphyiscally heats plasma, which is called the numerical Cherenkov instability (Godfrey, 1974). We adapted a mildly relativistic velocity in order to avoid the numerical Cherenkov instability. Whether the plasma is relativistic or non-relativistic is not essential for the generation of temperature anisotropy because the anisotropic escape of particles is caused by anisotropic density structures. In GRB afterglows, the shock upstream plasma is an electron-proton plasma. However, we use an electron-positron plasma because it is easy to perform a large simulation. Previous PIC simulations showed that the downstream ion and electron energies are almost equipartition for relativistic shocks (Spitkovsky, 2008a; Kumar et al., 2015). In this case, the effective masses of electrons and protons, γm, become the same. Therefore, the electron-positron plasma is applicable for GRB afterglows at the early phase.

We set the anisotropic density structures in the simulation box as,

$$n(x, y) = n_0\{1 + 0.5 \sin(2\pi x/L_x)\}, \tag{5-2-4}$$

where L_x and n_0 are the wavelength and the mean number density, respectively. There is one wavelength in the simulation box, and the density fluctuation depends only on the x-coordinate. The amplitude of the density fluctuation, $\delta n/n_0$ is 0.5, and the length scale of the high density region is $L_x/2$. We use 40 electrons and 40 positrons per cell in this study. We investigated a dependence of a numerical heating on the number of particles, by performing simulations for 10, 20, 40 particles per cell per species. We confirmed that the more particles, the more suppressed are the numerical heating. The result displayed below is for 40 particles per cell per species. To investigate a wavelength dependence in the magnetic field generation, we perform three runs for the wavelength of $L_x = 120, 240, 480c/\omega_{\rm pe}$. The skindepth, $c/\omega_{\rm pe}$, is defined by the mean number density of electron-positron plasmas, n_0, and 10 cells is used per a skindepth to solve Maxwell equations. The time step is $\Delta t = 0.05\omega_{\rm pe}^{-1}$.

Results

We compare the nonlinear evolution of the Weibel instability for a case of a homogeneous density distribution and an anisotropic one. Figure 5.6 shows the time evolution of the mean magnetic energy density normalized by the mean initial kinetic energy density,

$$\epsilon_{\rm B} = \frac{B^2/8\pi}{(\Gamma - 1)n_0 m_{\rm e} c^2} \ . \tag{5-2-5}$$

The exponential growth of the magnetic field at $t\omega_{\rm pe} \approx 10$ is the linear phase of the Weibel instability driven in the initial condition of counter-streaming plasmas. After the saturation, for the homogeneous density distribution (black), the magnetic field simply decays, which is

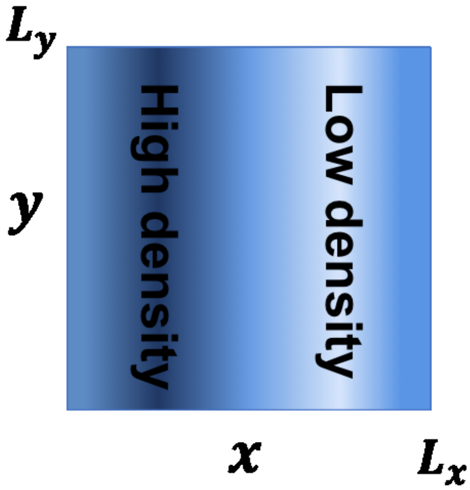

Figure 5.5: Schematic diagram of the setup of the two-dimensional periodic PIC simulations for the Weibel instability in anisotropic density structures. The density structure is spatially anisotropic. The streaming direction is the y-direction. The periodic boundary condition is imposed in the x and y-directions.

consistent with results of previous studies for the nonlinear evolution of the Weibel instability in a homogeneous plasma.

On the other hand, for the case of the anisotropic density structures with wavelength $L_x = 120$ (green line), 240 (red line), and 480 $c/\omega_{\rm pe}$ (blue line), there are second peaks at $t \approx 100,\ 200,\ 300\ \omega_{\rm pe}^{-1}$ after the first saturation. As the wavelength becomes longer, the second growth of the magnetic field starts more slowly. Each timescale of these second growth of the magnetic field is comparable to the sound-crossing time in the high-density region, $L_x/2v_{\rm th}$. We will explain the origin of the second growth of the magnetic field using the simulation result for the anisotropic density structure with the wavelength of $L_x \sim 240c/\omega_{\rm pe}$. In order to prove whether the the second growth results from the Weibel instability, in the Figure 5.7, we show the time evolution of the temperature anisotropy, $A = T_y/T_x - 1$, in the high- (red line) and low- (blue line) density regions. As explained in Section 5.2.1, the plasmas is heated almost isotropically by the first Weibel instability at $t \approx 10\ \omega_{\rm pe}^{-1}$, so that the temperature anisotropy decreases and closes to 0 after the first saturation. For the homogeneous case (black line), the temperature anisotropy decreases with time monotonically, while for the anisotropic density structures it increases up to $A \sim 0.25$ (-0.2) in the high- (low-) density region at $t \sim 10^2\ \omega_{\rm pe}^{-1}$. This implies that particles moving x-direction escape from the high-density region to the low-density region, so that the temperature in the x-direction decreases (increases) in the high- (low-) density region. The timescales of the generation of the temperature anisotropy is comparable to the sound-crossing time in the high- and low- density region, $L_x/2v_{\rm th}$. Thus, we found that the temperature anisotropy is generated by the particle escape. After $t \sim 10^2\omega_{\rm pe}$, the temperature anisotropy oscillates with time while the amplitude decreases because the anisotropic density structure decays due to the heating by the magnetic field.

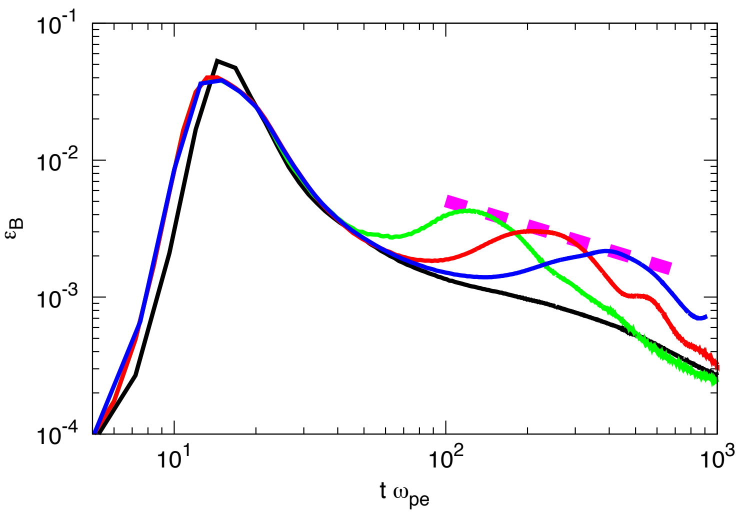

Figure 5.6: Time evolution of the mean magnetic field energy density normalized by the mean initial kinetic energy density, $\epsilon_{\rm B} = B^2/8\pi(\Gamma-1)n_0 m_{\rm e} c^2$. The black line shows $\epsilon_{\rm B}$ for the homogeneous density distribution. The green, red, and blue lines show $\epsilon_{\rm B}$ for the anisotropic density distributions with $L_{\rm x} = 120, 240, 480\ c/\omega_{\rm pe}$, respectively. The magenta dashed line represents the envelop of the second peaks of the three simulations, $\epsilon_{\rm B} = 0.08(t\omega_{\rm pe})^{-0.6}$. From Tomita & Ohira (2016).

Figure 5.8 shows the spatial distribution of $\epsilon_{\rm B}$ at the time of the second saturation, $t \sim 200\omega_{\rm pe}^{-1}$. The magnetic fields are efficiently amplified in the high- ($x \approx L_x/4$) and low- ($x \approx 3L_x/4$) density region. As seen in the Figure 5.8, the wave vector is parallel to the x- (y-) direction in the high- (low-) density region, and the wavelength is about $\sim 20c/\omega_{\rm pe}$. From the linear theory of the Weibel instability, the maximum-growth rate for a small temperature anisotropy ($A \ll 1$) is given by Eq. (4-3-24). For the observed $A \sim 0.25$ and $v_{\rm th} \sim 0.5$, the maximum-growth rate of the unstable mode with $k \approx 0.3\omega_{\rm pe}/c$ is $\gamma_{\rm max} \approx 10^{-2}\ \omega_{\rm pe}$. This is consistent with the timescale of the second growth of the magnetic field in our simulation. Therefore, we can conclude that the second generation of the magnetic field results from the Weibel instability which is driven in the anisotropic-temperature plasma produced by the anisotropic particle escape after the first saturation.

Finally, we discuss wether the second Weibel instability can explain the $\epsilon_{\rm B}$ suggested by the observation of the GRB afterglows. Since we cannot perform a much larger simulation, $t \sim 10^7\omega_{\rm pp}$ and $L_x \sim 10^7 c/\omega_{\rm pe}$, even using current supercomputers, we assume a scaling law of the second peak of $\epsilon_{\rm B}$ and compare with the observed properties. The dashed line in Figure 5.6 represents the envelope of the second peaks of the three simulations, and it is written by

$$\epsilon_{\rm B} \approx 0.08(t\omega_{\rm pe})^{-0.6} \ . \tag{5-2-6}$$

According to this scaling law, for the anisotropic density structures with $R \sim 10^7 c/\omega_{\rm pp}$,

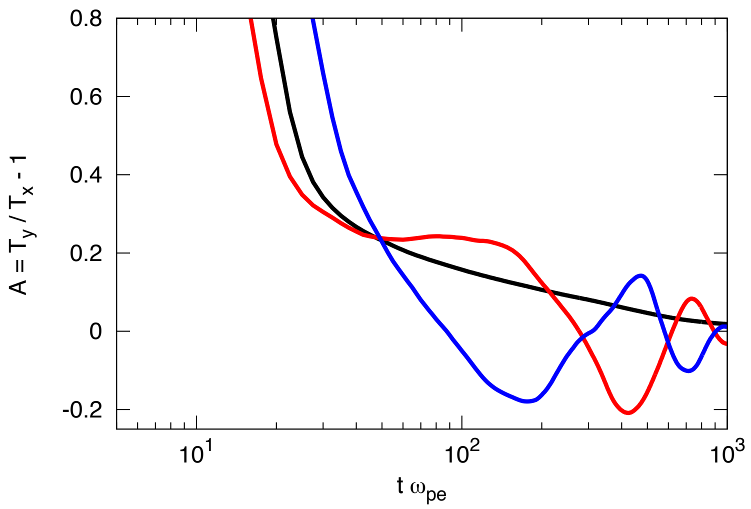

Figure 5.7: Time evolution of the temperature anisotropy, $A = T_{\rm y}/T_{\rm x} - 1$. The red and blue lines show A in the high ($50\ c/\omega_{\rm pe} < x < 70\ c/\omega_{\rm pe}$) and low ($170\ c/\omega_{\rm pe} < x < 190\ c/\omega_{\rm pe}$) density regions, respectively. The black line shows A measured in the whole simulation box ($0 < x < 240\ c/\omega_{\rm pe}$) for the homogeneous density distribution. From Tomita & Ohira (2016).

$\epsilon_{\rm B} \sim 10^{-5}$ at $t \sim 10^7\ \omega_{\rm pp}^{-1}$, which is consistent with the mean value of $\epsilon_{\rm B}$ suggested by observations of GRB afterglows. Observation of afterglows also shows the wide distribution of $\epsilon_{\rm B}$. As mentioned in the previous section, there would be various inhomogeneities in ISM, CSM, and shock precursor regions. The variety of the upstream inhomogeneities could make the broad distribution of $\epsilon_{\rm B}$.

5.3 The Weibel Mediated Shocks Propagating into Inhomogeneous Media

In section 5.2.2, we have assumed that the upstream density structure is just compressed in the downstream region by the shock wave. In other words, we have assumed an entropy wave in the shock downstream region. However, the linear analysis of hydrodynamics for a shock wave predicts not only the entropy wave but also a sound wave are generated in the downstream region. It is not clear whether the entropy and sound waves are actually generated in the downstream region of collisionless shocks. Furthermore, even though the entropy and sound waves are generated in the collsionless shock, they must be dissipated eventually. Although the dissipation mechanisms of the downstream entropy and sound waves are not understood, in order to dissipate these waves in a collisionless plasma, we can expect some plasma instabilities that generate magnetic fields. In this section, we perform PIC simulations of the Weibel mediated shocks propagating into inhomogeneous plasmas

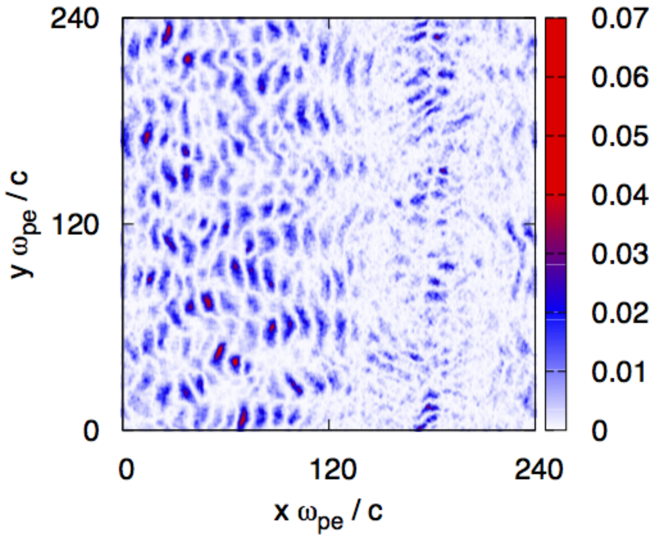

Figure 5.8: Spatial distribution of the magnetic energy density normalized by the mean initial kinetic energy density, $\epsilon_{\rm B} = B^2/8\pi(\Gamma-1)n_0 m_{\rm e}c^2$, for the anisotropic density distribution with $L_{\rm x} = 240\ c/\omega_{\rm pe}$ at $t = 200\ \omega_{\rm pe}^{-1}$. From Tomita & Ohira (2016).

for the first time.

Setting

We again use the two-dimensional electromagnetic PIC code (pCANS) to simulate a relativistic collisionless shock propagating into unmagnetized electron-positron plasmas. We suppress the numerical Cherenkov instability in relativistic plasma flows, solving Maxwell's equations by the implicit method with the Courant-Friedrichs-Lewy number $c\Delta t/\Delta x = 1.0$ (Ikeya & Matsumoto, 2015). We set a two-dimensional simulation box in the $x-y$ plane, with periodic boundary condition in the y-direction. The simulation box size is $L_x = 1.2\times10^4 c/\omega_{\rm pe}$ and $L_y = 86.4 c/\omega_{\rm pe}$. The skin-depth is defined by the upstream electron-positron plasma with a bulk Lorentz factor Γ and upstream mean number density n_0, i.e.,

$$\frac{c}{\omega_{\rm pe}} = \sqrt{\frac{\Gamma m_{\rm e} c^2}{4\pi n_0 e^2}}\ , \tag{5-3-7}$$

where constants c, e, m_e are speed of light, electron charge, and electron mass, respectively. The cell size and time step are $\Delta x = \Delta y = 0.1 c/\omega_{\rm pe}$ and $\Delta t = 0.1\omega_{\rm pe}^{-1}$, respectively. Unmagnetized plasma with the bulk Lorentz factor of $\Gamma = 10$ and the thermal velocity of $v_{\rm th} = 0.1c$ is injected from $x = L_x - ct$, where t is the simulation time. The shock is triggered by the reflecting the incoming particles at the conducting wall ($x = L_x$) and propagates toward the injection wall. The conducting wall represents the contact discontinuity. The formed shock corresponds to an external forward shock. The simulation frame is the downstream rest frame, that is, the downstream mean velocity is zero. We use 40 particles per cell per species on average. We set the inhomogeneous spatial distribution of electron-positron plasma in the upstream region as follows:

$$n(x,y) = n_0[1 + \delta n \sin(2\pi x/\lambda_x)] \;, \tag{5-3-8}$$

where δn and λ_x are the perturbation in the density and the wavelength of the upstream density wave in the downstream rest frame. We consider the case of a monochromatic wave. The upstream temperature is set to be constant for simplicity. Thereby, the pressure perturbation is also included in the upstream density flucutaion, but it is negligible for high-Mach number shocks.

Results

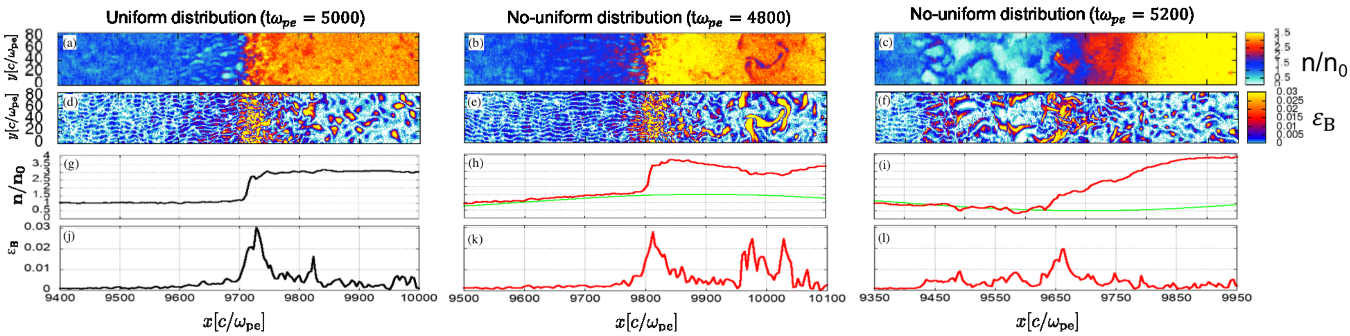

Figure 5.9: Structures of shocks for the homogeneous density distribution at $t\omega_{\rm pe} = 5000$ (left panels), and inhomogeneous case at $t\omega_{\rm pe} = 4800$ (middle panels) and 5200 (right panels). At $t\omega_{\rm pe} = 4800$ and 5200, the shock front is passing through the highest- and lowest-density regions, respectively. Panels (a)-(c) show the plasma density normalized by the upstream mean plasma density, n/n_0. Panels (d)-(f) show the magnetic energy density normalized by the upstream mean kinetic energy density, $\epsilon_{\rm B} = B^2/32\pi\Gamma n_0 m_{\rm e} c^2$. Panels (g)-(i) and panels (j)-(l) show transversely averaged n/n_0 and $\epsilon_{\rm B}$, respectively. The green curves in panels (h) and (i) show the initial density profile for the inhomogeneous case. From Tomita et al. (2019).

We show the shock structure for the case of inhomogeneous density distribution with $\lambda_x = 1200$ and $\delta n/n = 0.5$ while comparing with that of the homogeneous upstream one. The left column in Figure 5.9 shows the shock structures for the homogenous case at $t\omega_{\rm pe} = 5000$. From top to bottom, the four panels show the two-dimensional structures of normalized electron-positron density n/n_0 and the energy fraction of the magnetic field $\epsilon_{\rm B} = {\rm B}^2/(32\pi\Gamma {\rm n_0 m_e c^2})$, and one-dimensional profiles averaged over the y-direction of n/n_0 and $\epsilon_{\rm B}$, respectively. The shock front is located at $x \approx 9700\ c/\omega_{\rm pe}$ and moving leftward with the velocity of $v_{\rm sh} = (\gamma_{\rm ad} - 1) \times [(\Gamma - 1)/(\Gamma + 1)]^{1/2} \approx 0.45\ c$, where $\gamma_{\rm ad} \simeq 3/2$ is the upstream adiabatic index in two-dimensional relativistic gas. The left side of the shock front is the upstream region where magnetic filaments are generated by the Weibel instability. The transverse width of the Weibel filaments is about 8 $c/\omega_{\rm pe}$ in the upstream region. The magnetic field generated by the Weibel instability decays from the shock front to downstream. These features are consistent with early studies for relativistic Weibel mediated shocks (Spitkovsky, 2008b; Keshet et al., 2009). Compared with our previous periodic simulation (Section 5.2.2), the Weibel-mediated field is maintained for a long time in the shock simulation (note that $\epsilon_{\rm B}$ defined in this shock simulation is different with one in the periodic simulation.). This is because the magnetic field with a longer wavelength can be excited in the shock simulation. According to Keshet et al. (2009), the large-scale magnetic field is generated by high-energy particles accelerated by the shock.

The middle and right panels in Figure 5.9 display the time sequence of the shock structures for the inhomogeneous case at $t\omega_{\rm pe}$ =4800 and 5200, respectively. At $t\omega_{\rm pe} = 4800$ (middle panels in Figure 5.9), the shock front is passing through the highest-density region. Although the upstream structures are quite similar to those for the homogeneous case, one can see significant differences in the downstream region. At $x \approx 10000\ c/\omega_{\rm pe}$, there are large-scale filaments and the magnetic-field strength is comparable to that in the shock front. They are generated as the shock front passes through the lower-density region. The right column in Figure 5.9 shows the shock structures at $t\omega_{\rm pe} = 5200$ when the shock front is passing through the lowest-density region. The size of the upstream filaments is significantly larger than that for the homogeneous case. In addition, the magnetic field is generated in the broad upstream region (see panels (f) and (l)). The Weibel instability is driven by the cold upstream plasma and the hot plasma leaking from the downstream region. Since the density ratio of the hot leaking plasma to the cold upstream plasma becomes larger in the low-density region, the large momentum dispersion of the hot leaking plasma makes the transverse width of the filament wider (Ruyer et al., 2017). Since the length scale of the Weibel magnetic field is larger when the shock propagates in lower-density regions, it can be advected far downstream without dissipation. This is the reason why there is the large-scale magnetic field in the downstream region at $t\omega_{\rm pe} = 4800$ (panels (e) and (k)).

Next, we concentrate on the large-scale downstream structures of density and velocity for the inhomogeneous case. The blue and red curves in Figure 5.10 show the one-dimensional structures of x component of the average velocity, $\langle v_x \rangle/c$, and density, n/n_0, for the case of (a-d). The shock front in Figure 5.10 is located at $x \approx 9200\ c/\omega_{\rm pe}$. As seen in the blue curve in Figure 5.10, the average velocity oscillates with an amplitude of $\sim 0.2\ c$. The velocity profile (the blue curve) almost correlates with the large-scale density fluctuation. Therefore, the sinusoidal variation with the wavelength $\lambda_{\rm down} \approx 1100\ c/\omega_{\rm pe}$ can be interpreted as a sound wave propagating downstream. The propagation velocity in the downstream rest frame is about 0.62c that is consistent with a two-dimensional sound velocity of relativistic gas, $c/\sqrt{2}$.

There is another intermediate-scale density fluctuation with a wavelength of about $400\ c/\omega_{\rm pe}$ at $x \approx 9500$, 10000, 10500, 10900 $c/\omega_{\rm pe}$ in Figure 5.10, which is not associated with the velocity displacement. As shown in the dashed curve which represents the spatial profile of the density at $t\omega_{\rm pe} = 6000$, they are non-propagating. Therefore, this density fluctuation can be interpreted as an entropy wave.

As seen in the dashed red curve which shows the density at $t\omega_{\rm pe} = 6000$, the amplitude of the density wave oscillates with propagating downstream. This is because not only the resulting displacement of the entropy and sound waves but also beats caused by the interference between the sound wave propagating $+x$-direction and the one reflected at the

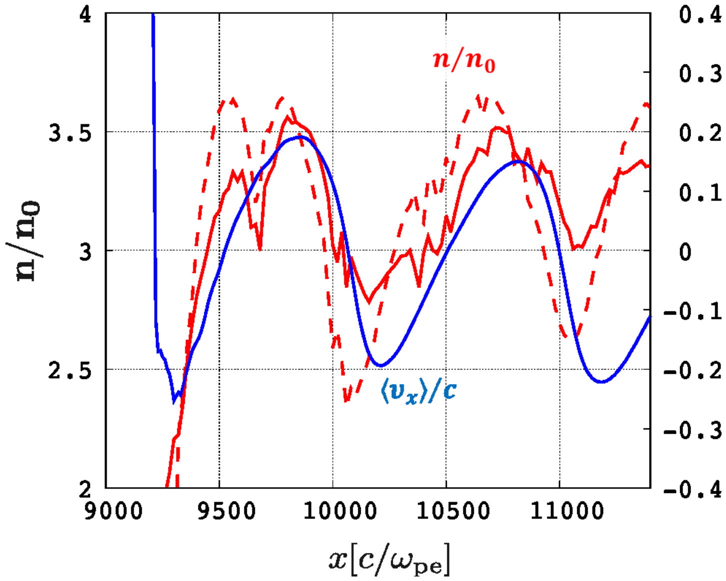

Figure 5.10: Spatial profiles of the x component of the average velocity, $\langle v_x \rangle/c$ (blue), and density, n/n_0 (red), measured in the downstream rest frame at $t\omega_{\rm pe} = 6100$ in the downstream region for the inhomogeneous upstream case. The dashed red curve shows the density at $t\omega_{\rm pe} = 6000$. The shock front is located at $x \approx 9200\ c/\omega_{\rm pe}$. From Tomita et al. (2019).

conducting wall.

The observed wavelengths of the entropy and sound waves are consistent with results from hydrodynamic analysis of interaction between a shock wave and a monochromatic density wave. This should never be taken for granted because we consider a collisionless system at finite temperature. If no particles change their momentum, density structures have to disappear in a sound crossing time. However, the simulation indicates that entropy and sound waves do not decay in the downstream region. The Weibel magnetic field changes the particle's momentum and plays an important role in the momentum exchange of particles. The gyroradius of thermal particles $r_{\rm g}$ is comparable to or slightly smaller than the coherence length of the Weibel magnetic field fluctuation, so that the diffusion coefficient of the thermal particles can be approximately given by

$$\kappa \sim \frac{1}{3} r_{\rm g} c = \frac{1}{3\sqrt{8}} \frac{c^2}{\omega_{\rm pe}} \epsilon_{\rm B}^{-1/2} \quad ,$$

Then, the decay time scales due to diffusion of the entropy and sound waves in the downstream region are given by

$$\begin{aligned} t_{\rm decay} &= \frac{\lambda_{\rm down}^2}{2\kappa} \\ &= \begin{cases} 9.9 \times 10^5 \ \omega_{\rm pe}^{-1} \left(\frac{\epsilon_{\rm B}}{10^{-2}}\right)^{1/2} \left(\frac{\lambda_{\rm down}}{1.1\times10^3 c/\omega_{\rm pe}}\right)^2 \\ \qquad\qquad\qquad\qquad \text{(for sound wave)} \\ 1.3 \times 10^5 \ \omega_{\rm pe}^{-1} \left(\frac{\epsilon_{\rm B}}{10^{-2}}\right)^{1/2} \left(\frac{\lambda_{\rm down}}{4.0\times10^2 c/\omega_{\rm pe}}\right)^2 \\ \qquad\qquad\qquad\qquad \text{(for entropy wave).} \end{cases} \end{aligned} \tag{5-3-9}$$

The decay time scales of the sound and entropy waves are much longer than the simulation time, $t\omega_{\rm pe} = 6100$ and sound crossing time, $t\omega_{\rm pe} = 1935$. Therefore, the both waves can propagate in the downstream region during the simulation time.

In Figure 5.11, we compare the spatial profile of the transversely averaged $\epsilon_{\rm B}$ in larger downstream region at $t\omega_{\rm pe} = 6100$ for the homogeneous and inhomogeneous density distributions, respectively. The shock front is located at $x \approx 9200\ c/\omega_{\rm pe}$ and passing through the lower-density region for the inhomogeneous case. For the homogeneous case, the magnetic field generated in the shock transition region simply decays downstream. For the inhomogeneous case, we can see two peaks of $\epsilon_{\rm B}$ downstream, which decay much slower than that for the homogeneous case. The number of the peaks is the same as that of the waves which transmitted through the shock. That is, $\epsilon_{\rm B}$ in the two peaks is generated when the shock propagates into the low-density region. Therefore, the inhomogeneity of the upstream density has an important role on the magnetic field generation far downstream.

Finally, we confirm whether the temperature anisotropy is generated and excites the Weibel instability in the downstream region. Figure 5.12 shows the spatial profile of temperature anisotropy averaged over the y-direction in the downstream region for the homogeneous (back solid) and inhomogeneous (red solid) cases at $t\omega_{\rm pe} = 6100$. The blue dashed curve represents the x component of the average velocity, $\langle v_x \rangle / c$. The temperature anisotropy is defined by $T_y/T_x - 1$, where according to Yoon & Lui (2007) the temperatures

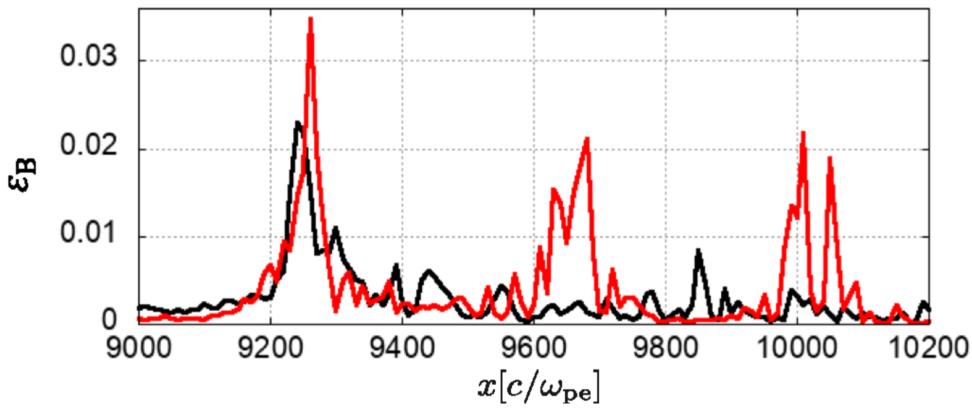

Figure 5.11: Spatial profiles of the transversely averaged $\epsilon_B = B^2/32\pi\Gamma n_0 m_e c^2$ in the larger downstream region at $t\omega_{pe} = 6100$ for the homogeneous (black) and inhomogeneous (red) density distributions, respectively. The shock front is located at $x \approx 9200\ c/\omega_{pe}$. From Tomita et al. (2019)

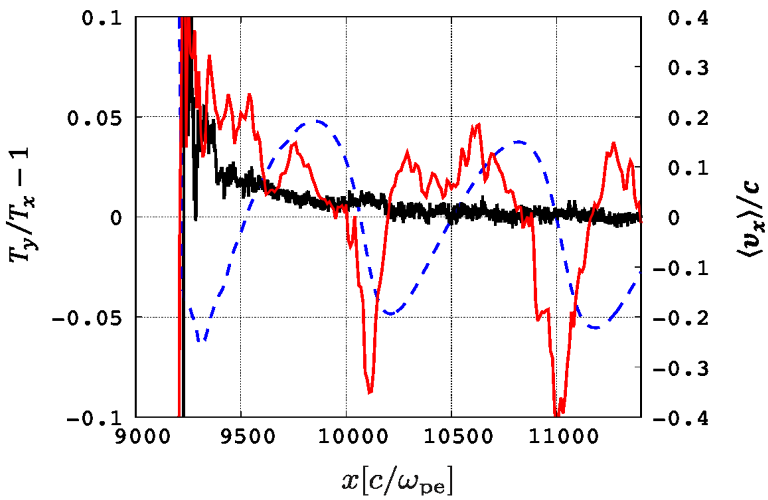

Figure 5.12: Spatial profiles of the temperature anisotropy at $t\omega_{pe} = 6100$ in the downstream region for the case of homogeneous (black) and inhomogeneous (red) upstream density distribution, respectively. The blue dashed curve shows the x component of the average velocity for the inhomogeneous case, $\langle v_x \rangle/c$ measured in the downstream rest frame. The shock front is located at $x \approx 9200\ c/\omega_{pe}$. From Tomita et al. (2019).

T_x and T_y are defined as follows,

$$T_x = \int \mathrm{d}^3 p \frac{p_x^2}{\gamma m_e} f(p_x, p_y, p_z), \tag{5-3-10}$$

$$T_y = \int \mathrm{d}^3 p \frac{p_y^2}{\gamma m_e} f(p_x, p_y, p_z). \tag{5-3-11}$$

Here, γ, f, p_x, p_y, and p_z are the particle Lorentz factor, the distribution function and momentum in the center-of-mass rest frame which is calculated by all particles in region of width $\sim 20c/\omega_{\mathrm{pe}}$ over the y-direction. After passing through the shock front, the temperature anisotropy rapidly decreases and becomes almost zero in the downstream region for the homogeneous case. On the other hand, for the inhomogeneous case, it oscillates synchronously with the sound wave with values ranging from -0.1 to 0.05. As seen in Figure 5.12, the absolute value of the temperature anisotropy becomes maximum at $x \approx 10100c/\omega_{\mathrm{pe}}$ and $\approx 11000c/\omega_{\mathrm{pe}}$ where the divergence of the mean velocity is negative. As discussed above, the particle diffusion in the sound wave is negligible for thermal particles during this simulation time. On the other hand, for high-energy particles accelerated by the shock, their gyroradii is larger than the coherent length scale of the magnetic-field fluctuations, so that the diffusion of high-energy particles is not negligible. Therefore, the mean motion of the high energy particles deviates from the sound wave motion. In Figure 5.13, we show the cartoon illustrating the momentum distribution in $p_x - p_y$ plane at the regions A, B, and C, where mean velocities are $\langle v_x \rangle > 0$, $= 0$, and < 0, respectively. The blue dashed circles are isotropic momentum distribution in the rest frame of regions A and C. If they are measured in the rest frame of region B, the momentum distributions are represented as the red circles by the Lorentz transformation. The color contrast (dark or light) represents the density contrast (high or low). Since the sound wave motion concentrates particle on the region B, high-energy particles in the regions A and C are more concentrated in the region B. As a result, the momentum distribution in the region B has larger momentum dispersion along the p_x-direction, so that the temperature in the x-direction becomes larger than that in the y-direction. Meanwhile, the region A and C lose particles with large p_x, so that , the temperature in the x-direction becomes smaller than that in the y-direction. Therefore, the temperature anisotropy in the downstream region is generated by the sound wave motion and diffusive motion of high-energy particles. In reality, the high-energy electrons efficiently cools down due to radiation, so that the temperature anisotropy generated by the diffusive motion of high-energy electrons would become small. However, protons do not loss their energy efficiently. Then, the temperature anisotropy generated by the high-energy protons becomes important for the generation of the magnetic field in the downstream region.

The temperature anisotropy can generate magnetic field by the Weibel instability in the downstream region. However, the observed temperature anisotropy oscillates downstream. We need to compare the growth time scale of the magnetic field and oscillation period of the temperature anisotropy in order to investigate whether the magnetic field is generated by the Weibel instability or not. According to the maximum growth rate of the relativistic Weibel instability, for the temperature anisotropy of 0.05 observed in our simulation, the growth time scale is

$$\begin{aligned} t_{\mathrm{grow}} &= \gamma_{\mathrm{max}}^{-1} \\ &\approx 20\omega_{\mathrm{pe}}^{-1} \left(\frac{T_x/m_{\mathrm{e}}c^2}{3.8}\right)^{-1} \left(\frac{T_y/T_x - 1}{0.05}\right)^{-3/2} \left(\frac{\Gamma}{10}\right)^{-1/2} . \end{aligned}$$

The oscillation period of the temperature anisotropy is that of the sound wave, $\lambda_{\mathrm{down}}/c_{\mathrm{s}} \approx 1.7 \times 10^3 \omega_{\mathrm{pe}}^{-1}$. Since $t_{\mathrm{grow}} < \lambda_{\mathrm{down}}/c_{\mathrm{s}}$, the Weibel-unstable mode should grow in the downstream anisotropic temperature plasma. However, we could not identify the magnetic field generated by the Weibel instability in the downstream region. This might be because the above growth time sale is given by the linear analysis of the Weibel instability in unmagnetized plasma, so that the growth rate is suppressed by the downstream magnetic field generated in the shock front. In addition, it should be noted that the linear analysis of the Weibel instability assumed the Maxwell-Jüttner distribution. However, non-thermal particles are accelerated in our simulation and make the temperature anisotropy mainly. This could also be the reason for the discrepancy in the growth rate. Even if the free energy of the temperature anisotropy is fully converted to the magnetic-field energy density during $t_{\mathrm{grow}} \approx 20\omega_{\mathrm{pe}}^{-1}$, we cannot see it significantly in the downstream field of the strength keeping a few percent. If the magnetic field generated in the shock font significantly decays in the far downstream region, the observed temperature anisotropy could be crucial role in the generation of the magnetic field in the far-downstream region.

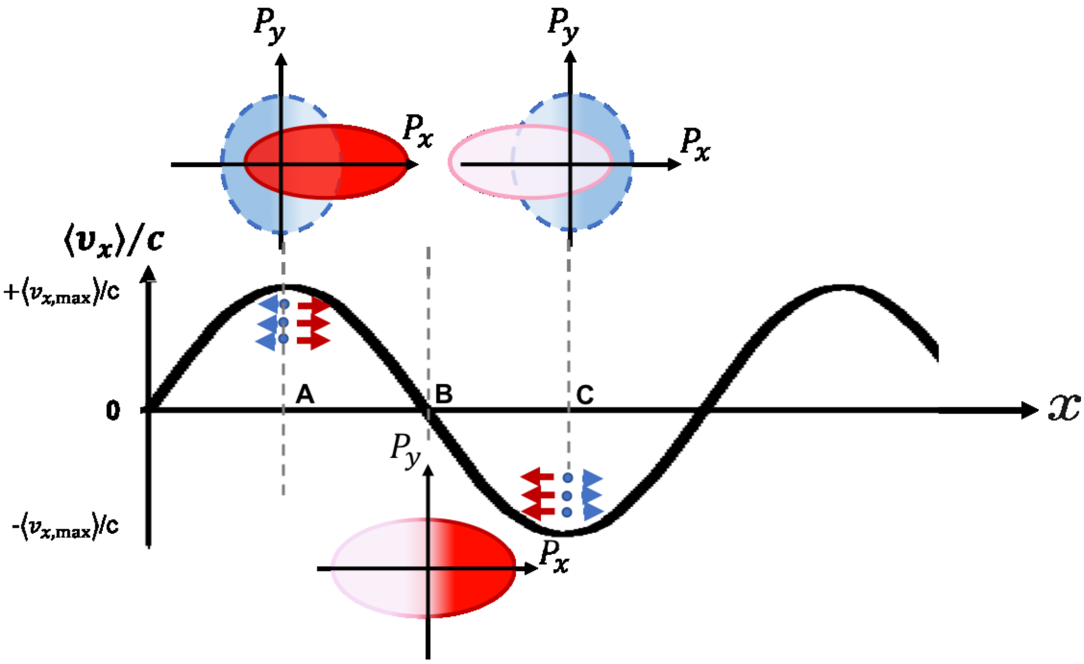

Figure 5.13: Generation mechanism of the temperature anisotropy in the downstream region. The blue dashed circles are isotropic momentum distribution in the rest frame of regions A and C. The red solid circles are the momentum distribution measured in the rest frame of region B (downstream rest frame). The black curve is the spatial profile of x component of the average velocity, $\langle v_x \rangle / c$. From Tomita et al. (2019).

Chapter 6

Discussion

In this thesis, we have investigated effects of upstream inhomogeneity on unmagnetized relativistic collisionless shocks by means of PIC simulations. In our simulation, the upstream density sinusoidally changes with a wavelength of $1.2 \times 10^3\ c/\omega_{\rm pe}$ in the downstream rest frame, which is much larger than the thickness of the shock transition region, the characteristic length scale of the Weibel instability, and the kinetic scale of plasmas. Although it is still much smaller than the injection scale of the interstellar turbulence ($\sim 1 - 100$ pc), there are some mechanisms that generate the small-scale density fluctuations in a precursor region of collisionless shocks (Drury & Falle, 1986; Ohira, 2013b, 2014, 2016). In addition, stellar winds contain small-scale density variation compared with the ISM turbulence. These small-scale density fluctuations could play an important role in collisionless shocks.

6.1 Generation of Large-Scale Magnetic Field

Our simulation shows that, compared with results for shocks into a uniform plasma, a larger-scale magnetic field is generated in the shock precursor region when the shock propagates into a low-density region in the inhomogeneous plasma. The density ratio of the hot leaking plasma to the upstream cold plasma becomes larger in the low-density region. Then, a finite temperature effect on the Weibel instability becomes significant in the low-density region, so that the characteristic length of the Weibel instability is thought to be larger. Hence, the larger-scale magnetic field hardly decays after they were advected downstream. The long-lived large-scale field is anticipated in GRB afterglows and could make a particle acceleration more efficient although this effect was not observed in this simulation because of a short simulation time. We performed other simulations for smaller $\delta n/n_0$. Although the results are not shown here, the coherent length of the upstream magnetic field depends on the upstream density fluctuation, and it becomes smaller for smaller $\delta n/n_0$. Furthermore, it may be limited by the wavelength of the upstream density fluctuation. If we consider a longer length scale of upstream density fluctuations, the coherence length and the decay time in the downstream region of generated magnetic fields would be longer. However, we also note that the actual upstream plasma is in general weakly magnetized. The gyroradius of leaking ions in the downstream rest frame is $\sim 10^{12}\ {\rm cm}(B_{\rm up}/3\ \mu{\rm G})^{-1}$, where $B_{\rm up}$ is the upstream magnetic field in the upstream rest frame. For accelerated particles, their gyroradii become much longer than the above estimate. When the wavelength of the upstream density fluctuation in the downstream rest frame is larger than the above gyroradii, the large-scale magnetic field generation that we observed would not work. Alternatively, the magnetic field is amplified by the downstream MHD turbulence. As mentioned above, the characteristic scale of the density fluctuation around GRB progenitors has not been understood yet. Therefore, the gyroradii of leaking particles would be larger than the length scale of the upstream density fluctuations.

6.2 Magnetic Field Amplification in the Sound Wave

We found that the upstream density variation generates sound waves in the downstream region. The downstream sound waves are responsible for the temperature anisotropy which can generate the magnetic field by the Weibel instability. Therefore, the energy of the downstream sound waves is expected to be converted to the downstream magnetic-field energy. Our simulations have shown that the ratio of the sound-wave energy density $4n_0\Gamma m_\mathrm{e}\langle v\rangle^2/2$ to the kinetic energy density is

$$\epsilon_\mathrm{sw} \sim 0.02 \times \left(\frac{\langle v\rangle}{0.2c}\right)^2 \quad , \tag{6-2-1}$$

where the downstream density is assumed to be $4n_0$ and n_0 is the upstream number density in the downstream rest frame. Furthermore, our simulation have shown that temperature anisotropy on the order of 10^{-2} is generated in the downstream region by the sound wave, which means that the ratio of the free energy of the temperature anisotropy to the downstream kinetic energy is $\epsilon_\mathrm{ani} \sim 10^{-2}$. Since observations of GRB afterglows suggest the energy fraction of magnetic field with $\epsilon_\mathrm{B} \sim 10^{-5}$ (Santana et al., 2014) which is smaller than ϵ_sw and ϵ_ani, the energies of the downstream sound wave and temperature anisotropy are sufficient to generate the magnetic field in the afterglow emission region. Therefore, for shocks in inhomogeneous plasmas, the magnetic field generation takes place not only at the shock precursor region but also far downstream of the shock.

In order for the upstream density fluctuations to affect the GRB afterglow emission, the wavelength, λ^u measured in the upstream frame, must be smaller than the deceleration radius of GRB jet, $R^\mathrm{u}_\mathrm{dec}$, that is,

$$\lambda^\mathrm{u} < R^\mathrm{u}_\mathrm{dec} = 1.2 \times 10^{17} \left(\frac{E_\mathrm{iso,53}}{n^\mathrm{u}_0}\right)^{1/3} {\Gamma^\mathrm{u}_\mathrm{sh,2}}^{-2/3}\ \mathrm{cm} \quad , \tag{6-2-2}$$

where $E_\mathrm{iso,53}, n^\mathrm{u}_0$ and $\Gamma^\mathrm{u}_\mathrm{sh,2}$ are the isotropic equivalent kinetic energy of the blast wave in unit of erg, upstream density in unit of cm^{-3} and the initial Lorentz factor of the shock measured in the upstream rest frame, respectively (e.g. Sironi & Goodman, 2007). We have adopted the usual notation $\mathcal{Q}_n \equiv \mathcal{Q}/10^n$. For a later phase of GRB afterglows, the upstream density fluctuations with longer wavelength generate downstream magnetic field.

In the hydrodynamics, a finite-amplitude sound wave eventually steepens to a shock-like structure, and the wave motion is thermalized by dissipation. The lifetime of a downstream sound wave with the wavelength of λ_down in the downstream rest frame is given by (Stein et al., 1972)

$$t_\mathrm{lifetime} = \frac{\lambda_\mathrm{down}}{\langle v\rangle} + t_\mathrm{dis} \quad . \tag{6-2-3}$$

The first term represents a steepening time in which the sound wave becomes a shock-like structure. The second term represents a dissipation time. If the dissipation is mainly due to the shock wave, the dissipation time is given by $t_{\rm dis} = \lambda_{\rm down}/\langle v\rangle(M-1)$, where M is a Mach number (Stein et al., 1972). However, at present we have not understood the main dissipation mechanism and cannot estimate the dissipation time because we consider a collisionless system. In this discussion, we consider only the steepening time as a lower limit of the lifetime of the downstream sound wave. Observed GRB afterglows are already bright until the deceleration time, $t^{\rm u}_{\rm dec} = R^{\rm u}_{\rm dec}/c$, at which observers see the emission peak in the optical band. Hence, the field generation occurs until this epoch, so that $\Gamma^{\rm u}_{\rm sh} t_{\rm lifetime}/\sqrt{2} > t^{\rm u}_{\rm dec}$. Thus, the lower limit of the wavelength of the upstream density fluctuation is given as,

$$\begin{aligned} \lambda^{\rm u} > & \ 9.6 \ \times 10^{16} \left(\frac{c_s}{0.62c}\right)^{-1} \left(\frac{\langle v\rangle}{0.2c}\right) \\ \times & \left(\frac{E_{\rm iso,53}}{n^{\rm u}_0}\right)^{1/3} \Gamma^{\rm u \ -2/3}_{\rm sh,2} \ {\rm cm} \ , \end{aligned} \tag{6-2-4}$$

where we use $\lambda^{\rm u} \sim \Gamma^{\rm u}_{\rm sh}\lambda_{\rm down}$ (Lemoine et al., 2016). Since we ignore the dissipation time in this discussion, the above lower limit actually should be smaller.

6.3 Magnetic field Amplification in the Entropy Wave

In Section 5.2.2, we investigated effects of particle diffusion from an entropy mode in the shock downstream region by local PIC simulations with periodic boundary conditions. We showed that the magnetic field is generated by the Weibel instability in spatially anisotropic density structures. However, the anisotropic escape of particles from the entropy mode was not observed in this shock simulation. This is because the strength of the large-scale long-lived magnetic field is large enough to suppress the particle diffusion from the entropy mode. Instead of that, high-energy accelerated particles escape from high-density regions of the sound wave, which makes temperature anisotropy in the shock downstream region. The large-scale magnetic field generated in the shock precursor region would decay more rapidly in a realistic three-dimensional simulation. In that case, the downstream entropy and sound waves would also rapidly dissipate due to the particle diffusion, so that the temperature anisotropy would be generated by the anisotropic escape from high-density regions. Therefore, a realistic three-dimensional PIC simulation should be performed in the future even though it is very challenging.

6.4 Particle acceleration

Since our PIC simulations solve plasmas as particles, we can make the energy spectrum at any regions. Figure 6.1 shows the energy spectra in the shock downstream region for the homogeneous (black curve) and inhomogeneous (red curve) cases. As one can see, the energy spectra are not a Maxwell distribution. There are many nonthermal high-energy particles compared with the Maxwell distribution. The early studies for the homogenous case show that the high energy particles are accelerated by the diffusive shock acceleration mechanism. For the inhomogeneous case, although the maximum energy does not change, the number of particles in the energy range $20 < \gamma < 100$ is significantly larger than that of the homogeneous case. We have not understood why the shock in the inhomogeneous plasma efficiently accelerates particles compared with the shock in the homogenous plasma. The large scale magnetic field and sound waves produced by the shock in the inhomogeneous plasma would play an important role in the efficient particle acceleration. By tracking motion and acceleration of the accelerated particles in our simulations, we can identify the origin of the efficient particle acceleration, which will be addressed in the future.

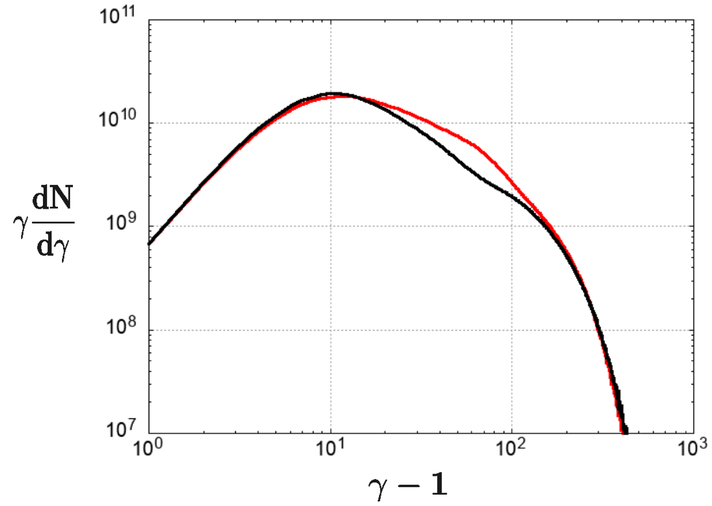

Figure 6.1: Energy spectra in the shock downstream region, which are obtained from the PIC simulations performed in Section 5.3. The black and red curves show the energy spectra for the homogeneous and inhomogeneous cases, respectively.

6.5 Application to GRB Afterglows

The standard model of the GRB afterglows assumes that the radiation mechanism is synchrotron emission from non-thermal electron in the homogeneous magnetic field. Early PIC simulations show that the magnetic field decays in the shock downstream region for the homogeneous plasma case. Furthermore, there are some theoretical models for the GRB afterglow, which consider the decaying magnetic field (Rossi, & Rees, 2003; Derishev, 2007; Lemoine, 2013; Uhm & Zhang, 2014; Zhao et al., 2014). However, our PIC simulations for the inhomogeneous plasma case show that the magnetic field does not simply decay in the downstream region, but there are locally the large-scale ($\gg c/\omega_{\rm p}$) magnetic field in the downstream region. Moreover, our PIC simulations suggest that the small-scale ($\sim c/\omega_{\rm p}$) magnetic field would be generated in the shock downstream region by the temperature anisotropy. Therefore, both synchrotron and jitter radiations would contribute the GRB afterglows.

The standard model of the GRB afterglows assumes that the emission region is downstream regions. However, PIC simulations show that the magnetic field is generated not only in the shock downstream region, but also in the upstream region. In addition, there are many nonthermal particles in the shock upstream region because of the diffusive shock acceleration. Therefore, we should estimate the synchrotron, jitter, and inverse Compton emissions from the shock upstream region quantitatively.

To calculate all the radiation spectra, we need the energy spectrum and spatial distribution of nonthermal particles. In addition, to calculate the jitter radiation, the power spectra of magnetic field fluctuations are needed. PIC simulations give us all the information that we need, so that we will be able to make a testable prediction for the GRB afterglows.

6.6 Future Work

In this thesis, we have studied a case where the wave vector of the upstream density fluctuation is parallel to the shock normal direction. In reality, there are clumpy structures in the ISM or CSM. When a high-density clump passes through the shock front, not only compressible modes but also vortexes (incompressible modes) are excited in the downstream region. If the particle diffusion works, the escape of particles from the vortex can generate the temperature anisotropy as the sound wave makes it. Magnetic-field lines generated by the Weibel instability might be stretched to a large scale by the vorticity. Then, the magnetic field would be further amplified by the turbulent dynamo. On the other hand, if the particle diffusion works efficiently, the vortex rapidly decays and the turbulent dynamo becomes inefficient compered with ideal MHD case. However, if the shock-compressed background magnetic field is rapidly amplified by the turbulent dynamo before particles escape from the high-density clump, the diffusion is strongly suppressed, so that the small-scale magnetic field cannot be generated by the Weibel instability. A larger simulation box and a longer simulation time are required to understand the effect of vortexes on collisionless shocks, which will be addressed in future work.

The decay of the turbulence means heating or acceleration of particles by the turbulence. Although we cannot see in this study a significant difference of the number of high-energy particles between the homogeneous and inhomogeneous cases, the second-order Fermi-acceleration by the downstream large-scale turbulence is expected in larger and longer simulations (Ohira, 2013a; Asano & Terasawa, 2015).

We considered only electron-positron plasma in this study. For the standard model of the GRB afterglow, the external shock wave propagates to an electron-ion plasma. When the shock is ultra-relativistic, the downstream electron and ion temperatures become almost the same (Spitkovsky, 2008a; Kumar et al., 2015). Then, the results for electron-positron plasmas would be applicable to GRB afterglows. However, the shock eventually becomes nonrelativistic at a later phase of the GRB afterglow. Therefore, in reality, three-dimensional effects, the upstream magnetic fields, multidimensional density structures, nonrelativistic physics, and ion inertia could play important roles on the GRB afterglow and collisionless shocks propagating to inhomogeneous plasmas. More realistic simulations should be performed to understand these effects. Although it is very challenging for numerical simulations, we may be able to reveal it in the laboratory astrophysics (Takabe et al., 2008). Furthermore, we can apply their knowledge to supernova remnant shocks which are believed to be the cosmic-ray accelerator in our galaxy.

Chapter 7

Overall Conclusions

In this thesis, we have studied relativistic collisionless shocks propagating into inhomogeneous plasmas to understand emission from GRB afterglows. To understand the particle acceleration, the plasma heating, and the magnetic field amplification mechanisms in the GRB afterglow shocks, we have to understand what collisionless plasma instabilities really occur and their nonlinear developments. As a first step, we have considered a relativistic collisionless shock in an unmagnetized eletron-positron plasma. To obtain better understanding of nonlinear development of the collsionless shock, we have performed particle-in-cell (PIC) simulations. We have summarized our important results as follows.

7.1 Simulation in a Local Shock Downstream Region

In chapter 5.2, we have investigated the magnetic field amplification due to the Weibel instability driven by anisotropic density structures. When a relativistic shock propagates through inhomogeneous media, an anisotropic density structure is generated by the relativistic shock compression in the downstream region. We proposed a new model for the magnetic field amplification. Thanks to an anisotropic escape of high-energy particles from the high-density region, a temperature anisotropy is generated and excites the Weibel instability in the downstream region. So far, there are many fluid simulation for the interaction between a shock and a high density clump. We first pointed out the importance of kinetic effects in the interaction between a collsionless shock and a high density clump. We have performed two-dimensional PIC simulations to demonstrate our model. The results are summarized as follows:

- We have demonstrated that the anisotropy in momentum space is generated by the anisotropic escape of high-energy particles from the anisotropic density structure.
- The generated anisotropy in the momentum space excite the Weibel instability and generated the magnetic field for a longer time than considered so far.
- We have investigated how the generated magnetic field depends on the length scale of the density fluctuations. Applying the dependence to the observation of GRB afterglows, we have shown that the magnetic field generated by the Weibel instability

in the anisotropic density structure can explain the value of $\epsilon_{\rm B}$ suggested by the observation of the afterglows.

7.2 Simulation for Collsionless Shocks Propagating to an Inhomogeneous Plasma

In chapter 5.3, we have investigated effects of upstream density fluctuation on collisionless shocks.

The interstellar or circumstellar matters around GRBs are not completely uniform. A variety of the density fluctuation could be the origin of the observed large dispersion of $\epsilon_{\rm B}$. So far, there are many fluid simulation for the interaction between a shock and a high density clump (e.g. McKenzie & Westphal, 1968; Shu & Osher, 1989; Inoue et al., 2011; Mizuno et al., 2011; Lemoine et al., 2016; Arshed & Hoffmann, 2013). The fluid simulations showed that sound and entropy waves are generated in the shock downstream region. It is not obvious in a collisionless system. Furthermore, the fluid simulations showed that the strong turbulence is generated in the downstream region by the interaction (Inoue et al., 2011; Mizuno et al., 2011). However, kinetic behaviors in the interaction have never been studied. We have performed PIC simulations of collisionless shocks propagating into inhomogeneous plasmas for the first time. The results are summarized as follows:

- The entropy and sound waves are formed in the downstream region of the Weibel mediated collisionless shock.
- The large-scale magnetic field is generated by the Weibel instability in the low density region of the precursor region, being maintained in the far downstream region. The large-scale magnetic field provides particle interactions though the Lorentz force, so that the entropy and sound waves are generated as with a fluid system.
- We found a new generation mechanism of the temperature anisotropy. The temperature anisotropy is produced in the shock downstream region by the sound wave and diffusive motion of high-energy particles. The free energy of the temperature anisotropy is large enough to make the field strength suggested by GRB observations.

References

Abbott, B. P., Abbott, R., Abbott, T. D., et al. 2017, Physical Review Letters, 119, 161101

Abdo, A. A., Ackermann, M., Ajello, M., et al. 2009, Astrophysical Journal, 706, 1331

Abdo, A. A., Ackermann, M., Arimoto, M., et al. 2009, Science, 323, 1688

Ajello, M., Arimoto, M., Axelsson, M., et al. 2019, Astrophysical Journal, 878, 52

Ajello, M., Arimoto, M., Axelsson, M., et al. 2019, arXiv e-prints, arXiv:1909.10605

Amati, L., Frontera, F., Tavani, M., et al. 2002, Astronomy and Astrophysics, 390, 81

Armstrong, J. W., Rickett, B. J., & Spangler, S. R. 1995, Astrophysical Journal, 443, 209

Arshed, G. M., & Hoffmann, K. A. 2013, Journal of Computational Physics, 246, 58

Asano, K. & Terasawa, T. 2015, Monthly Notices of the RAS, 454, 2242

Band, D., Matteson, J., Ford, L., et al. 1993, Astrophysical Journal, 413, 281

Berger, E., Kulkarni, S. R., & Frail, D. A. 2003, Astrophysical Journal, 590, 379

Bersier, D., Stanek, K. Z., Winn, J. N., et al. 2003, Astropysical Journal, Letters, 584, L43

Blandford, R. D., & McKee, C. F. 1976, Physics of Fluids, 19, 1130

Bloom, J. S., Djorgovski, S. G., & Kulkarni, S. R. 2001, Astrophysical Journal, 554, 678

Bošnjak, Ž., & Daigne, F. 2014, Astronomy and Astrophysics, 568, A45

Briggs, M. S., Band, D. L., Kippen, R. M., et al. 1999, Astrophysical Journal, 524, 82

Burrows, D. N., Romano, P., Falcone, A., et al. 2005, Science, 309, 1833

Chang, P., Spitkovsky, A., & Arons, J. 2008, Astrophysical Journal, 674, 378

Chugai, N. N., & Danziger, I. J. 1994, Monthly Notices of the RAS, 268, 173

Costa, E., Frontera, F., Heise, J., et al. 1997, Nature, 387, 19

Dai, Z., D., & Wu, X., F. 2003, Astrophysical Journal, 591, 21

Davidson, R. C., Hammer, D. A., Haber, I., et al. 1972, Physics of Fluids, 15, 317

De Pasquale, M., Evans, P., Oates, S., et al. 2009, Monthly Notices of the RAS, 392, 153

Derishev, E. V. 2007, Astrophysics and Space Science, 309, 157

Derishev, E., Piran, T. 2019, Astropysical Journal, Letters, 880, 27

Drury, L. O., & Falle, S. A. E. G. 1986, Monthly Notices of the RAS, 223, 353

Dai, Z. G., & Lu, T. 2002, Astropysical Journal, Letters, 565, L87

Fan, Y., & Piran, T. 2006, Monthly Notices of the RAS, 369, 197

FIshman, G., Meegan, C. 1995, Annual Review of Astron and Astrophys, 33, 415

Fox, W., Fiksel, G., Bhattacharjee, A., et al. 2013, Physical Review Letters, 111, 225002

Frail, D. A., Kulkarni, S. R., Nicastro, L., et al. 1997, Nature, 389, 261

Galama, T., Groot, P. J., Vanparadijs, J., et al. 1997, Nature, 387, 479

Gehrels, N., Sarazin, C. L., O'Brien, P. T., et al. 2005, Nature, 437, 851

Genet, F., Daigne, F., & . Mochkovitch, R. 2007, Monthly Notices of the RAS, 381, 732

Ghirlanda, G., Nava, L., Ghisellini, G., et al. 2012, Monthly Notices of the RAS, 420, 483

Ghisellini, G., Ghirlanda, G., Nava, L., & Celotti, A. 2010, Monthly Notices of the RAS, 403, 926

Goodman, J. 1986, Astrophysical Journal, 308, 47

Goodman, J. 1997, New Astronomy, 2. 5

Godfrey, B. B. 1974, Journal of Computational Physics, 15, 504

Granot, J., Nakar, E., & Piran, T. 2003, Nature, 426, 138

Granot, J., Königle, A., & Piran, T. 2006, Monthly Notices of the RAS, 370, 1946

Gruzinov, A., & Waxman, E. 1999, Astrophysical Journal, 511, 852

Harrison, F. A., Bloom, J. S., Frail, D. A., et al. 1999, Astropysical Journal, Letters, 523, L121

Heyl, J. S., & Perna, R. 2003, Astropysical Journal, Letters, 586, L13

Holland, S. T., Weidinger, M., Fynbo, J. P. U., et al. 2003, Astronomical Journal, 125, 2291

Huang, Y. F., Wu, X. F., Dai, Z. G., et al. 2004, Astrophysical Journal, 605, 300

Huntington, C. M., Fiuza, F., Ross, J. S., et al. 2015, Nature Physics, 11, 173

Ikeya, N., Matsumoto, Y. 2015, PASJ, 67, 64

Inoue, T., Asano, K., & Ioka, K. 2011, Astrophysical Journal, 734, 77

Ioka, K., Kobayashi, S., & Zhang, B. 2005, Astrophysical Journal, 631, 429

Ioka, K., Toma, K., Yamazaki, R., et al. 2006, Astronomy and Astrophysics, 458, 7

Jakobsson, P., Hjorth, J., Ramirez-Ruiz, E., et al. 2004, New Astronomy, 9, 435

Kato, T. N. 2005, Physics of Plasmas, 12, 080705

Kato, T. N., & Takabe, H. 2010, Astrophysical Journal, 721, 828

Katz, J. I. 1994, Astrophysical Journal, 422, 248

Katz, J. I., Piran, T., & Sari, R. 1998, Physical Review Letters, 80, 1580

Katz, B., Keshet, U., & Waxman, E. 2007, Astrophysical Journal, 655, 375

Keshet, T., Katz, B., Spitkovsky, A., & Waxman, E. 2009, Astropysical Journal, Letters, 693, L127

Klebesadel, R. W., Strong, I. B., & Olson, R. A. 1973, Astropysical Journal, Letters, 182, L85

Kouveliotou, C., Meegan, C. A., Fishman, G. J., et al. 1993, Astropysical Journal, Letters, 413, L101

Kulkarni, S. R., Djorgovski, S. G., Odewahn, S. C., et al. 1999, Nature, 398, 389

Kumar, P., & Piran, T. 2000, Astrophysical Journal, 535, 152

Kumar, P., & Piran, T. 2000, Astrophysical Journal, 532, 286

Kumar, P., & Barniol Duran R. 2009, Monthly Notices of the RAS, 400, 75

Kumar, P., & Barniol Duran, R. 2010, Monthly Notices of the RAS, 409, 226

Kumar, R., Eichler, D., & Gedalin, M. 2015, Astrophysical Journal, 806, 165

Lamb, D. Q. 1995, Publications of the ASP, 107, 1152

Lazzati, D., Rossi, E., Covino, S., et al. 2002, Astronomy and Astrophysics, 396, L5

Lemoine, M. 2013, Monthly Notices of the RAS, 428, 845

Lemoine, M. 2015, Journal of Plasma Physics, 81, 455810101

Lemoine, M., Ramos, O., & Gremillet, L. 2016, Astrophysical Journal, 827, 44

Lemoine, M., Gremillet, L., Pelletier, G., et al. 2019, Physical Review Letters, 123, 035101

Lemoine, M., Vanthieghem, A., Pelletier, G., & Gremillet, L., 2019,Physical Review E, 100, 033210

Lemoine, M., Vanthieghem, A., Pelletier, G., et al. 2019, Physical Review E, 100, 033209

Lipkin, Y. M., Ofek, E. O., Gal-Yam, A., et al. 2004, Astrophysical Journal, 606, 381

Lloyd-Ronning, N. M., & Zhang, B. 2004, Astrophysical Journal, 613, 477

Matsumoto, Y., Amano, T., Kato, T. N., et al. 2015, Science, 347, 974

Matsumoto, Y., Amano, T., Kato, T. N., & Hoshino, M. 2017, Physical Review Letters, 119, 105101

McKenzie, J. F., & Westphal, K. O. 1968, Physics of Fluids, 11, 2350

Medvedev, M., & Loeb, A. 1999, Astrophysical Journal, 526, 697

Medvedev, M. V. 2000, Astrophysical Journal, 540, 704

Medvedev, M. V., Frederiksen, J. T., Haugbølle, T., et al. 2011, Astrophysical Journal, 737, 55

Meegan, C. A., Fishman, G. J., Wilson, R. B., et al. 1992, Nature, 355, 143

Meszaros, P., & Rees, M. J. 1992, Monthly Notices of the RAS, 257, 29P

Mészáros, P., & Rees, M. J. 1997, Astrophysical Journal, 476, 232

Metzger, M. R., Djorgovski, S. G., Kulkarni, S. R., et al. 1997, Nature, 387, 878

Mirzoyan, R. 2019, The Astronomer's Telegram 12390, 1

Mooley, K. P., Deller, A. T., Gottlieb, O., et al. 2018, Nature, 561, 355

Mizuno, Y., Pohl, M., Niemiec, J., et al. 2011, Astrophysical Journal, 726, 62

Molinari, E., Vergani, S. D., Malesani, D., et al. 2007, Astronomy and Astrophysics, 469, L13

Nakar, E., Piran, T., & Granot, J. 2003, New Astronomy, 8, 495

Nava, L., Vianello, G., Omodei, N., et al. 2014, Monthly Notices of the RAS, 443, 3578

Nemiroff, R. J. 1995, Publications of the ASP, 107, 1131

Norris, J. P., Nemiroff, R. J., Bonnell, J. T., et al. 1996, Astrophysical Journal, 459, 393

Nousek, J. A., Kouveliotou, C., Grupe, D., et al. 2006, Astrophysical Journal, 642, 389

Nysewander, M., Fruchter, A. S., & Pe'er, A. 2009, Astrophysical Journal, 701, 824

O'Brien, P. T., Willingale, R., Osborne, J., et al. 2006, Astrophysical Journal, 647, 1213

Ohira, Y. 2013, Astropysical Journal, Letters, 767, L16

Ohira, Y. 2013, Physical Review Letters, 111, 245002

Ohira, Y. 2014, Monthly Notices of the RAS, 440, 514

Ohira, Y. 2016, Astrophysical Journal, 817, 137

pCANS, http:www.astro.phys.s.chiba−u.ac.jp/pcans/

Paczynski, B. 1986, Astropysical Journal, Letters, 308, L43

Paczynski, B., & Rhoads, J. E. 1993, Astropysical Journal, Letters, 418, L5

Paczynski, B. 1995, Publications of the ASP, 107, 1167

Panaitescu, A., & Kumar, P. 2001, Astropysical Journal, Letters, 560, 49

Panaitescu, A., Mészáros, P., Burrows, D., et al. 2006, Monthly Notices of the RAS, 369, 2059

Pelletier, G., Gremillet, L., Vanthieghem, A., et al. 2019, Physical Review E, 100, 013205

Piran, T. 2000, Physics Reports, 333, 529

Piran, T. 2004, Reviews of Modern Physics, 76, 1143

Preece, R. D., Briggs, M. S., Mallozzi, R. S., et al. 2000, Astrophysical Journal, Supplement, 126, 19

Racusin, J. L., Karpov, S. V., Sokolowski, M., et al. 2008, Nature, 455, 183

Ramirez-Ruiz, E., García-Segura, G., Salmonson, J. D., et al. 2005, Astrophysical Journal, 631, 435

Rees, M. J., & Meszaros, P. 1992, Monthly Notices of the RAS, 258, 41

Rhoads, J. E. 1999, Astrophysical Journal, 525, 737

Rossi, E., & Rees, M. J. 2003, Monthly Notices of the RAS, 339, 881

Ross, J. S., Higginson, D. P., Ryutov, D., et al. 2017, Physical Review Letters, 118, 185003

Ruyer, C., Gremillet, L., Bonnaud, G., et al. 2017, Physics of Plasmas, 24, 041409

Ruyer, C., & Fiuza, F. 2018, Physical Review Letters, 120, 245002

Rybicki, G. B., & Lightman, A. P. 1979, A Wiley-Interscience Publication

Sahu, K. C., Livio, M., Petro, L., et al. 1997, Nature, 387, 476

Sakamoto, T., Lamb, D. Q., Kawai, N., et al. 2005, Astrophysical Journal, 629, 311

Sakamoto, T., Hullinger, D., Sato, G., et al. 2008, Astrophysical Journal, 679, 570

Santana, R., Barniol Duran, R., & Kumar, P. 2014, Astrophysical Journal, 785, 29

Sari, R., & Piran, T. 1997, Monthly Notices of the RAS, 287, 110

Sari, R., Piran, T., & Narayan, R. 1998, Astropysical Journal, Letters, 497, L17

Sari, R., & Piran, T. 1999, Astronomy and Astrophysics, Supplement, 138, 537

Sari, R., Piran, T., & Halpern, J. P. 1999, Astropysical Journal, Letters, 519, L17

Schaefer, B. E., Gerardy, C. L., Höflich, P., et al. 2003, Astrophysical Journal, 588, 387

Shu, C.-W., & Osher, S. 1989, Journal of Computational Physics, 83, 32

Silva, L. O., Fonseca, R. A., Tonge, J. W., et al. 2003, Astropysical Journal, Letters, 596, L121

Sironi, L., & Goodman, J. 2007, Astrophysical Journal, 671, 1858

Sironi, L., Spitkovsky, A., & Arons, J. 2013, Astrophysical Journal, 771, 54

Smith, N., Silverman, J. M., Chornock, R., et al. 2009, Astrophysical Journal, 695, 1334

Spitkovsky, A. 2008, Astropysical Journal, Letters, 673, L39

Spitkovsky, A. 2008, Astropysical Journal, Letters, 682, L5

Stanek, K. Z., Matheson, T., Garnavich, P. M., et al. 2003, Astropysical Journal, Letters, 591, L17

Stein, R. F., McCray, R., & Schwarz, J. 1972, Astropysical Journal, Letters, 177, L125

Stockem Novo, A., Bret, A., Fonseca, R. A., et al. 2015, Astropysical Journal, Letters, 803, L29

Tak, D., Omodei, N., Uhm, Z. L., et al. 2019, Astrophysical Journal, 883, 134

Takabe, H., Kato, N. T., Kuramitsu, Y. & Sakawa, Y., 2008, Proceedings of the Conference in Honor of C N Yang's 85th Birthday, Statistical physics, high energy, condensed matter and mathematical physics, Singapore, World Scientific Co., Ltd., pp.538

Takamoto, M., Matsumoto, Y., & Kato, T. N. 2018, Astropysical Journal, Letters, 860, L1

Taylor, G. B., Frail, D. A., Berger, E., et al. 2004, Astropysical Journal, Letters, 609, L1

Tomita, S., & Ohira, Y. 2016, Astrophysical Journal, 825, 103

Tomita, S., Ohira, Y., Yamazaki, R. 2019, Astrophysical Journal, 886, 54

Uhm, Z. L., & Beloborodov, A. M. 2007, Astropysical Journal, Letters, 665, L93

Uhm, Z. L., Zhang, B., Hascoët, R., et al. 2012, Astrophysical Journal, 761, 147

Uhm, Z. L., & Zhang, B. 2014, Astrophysical Journal, 789, 39

van Paradijs, J., Groot, P. J., Galama, T., et al. 1997, Nature, 386, 686

Vanthieghem, A., Lemoine, M., & Gremillet, L. 2018, Physics of Plasmas, 25, 072115

Wang, X., & Lobe, A. 2000, Astrophysical Journal, 535, 788

Wang, Y., Li, L., Moradi, R., et al. 2019, arXiv e-prints, arXiv:1901.07505

Waxman, E. 1997, Astropysical Journal, Letters, 485, L5

Weibel, E. S. 1959, Physical Review Letters, 2, 83

Wijers, R. A. M. J., Rees, M. J., & Meszaros, P. 1997, Monthly Notices of the RAS, 288, L51

Wijers, RAMJ., & Galama, J., T. 1999, Astrophysical Journal, 523, 177

Yalinewich, A., & Portegies Zwart, S. 2019, Astropysical Journal, Letters, 872, L3

Yamazaki, R., Ioka, K., & Nakamura, T. 2004, Astrophysical Journal, 607, 103

Yoon, P. H., & Lui, A. T. Y. 2007, Physics of Plasmas, 14, 104504

Zhao, X., Li, Z., Liu, X., et al. 2014, Astrophysical Journal, 780, 12

Zhang, B., Fan, Y. Z., Dyks, J., et al. 2006, Astrophysical Journal, 642, 354

Zhang, Q., Hunter, T. R., Sridharan, T. K., et al. 2002, Astrophysical Journal, 566, 982

Zhang, B.-B., Zhang, B., Liang, E.-W., et al. 2011, Astrophysical Journal, 730, 141

Zhang, H., Christie, I., Petropoulou, M., et al. 2019, arXiv e-prints, arXiv:1910.14049